EFFICIENT RAY TRACING ALGORITHMS BASED ON WAVEFRONT CONSTRUCTION AND MODEL BASED INTERPOLATION METHOD

A Dissertation

by

KYOUNG JIN LEE

Submitted to the Office of Graduate Studies of
Texas A&M University
in partial fulfillment of the requirements for the degree of

DOCTOR OF PHILOSOPHY

May 2005

Major Subject: Geophysics

EFFICIENT RAY TRACING ALGORITHMS BASED ON WAVEFRONT CONSTRUCTION AND MODEL BASED INTERPOLATION METHOD

A Dissertation

by

KYOUNG JIN LEE

Submitted to Texas A&M University
in partial fulfillment of the requirements
for the degree of

DOCTOR OF PHILOSOPHY

Approved as to style and content by:

Richard L. Gibson, Jr. (Chair of Committee)	Philip D. Rabinowitz (Member)
Mark E. Everett (Member)	David W. Sparks (Member)
Donald Allen (Member)	Richard L. Carlson (Head of Department)

May 2005

Major Subject: Geophysics

ABSTRACT

Efficient Ray Tracing Algorithms Based on
Wavefront Construction and
Model Based Interpolation Method. (May 2005)
Kyoung Jin Lee, B.S., Korea University, Korea;
M.S., Texas A&M University
Chair of Advisory Committee: Dr. Richard L. Gibson

Understanding and modeling seismic wave propagation is important in regional and exploration seismology. Ray tracing is a powerful and popular method for this purpose. Wavefront construction (WFC) method handles wavefronts instead of individual rays, thereby controlling proper ray density on the wavefront. By adaptively controlling rays over a wavefront, it efficiently models wave propagation. Algorithms for a quasi-P wave wavefront construction method and a new coordinate system used to generate wavefront construction mesh are proposed and tested for numerical properties and modeling capabilities. Traveltimes, amplitudes, and other parameters, which can be used for seismic imaging such as migrations and synthetic seismograms, are computed from the wavefront construction method. Modeling with wavefront construction code is applied to anisotropic media as well as isotropic media. Synthetic seismograms are computed using the wavefront construction method as a new way of generating synthetics. To incorporate layered velocity models, the model based interpolation (MBI) ray tracing method, which is designed to take advantage of the wavefront construction method as well as conventional ray tracing methods, is proposed and experimental codes are developed for it. Many wavefront construction codes are limited to smoothed velocity models for handling complicated problems in layered velocity models and the conventional ray tracing methods suffer from the inability to control ray density during wave propagation. By interpolating the wavefront near model boundaries, it is possible to handle the layered velocity model as well as overcome ray density control problems in conventional methods. The test results revealed this new method can be an effective modeling tool for accurate and effective computing.

To my Lord Jesus, my lovely wife Jiyoung, and my son Jeffrey

ACKNOWLEDGMENTS

I would like to thank my family for supporting my study. My son, Jeffrey, helped me by doing his part at home and my wife, JiYoung, was always my supporter. I also extend my thanks to my church members for sharing and encouraging me whenever I had trouble.

I also want to thank my friends in Dr. Gibson's seismic lab. Sung Yuh and Costas Tzimeas, former students of the lab, shared lots of valuable things by discussing problems in the research as well as in life. John, Hungliang, Pablo, Seung, and Ravi were nice friends to have good conversations with on many topics.

I deeply appreciate the advice and the direction by Dr. Gibson. Whenever I had problems with my research or my personal life, he was the best person I could go to for help. He helped me, not only as an academic advisor, but also as a counselor. I also appreciate my committee members, Dr. Rabinobitz, Dr. Everrette, Dr. Sparks, and Dr. Allen. Their classes and their direction were always good for understanding my research problems and for helping me set the right attitude for the work. I also extend my appreciation to Dr. Gangi, my former MS advisor. He always showed energy and enthusiasm for the research. He also helped me as a mentor.

TABLE OF CONTENTS

CHAPTER Page

LIST OF TABLES

TABLE Page

LIST OF FIGURES

FIGURE Page

FIGURE Page

CHAPTER I

INTRODUCTION

1.1 Overview

Modeling of seismic wave propagation in the subsurface is a very important part of interpreting physical properties from seismic data. Several methods are available for such modeling, including the finite-difference methods and ray tracing methods. The finite-difference method (FDM) attempts to solve an exact elastic or an acoustic wave equation by discretizing the model and applying finite-differences technique to solve partial differential equation. This method can obtain the complete solution (total wavefield) (Virieux, 1986; Levander, 1988). However, the simulated wavefield by finite-difference can be very complicated and difficult to interpret. Also, the finite-difference method is comparatively slow and requires significant memory resources, especially for 3D simulation.

In contrast to the finite-difference method, ray tracing solves simpler equations resulting from a high-frequency approximation. Červený (1972) has derived kinematic description of elastic waves and amplitude solutions for heterogeneous, anisotropic media. Using the ray tracing method, we can calculate the traveltimes and the amplitudes for different wave types independently. In other words, we can select our desired wave type and simulate the wave propagation of that wave type only (Červený, 2001). The ray tracing method is therefore very fast compared to the finite-difference method, and it is widely used in earthquake seismology as well as seismic imaging. Although ray tracing is relatively fast and less expensive than finite differences, conventional ray tracing has some limits in practical applications. One of the well known difficulties is the two-point problem, which involves finding an exact ray path between source and receiver points. Also, when individual rays are traced as in the traditional ray tracing method, the constant initial number of rays may be not enough to cover the areas where the rays are diverging rapidly.

This dissertation follows the style and format of Geophysics.

When we need to compute only the traveltime of propagating waves, solving eikonal equation with the finite-difference method and the graph ray tracing method can be other choices (Vidale, 1988; Vidale, 1990; Moser, 1991). The finite-difference eikonal solver (FDES) computes the first-arrival traveltimes on a predefined grid space and it is known that this method is fast and robust (Kim and Cook, 1999). But this method is limited by computing the minimum traveltimes or first-arrival times due to the mathematical properties in the finite-difference solutions of the eikonal equation (Van Trier and Symes, 1991). This becomes a critical drawback when later-arrivals are important in subsurface imaging (Geoltrain and Brac, 1993). To compute amplitudes from FDES solver as additional features, Qian and Symes (2002) proposed a FDES algorithm in anisotropic media considering amplitudes as well as traveltimes. The needs for the handling of later arrivals led to the recent developments in the eikonal solver which can compute reliable traveltimes and amplitudes of later arrivals (Qian and Symes, 2002; Buske and Kästner, 2004).

The network ray tracing or shortest ray path method has been developed to overcome the restrictions of conventional ray tracing such as diffracted ray paths and the paths to shadow zones by taking the shortest or fastest path over a network of subdivided velocity blocks (Moser, 1991). This is also called a graph method because the approach of locating the shortest path is found in graph theory. Ray paths of shortest traveltime are found by connecting the grid points or nodes and the grid points act as scatters or secondary sources of the propagating wave, stated as Huygens' principle. It is known that this method is very stable for finding the global minimum traveltime (Cheng and House, 1996). The major drawback of this method is the computation time of searching the minimum traveltime over the network of cells or velocity blocks (van Avendonk et al., 2001).

The Wavefront construction method is an extension of the conventional ray tracing technique. This method was developed in the early 90's (Vinje et al., 1993; Vinje et al., 1999; Lambaré et al., 1996; Lucio et al., 1996; Ettrich and Gajewski, 1996; Gibson, 1999; Gjøstdal et al., 2002) to improve the computational efficiency and to overcome conventional ray tracing system's inherited problems such as the two-point problem and possible artificial shadow problems. Because wavefront construction based ray tracing considers an entire wavefront instead of tracing individual rays and adaptively controls the ray density on the wavefront, it is better able to model this type of propagation. As a result, by using wavefront based ray tracing, it is possible to avoid artificial “shadows” typical of conventional ray methods. Earlier WFC algorithms are designed for isotropic media (Vinje et al., 1999; Lambaré et al., 1996; Lucio et al., 1996) and recently several authors have introduced anisotropic WFC algorithms (Gibson, 1999; Lee and Gibson, 2003; Mispel and Williamson, 2001; Kaschwich and Gajewski, 2003). Very similar with wavefront construction method, the wavefront oriented ray tracing inserts new rays from the source point when the ray density is less than the preset threshold at a wavefront (Coman and Gajewski, 2001; Kaschwich and Gajewski, 2003). The merit of wavefront oriented ray tracing is the higher accuracy than the wavefront construction method due to reducing the possible errors of ray insertion. Both methods are basically same idea and if the wavefronts are constructed with enough number of rays, the difference between the two methods should be small enough. Details of the theoretical backgrounds and developments of ray tracing are described in appendix A and the derivation of amplitude computation in ray tracing with Jacobian is shown in appendix B.

Leidenfrost et al. (1999) performed a comparison of the accuracy, computation time, and usage of system resources for various versions of the finite-difference eikonal solvers (FDES), graph method, and wavefront construction method (WFC). They performed this test on a 2D gradient and a 2D Marmousi model but the results would be similar in a 3D case. The accuracy test showed that FDES methods have higher errors than graph or WFC methods. In terms of computation time, the graph method took more than twice the computation time than other methods. In memory resource usage tests, all methods took similar resources except WFC, which took more for the 2D Marmousi model.

They have concluded that the FDES (FD method in Cartesian coordinate) and WFC methods are good. In general the FD method is good because it is fast and sufficiently accurate, but it is limited to use for simpler gradient models due to the lack of tracking multiple arrival traveltimes. WFC is their method of choice even though its memory requirements are higher than other methods because of its ability to model complicated smooth media, speed and robustness, and handling of later-arrival traveltimes.

In conventional ray tracing methods, ray parameters are defined as $\gamma_1 = \psi$ (declination), $\gamma_2 = \theta$ (azimuth), and $\gamma 3 = \tau$ (traveltime) to set up the initial rays. In most WFC based ray tracing, the initial rays are traced with the initial mesh geometry, which uses the conventional ray parameters. In the conventional take-off angle parameters, due to regularly discretized angle domain, the initial mesh constructing the initial wavefront has very dense rays and will also have singular points at or near the poles (Lee and Gibson, 2003). The resulting WFC ray tracing has 1) inefficiency from calculating very dense rays near the poles and 2) the vertical rays through the source to the poles will have numerically unstable ray derivatives $(\frac{\partial x_i}{\partial \gamma_j}, \frac{\partial p_i}{\partial \gamma_j})$ which are essential numerical components in kinematic ray tracing. If we can generate more evenly distributed rays on wavefronts without geometric poles, it will help to avoid the above problems. In this dissertation, I am proposing another possible mesh generation scheme, cubed sphere mesh which is a centered focal cube idea. The detailed ideas, implementations, and numerical properties are described in chapter 2. Modeling of isotropic and anisotropic media and the application of wavefront construction method to generate synthetic seismograms is also described in chapter 3 to demonstrate the ability of the modeling capability.

The Wavefront construction method, proposed and developed in this dissertation, is a strong and useful tool for seismic modeling. However, the current stage of development requires smoothed or gradient velocity models as in other wavefront construction codes. This is due to high-frequency approximations and the complicated handling or book keeping problem of neighboring rays on wavefronts with hard boundaries between layers. However, when we use conventional ray tracing, such as the layer stripping method, there is no way to control the ray density over wave propagation. The proposed model based interpolation (MBI) ray tracing method takes advantages of the wavefront construction method as well as the layered model handling capability of conventional ray tracing systems.

In MBI ray tracing, instead of interpolating a wavefront mesh at regular increments of traveltime, the interpolation step is applied only at interfaces inside the earth model. This simplification facilitates the implementation, given the potentially complex wavefront changes that may take place as a wavefront propagates away from an interface. The application of the interpolation can even be limited to a subset of one or more of the boundaries to improve computation time as well.

This new method has been implemented, and its results are demonstrated in this dissertation to illustrate its potential for facilitating more effective ray modeling of layered media.

1.2 Objectives

The objectives of this thesis are to first develop quasi P-wave WFC algorithms for general anisotropic medium and setting standard test models, and then develop the model based interpolation (MBI) ray tracing method for layered models. Analyses of numerical properties of the WFC method for different mesh generation schemes and finite-difference methods is a part of the algorithm development. As an application of the WFC method, generation of synthetic seismograms from amplitude, traveltime, and the Green's tensor and comparing them to the field data are important steps. Development of the MBI ray tracing method and performing some feasibility tests to verify the possibility of implementing the method and the error analysis of its traveltime estimation are other goals in this research.

1.2.1 Algorithm Development

In this dissertation, the primary interest is quasi P-wave propagation and chapter 2 presents a summary of the algorithm and a new mesh design scheme for more effective quasi P-wave WFC modeling. P-wave seismic data are most frequently acquired in exploration seismic surveys. In marine seismic surveys with hydrophone receiver arrays, only pressure (acoustic wave) can be recorded by this type of sensor and shear waves can not propagate in the water except for converted waves generated at internal subsurface boundaries.

The first goal is the development of quasi p-wave wavefront construction codes with conventional take-off angle ray coordinates. Computation of traveltimes and amplitudes are also important procedures in this step. Developing wavefront construction code with the proposed cubed sphere mesh coordinate will be the next step. Setting up of basic mathematical derivations and implementations of the algorithm in the code are required. To analyze the numerical behavior of both experiments, it is necessary to design a mapping function to map propagating wavefronts in 3D to a 2D surface, usually a free surface at zero depth. Then, analyses of the results of traveltime and amplitude are required on a surface as well as on a wavefront to understand the physical behavior of different coordinate based ray tracing.

To interpolate a wavefront cell, we are using paraxial computation which requires ray derivatives. The derivatives can be calculated by the finite-difference method. We can use simple single side (forward) finite-difference computation for easy implementation of wavefront code development. Another way is using central finite-difference computation, which requires rigorous neighbor checks at a wavefront patch for the eligibility of central finite-difference scheme. How the numerical properties change and the trade-offs of two methods are discussed. Also, for practical purpose, it is good to have more automated control of the starting number of rays. A recursive algorithm has been applied to determine the optimum number of rays on the initial wavefront and the threshold or criteria of optimum initial numbers are investigated.

1.2.2 WFC Modelings and Synthetic Data Application

The WFC algorithm has been applied to some basic models and a gradient velocity model acquired from field data by minimizing traveltimes between observed traveltime data and forward modeling outputs by WFC (Durussel, 2002; Gibson et al., 2005) in chapter 3. Synthetic seismograms can be computed and used in forward modeling. From the equation of medium response (displacement) we can compute and compare the waveforms of synthetics with field recordings. This can be used for the validation check of the forward modeling such as preliminary velocity modeling before going into more specific velocity analysis like migration velocity model building.

Synthetic seismograms are also important because they show how we understand the physics of the modeling media and the source mechanism. If we understand the medium, such as anisotropy and velocity distribution, and source mechanism, the synthetics and the field data will be similar. As such, this can be a useful tool for earthquake seismology. In earthquake seismology, due to sparse receiver distribution, long periods or wavelengths of seismic waves, and long and complicated propagation paths, individual waveform details contain important information to interpret. Thus, the synthetic seismograms we are generating to compare to the field record reveals our understanding of the process. Also, compared to other modeling methods, our wavefront based synthetic seismograms have advantages of computing time and resources. WFC applications of synthetic seismograms are also described in chapter 3.

1.2.3 Model Based Interpolation (MBI) Ray Tracing

Utilizing wavefront construction code, taking layered velocity models constraining the interpolation in a wavefront mesh elements near the layer boundaries, the development of algorithms for the MBI ray tracing method is another major task. By constructing a wavefront in a wavefront element (or a ray tube) before it arrives at a certain layer boundary we can apply the basic ideas of wavefront construction code handling interpolations test, perform insertion of new rays and manipulate book keeping problems for the necessary ray derivatives computations. Associating layer boundary space and wavefront space is a important step for this approach.

To show the possibility of implementing MBI ray tracing, simple isotropic/ anisotropic layered models and a salt dome model with isotropic/anisotropic layers are tested in chapter 4. The difference between conventional ray tracing with initially dense rays and MBI ray tracing results are measured and used as a tools to see how the proposed MBI method works.

CHAPTER II

NUMERICAL PROPERTIES OF MESH GENERATION SCHEMES IN WAVEFRONT CONSTRUCTION METHOD

Ray tracing methods are high frequency approximations and based on optical ray theory and were developed for seismic wave modeling in the 1970s and 1980s (Fedorov, 1968; Červený, 1972; McMechan and Mooney, 1980; Hanyga, 1982; Červený, 1985; Gajewski and Pšenčik, 1987; Beydoun and Keho, 1987; Chapman and Shearer, 1989). The conventional ray methods have suffered from two-point problem which finds the exact ray path between the source and the receiver positions, and artificial shadows which are caused by diverged rays with fixed initial ray parameters. This should be distinguished from actual shadow zones where seismic waves can't reach. To overcome the two-point problem, paraxial ray tracing technique has been developed (Beydoun and Keho, 1987; Gibson et al., 1991).

Other methods based on ray theory are finite-difference Eikonal solvers and wavefront construction methods. The finite-difference Eikonal solvers are known to be fast and robust (Vidale, 1990; Van Trier and Symes, 1991; Kim, 2002). Early developments of the Eikonal solvers were limited to first arrivals and traveltimes only (Geoltrain and Brac, 1993). Recent developments in the Eikonal solvers can compute traveltimes and amplitudes of later arrivals (Qian and Symes, 2002; Buske and Kästner, 2004).

Wavefront construction methods have been developed in early 90s to overcome the known problems in conventional ray tracing systems (Vinje et al., 1993; Lambaré et al., 1996; Lucio et al., 1996; Ettrich and Gajewski, 1996; Gibson, 1999; Vinje et al., 1999; Gibson et al., 2002; Mispel and Williamson, 2001; Lee and Gibson, 2003; Gibson et al., 2005). In the wavefront construction method, volumetric wavefronts are propagated instead of handling individual rays and wavefront construction methods explicitly track the propagation of wavefronts through an earth model to perform calculations that are more efficient and more accurate than conventional ray algorithms.

Both wavefront construction and traditional ray tracing algorithms suffer from serious limitations when take-off angles are used as ray parameters. The ray parameters uniquely define a ray in space and time, and both methods use ray parameters as the building blocks of the modeling systems. In constructing wavefronts, conventional ray parameters of take-off angles result in numerical instability of ray derivatives and unnecessarily dense rays at or near the pole, where declination is $\approx \pm 90°$. If we can design different ray parameters which generate evenly distributed rays over a wavefront, the numerical instability and inefficiency near the pole in conventional ray parameters can be avoided. The cubed sphere mesh scheme has been proposed in this paper as an alternative way of generating initial meshes and it can be used as a replacement for conventional ray parameters. In the cubed sphere mesh coordinate ray parameters, an imaginary cube centered at the source is discretized and rays are traced from the source through the discretized points for a certain traveltime. Declination and azimuth angles in the conventional ray parameters are replaced by the Cartesian coordinates of the discretized points on the face of the cube and the traveltime is kept as the third parameter. The resulting wavefront constructed with the cubed sphere mesh does not have geometric poles which causes the numerical instability and inefficiency. The analyses of the numerical behavior of the cubed sphere mesh coordinate and take-off angle mesh coordinates showed that the proposed method is acceptable for computing traveltime and amplitude with stabler numerical properties than conventional take-off angle ray parameters.

2.1 Ray Tracing in Anisotropic Media

Ray tracing methods or asymptotic wave methods result from a high frequency approximation to the 3D wave equation (Červený, 2001). Physically, this can be interpreted as applying the assumption that the characteristic length of the propagating medium is larger than the wavelength of the propagating wave (Gibson et al., 1991; Ben-Menahem and Beydoun, 1985; Ben-Menahem et al., 1991). The ray paths and traveltimes for general anisotropic media can be computed by integrating the right hand side of a set of ordinary differential equations (O.D.E.) in the form

$$\begin{aligned} &\tfrac{dx_i}{d\tau} = a_{ijkl} p_l g_j g_k \\ &\tfrac{dp_i}{d\tau} = -\tfrac{1}{2} \tfrac{da_{ijkl}}{dx_i} p_n p_l g_j g_k \\ &a_{ijkl} = \tfrac{c_{ijkl}}{\rho}. \end{aligned} \tag{2.1}$$

Here, x_i are spatial coordinate components, p_i are slowness vector components, τ is traveltime, a_{ijkl} are density normalized elastic moduli (stiffness tensor), and g_i are eigenvectors of Christoffel matrix, Γ_{ij},

$$\begin{aligned} &(\Gamma_{jk} - v^2\delta_{jk})u_k = 0, \\ &\Gamma_{jk} = a_{ijkl}p_i p_l \end{aligned} \tag{2.2}$$

where v is a phase velocity in the direction of p_i and we have three eigenvalues for each squared phase velocity. The traveltime along a ray path can be found by solving the right hand side of $dx_i/d\tau$, the first equation in equation (2.1).
The amplitude for a point source in an isotropic medium (Gajewski and Pšenčik, 1987; Červený, 2001) is

$$A(\tau) = \left[\frac{\rho(\tau_0)v(\tau_0)J(\tau_0)}{\rho(\tau)v(\tau)J(\tau)}\right]^{1/2} A(\tau_0) \tag{2.3}$$

where τ is traveltime, τ_0 is the time at the source, the functions of τ ($\rho(\tau)$, $v(\tau)$, and $J(\tau)$) are evaluated at some traveltime τ along the ray path, ρ is the density function of the medium, and J is the Jacobian representing the transformation from ray coordinates to Cartesian coordinates.

$$J(\tau) = \left|\frac{\partial x_i}{\partial \gamma_j}\right| \tag{2.4}$$

If we consider only an isotropic and homogeneous medium, (2.3) takes the simpler form of

$$\begin{aligned} A(\tau) &= \left[\frac{J(\tau_0)}{J(\tau)}\right]^{1/2} A(\tau_0) \\ &\propto \frac{1}{R} \end{aligned} \tag{2.5}$$

where R is a distance from the source to the receiver point at traveltime (τ) along the ray path.

In the conventional ray tracing system, traveltime is computed by solving kinematic ray tracing system [KRT: Equation (2.1)], and the amplitude can be computed by solving Dynamic Ray Tracing (DRT) which requires solving another set of ordinary differential equations (Červený, 1985; Ettrich and Gajewski, 1996; Červený, 2001). However, by estimating ray derivatives directly on a wavefront with the finite-difference way, it is possible to avoid solving the DRT which is computationally expensive. In this paper, I have focused on the analysis of Jacobians with the finite-difference method to compute the amplitude without solving the DRT equations.

2.2 Wavefront Construction Method (WFC)

Wavefront Construction Method (WFC) is one implementation of the ray tracing method. The basic difference between the WFC method and conventional ray tracing is how individual rays are implemented (Gibson et al., 2005). Instead of tracing a specified set of rays from a source to the boundary of a model, the WFC method begins with a few rays at the source and then adaptively adds new rays as the wavefront propagates away from the source (Figure 2.1) (Vinje et al., 1993; Lambaré et al., 1996; Ettrich and Gajewski, 1996; Vinje et al., 1999; Gibson, 1999; Gibson et al., 2002; Gjøstdal et al., 2002).

The WFC algorithm has been implemented in three steps: 1) individual ray tracing computation, 2) initial wavefront mesh construction, and 3) propagation of wavefront mesh and interpolation when necessary (Gibson et al., 2005).

2.2.1 Ray Tracing

Asymptotic seismic ray tracing can be obtained by solving a set of ordinary differential equations (2.1). In this paper, we have used the 5th order Runge-Kutta method to numerically solve the ordinary differential equations; other numerical solvers such as Hamming's predictor-corrector method or Adams-Moulton predictor formula can be used. Ray tracing is not limiting any particular numerical solver as long as we can compute physically valid rays. Also, ray tracing can be performed with different approaches such as the graphical ray method or the simple geometric ray tracing for multi-layered model with isotropic homogeneous layers.

2.2.2 Initial Mesh Construction

The initial mesh in the wavefront construction method describes the geometric distribution of initial rays. The initial mesh can be regarded as a set of initial conditions for each of the ray directions. The initial conditions or the take-off directions of each

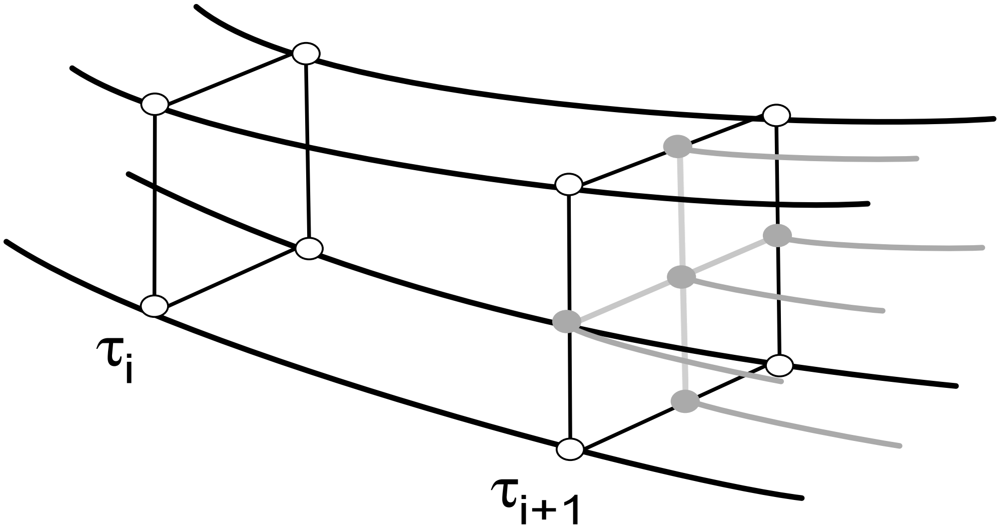

Fig. 2.1. Rays are diverging with wave propagation and new rays are inserted at the interpolated points on the wavefront to satisfy accuracy criteria and constant density of rays.

ray are specified with two ray parameters, γ_1 and γ_2, and we can set the third ray parameter as the traveltime, $\gamma_3 = \tau$, or arclength, $\gamma_3 = s$, along the ray path (Červený, 2001). The initial mesh is then constructed by connecting the points sharing the same traveltime along the ray paths ($\gamma_1 = \psi$, $\gamma_2 = \phi$, and $\gamma_3 = \tau_0$) (Figure 2.2). Constructing the initial mesh with take-off angles is very natural and easy to visualize and implement. However, this mesh coordinate system always has geometric poles at the top and the bottom (declination angle, $\psi = \pm 90°$), where the population of rays is very dense and it is computationally inefficient. Further more, when we compute ray derivatives near or at the pole, it is numerically unstable. A detailed discussion regarding these numerical properties will be presented in a later section.

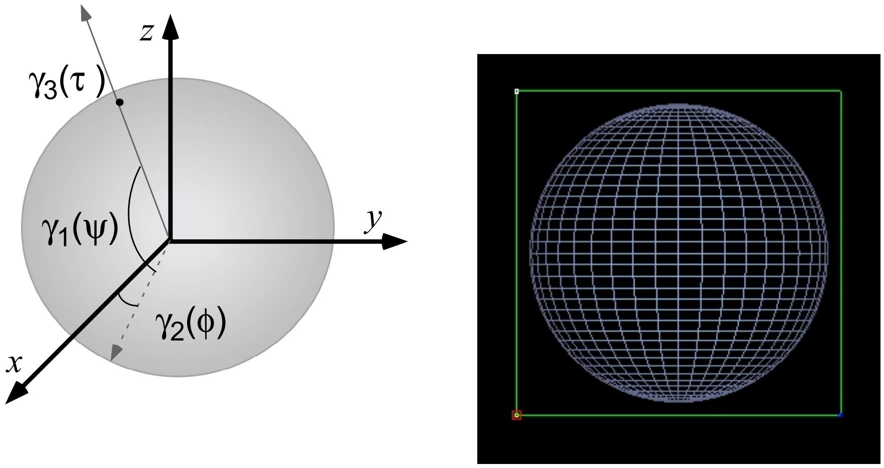

Fig. 2.2. Left: In take-off angle mesh coordinate, the ray parameters are defined as $\gamma_1 = \psi$(declination), $\gamma_2 = \phi$(azimuth), and $\gamma_3 = \tau$(traveltime). Right: Constructed wavefront with take-off angle meshes. Note that there are two geometric poles at the top and the bottom and very high ray density near the poles.

Recalling that we can use any physical quantity for the ray parameters as long as we can specify the ray uniquely, we can design different types of mesh generation schemes by choosing another set of ray parameters. An alternative choice of ray parameters is the cubed sphere mesh (Figure 2.3), which uses a imaginary cube (focal cube) centered at the source point. Initial rays are projected from the source point for a unit traveltime, passing through the discretized points on each face of the cube. The cube is constructed with a unit length and discretized by $N \times N$ points for each face. Therefore, we have total $6 \times N^2$ points over all cube faces. The number of discretized points and the shape of the cube can be changed from $N \times N$ to $N \times M$, where N and M are the number of discretized points and cubic shape to rectangular prism shape. For the $N \times N$ discretization and the most general equal-length focal cube, all the rays are distributed evenly on all six faces of the focal cube. Thus, the cubded sphere mesh coordinate system does not have the pole problem associated with the take-off angles.

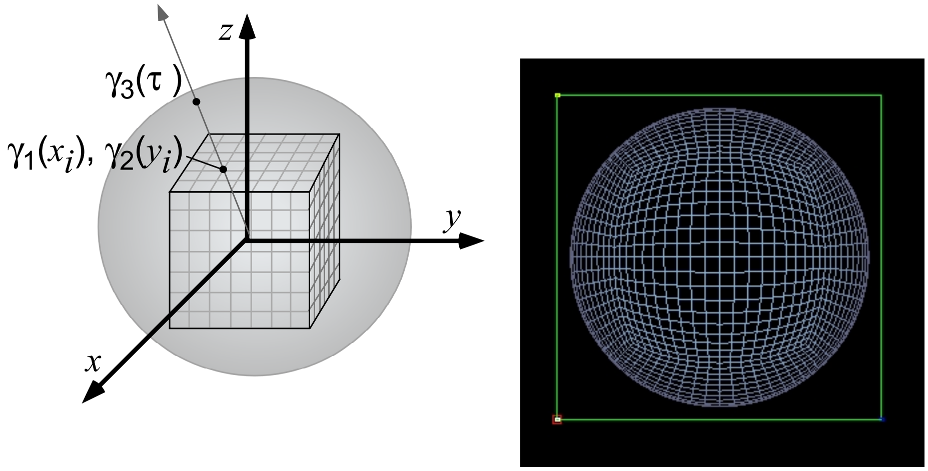

Fig. 2.3. Left: Suppose we have a unit cube centered at the source point, then a ray can be traced from the source point through an evenly discretized point on the face of the focal cube face. The coordinates of discretized points on the face of focal cube are new ray parameters defined as $\gamma_1 = x_i$ (x_1 component of a face), $\gamma_2 = x_j$ (x_2 component of a face), and $\gamma_3 = \tau$ (traveltime). Right: Constructed wavefront with cubed sphere meshes. Note that there are no geometric poles and rays are evenly distributed over the faces of imaginary cube.

To find the relationship between the take-off angles and the ray parameters in cubed sphere mesh coordinate in homogeneous medium, consider a discretized point (x_c, y_c) on a face of the cube, then the azimuth(ϕ) and declination (ψ) angles are

$$\phi = atan(\tfrac{y_c}{x_c}) \tag{2.6}$$

$$\psi = atan\left(\tfrac{1}{\sqrt{x_c^2+y_c^2}}\right). \tag{2.7}$$

The Cartesian coordinate components on the wavefront at a time (τ sec) will be in the direction indicated by the two take-off angles, azimuth (ϕ) and declination (ψ),

$$\begin{aligned} x &= v\tau \cdot cos\psi \cdot cos\phi \\ y &= v\tau \cdot cos\psi \cdot sin\phi \\ z &= v\tau \cdot sin\psi \end{aligned} \tag{2.8}$$

where, v is the velocity in the direction given by ψ and ϕ, and τ is the traveltime (the third ray parameter).

2.2.3 Propagation and Interpolation of the Wavefront

The wavefront in this method is defined as a surface connecting the points of the same traveltime along the each ray path. The wavefront is composed of elementary geometric subdivisions of adjacent rays. The elementary geometric subdivisions are called wavefront mesh cells or wavefront meshes elements. Triangular or quadrilateral shapes are commonly used to define the wavefront mesh cell. In this paper, we use quadrilateral cells to define wavefront meshes while other researchers are using triangular meshes (Vinje et al., 1993; Lambaré et al., 1996; Gibson et al., 2005). The merit of using a quadrilateral mesh is its geometrical shape for implementing finite-difference computation. Due to its symmetric shape in the ray coordinate domain, it is easier to find corresponding finite-difference grid points than triangular meshes. To compute ray derivatives which are used in numerical ray tracing, paraxial computation, and amplitude computation, finite-difference schemes have been implemented [equations (2.12) and (2.13)]. Figure 2.1 shows the wavefront composed of quadrilateral cells is propagating through the model space and new rays are inserted if it is necessary to keep a certain level of ray density. The actual wavefront propagation and interpolation/insertion of new rays are shown in Figure 2.4.

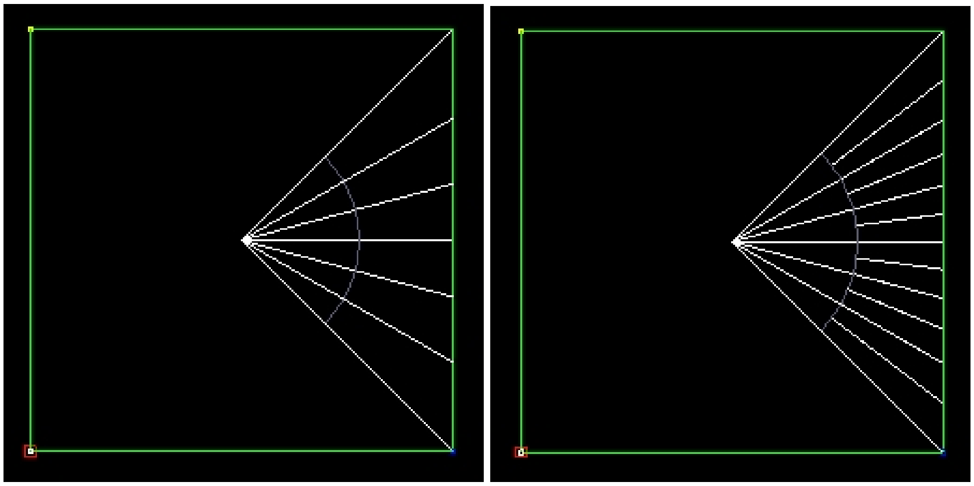

Fig. 2.4. An example showing implemented ray interpolation on the wavefront to satisfy accuracy criteria and constant density of rays. The wavefront of sparse rays (left) has been interpolated after propagation of one more wavefront step (right).

2.2.3.a Interpolation Criteria for Wavefront Mesh Refining

In the WFC method, the initial wavefront propagates through the model space by controlling the ray density on a wavefront to ensure numerical accuracy. To control the insertion of new rays, or interpolation of a wavefront, we can use several quantities as interpolation criteria such as constant distance between adjacent rays, constant area defined by adjacent four rays (a cell on a wavefront), or other quantities. Vinje (1993; 1999) used constant distance as the threshold and Lucio et al. (1996) and Lambaré et al. (1996) used distance and slowness perturbation as the threshold (Figure 2.5).

Another good criteria for interpolation could be traveltime perturbation on a wavefront which is a more physically meaningful measure as a threshold. The traveltime on a certain wavefront at all the ray intersection points with the wavefront have the same traveltime by definition. Then, if we can calculate traveltime perturbation between actual traveltime (which is already known) and a numerically estimated perturbed traveltime, we can use the difference as our threshold. The perturbed traveltime can be calculated using paraxial ray tracing.

The paraxial traveltime correction is a form of the Taylor series expansion ex-

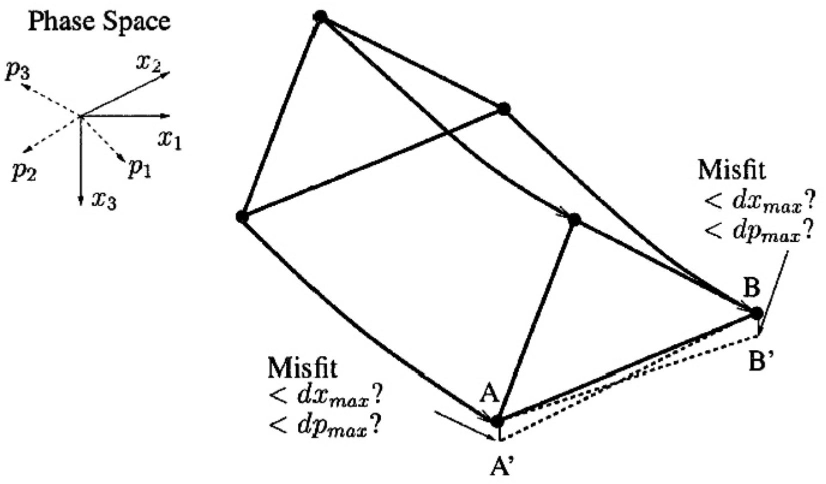

Fig. 2.5. The ray interpolation criterion by Lucio et al. (1996) and Lambaré et al. (1996). Paraxial computation of slowness at point B' is compared with the ray arrival point A' to estimate paraxial perturbation of Δp. Also, position error Δx for the above points are used to decide the interpolation. (after Lucio et al. (1996)).

pressed in ray parameters and slowness vectors (Gibson et al., 1991).

To use it as an interpolation criterion, we set the lower left corner of a quadrilateral cell as our point of reference and the upper right corner of a cell as our point of interest (Figure 2.6). Then, using the ray derivatives expressed in the slowness vector, the approximate traveltime, τ' can be estimated at the point of interest (Gibson et al., 1991).

$$\tau'(x'_j) = \tau_0(x_j) + p_k(x'_j)(x'_k - x_k) + \frac{1}{2}N_{ik}(x_j)(x'_i - x_i)(x'_k - x_k) \tag{2.9}$$

where, the slowness

$$p_k(x'_j) = \left.\frac{\partial \tau}{\partial x_k}\right|_{x'_j} \tag{2.10}$$

$$\begin{aligned} N_{ik}(x_j) &= \tfrac{\partial^2 \tau}{\partial \tau_k \partial x_i} \\ &= \tfrac{\partial p_i}{\partial x_k} \\ &= \tfrac{\partial p_i}{\partial \gamma_j}\tfrac{\partial \gamma_j}{\partial x_k} \\ &= Y_{ij}(X^{-1})_{jk} \end{aligned} \tag{2.11}$$

If the estimated correction time, $d\tau = \tau - \tau'$ in equation (2.9) is greater than the preset threshold level, we interpolate the cell (Figure 2.6).

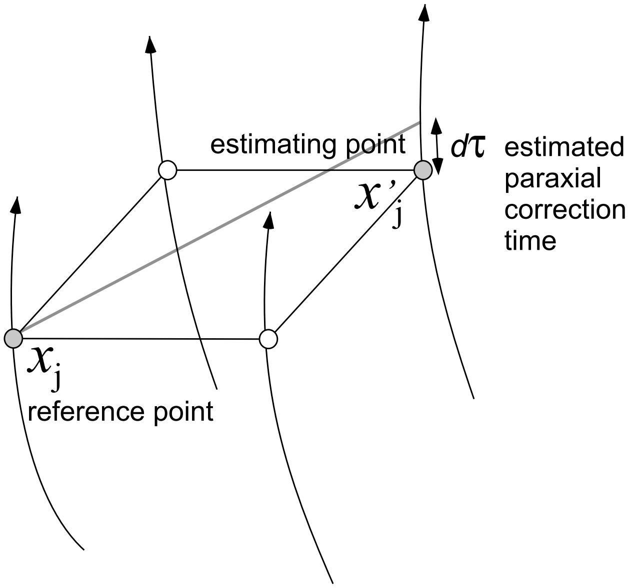

Fig. 2.6. Paraxial computation of $d\tau$ is using two points, (usually diagonal) on a mesh. Because the traveltime at a mesh node on a wavefront is the same for all nodes, the paraxial correction time, $d\tau$, can be a measure of the divergence of rays. Due to the asymmetry of a mesh in general, we are calculating 4 $d\tau$s around all mesh nodes and averaging them to compare them to the interpolation threshold.

2.3 Numerical Properties of Mesh Generation Schemes

The numerical properties of each mesh generation scheme are a function of the properties of ray derivatives. The numerically estimated ray derivatives in the form of $\partial x_i / \partial \gamma_j$ are widely used in the ray tracing system. One can find these derivatives used in the paraxial computation, solving the Christoffel equation and the Jacobians [equations (2.9), (2.2), and (2.4)].

To numerically compute the ray derivatives, we use the finite-difference method. The simplest form of the finite-difference method is simple forward finite-difference which uses just one side of the computing node in the finite-difference grid. Another popular way of computing the finite-difference way of derivatives is the central finite-difference scheme.

The forward difference scheme is

$$f_i' = \frac{f_{i+1} - f_i}{h} - \frac{1}{2} h f''(\xi), \quad \xi \text{ in } [\gamma_k^i, \gamma_k^{i+1}], \tag{2.12}$$

where h is $\gamma_k^{i+1} - \gamma_k^i$ (γ_k is the k^{th} ray parameter and i is the index of a grid point of γ_k). Note that the error is $O(h) = \frac{1}{2} h f''(\xi)$. Suppose we use a second-degree polynomial taht matches γ_k^{i-1}, γ_k^i, and γ_k^{i+1},

the central-difference derivative formula is

$$f_i' = \frac{f_{i+1} - f_{i-1}}{2h} - \frac{1}{6} h^2 f^{(3)}(\xi), \quad \xi \text{ in } [\gamma_k^i, \gamma_k^{i+1}]. \tag{2.13}$$

The simple forward-difference method has truncation errors of the order of one [$O(h)$] and the central-difference formula has the order of two [$O(h^2) = \frac{1}{6} h^2 f^{(3)}(\xi)$]. That means by introducing one more term, we will improve the order of errors.

Jacobian has been used for the measure of numerical properties of wavefront construction method. In conventional ray take-off angle mesh for homogeneous medium, the analytic form of Jacobian is (Červený, 2001)

$$\begin{aligned} J &= \left| \frac{\partial x_i}{\partial \gamma_j} \right| \\ &= l^2 \cdot cos\psi \\ &= v^2 \tau^2 \cdot cos\psi = v^2 \gamma_3^2 \cdot cos\gamma_1 \end{aligned} \tag{2.14}$$

where, l is the distance from the source.

To derive the analytic form of the Jacobian in cubed sphere mesh coordinates, set up the matrix (T) of partial derivatives for the transformation from the cubed sphere mesh coordinates to Cartesian coordinates. From the equations (2.7) and (2.8) about the relation between Cartesian coordinate and declination/azimuth angles, the matrix (T) of partial derivatives is

$$T = \begin{bmatrix} \frac{\partial x}{\partial x_c} & \frac{\partial x}{\partial y_c} & \frac{\partial x}{\partial z_c} \\ \frac{\partial y}{\partial x_c} & \frac{\partial y}{\partial y_c} & \frac{\partial y}{\partial z_c} \\ \frac{\partial z}{\partial x_c} & \frac{\partial z}{\partial y_c} & \frac{\partial z}{\partial z_c} \end{bmatrix} = \begin{bmatrix} \frac{\tau(1+y_c^2)}{(1+x_c^2+y_c^2)^{3/2}} & -\frac{\tau x_c y_c}{(1+x_c^2+y_c^2)^{3/2}} & \frac{x_c}{(1+x_c^2+y_c^2)} \\ -\frac{\tau x_c y_c}{(1+x_c^2+y_c^2)^{3/2}} & \frac{\tau(1+x_c^2)}{(1+x_c^2+y_c^2)^{3/2}} & \frac{y_c}{(1+x_c^2+y_c^2)} \\ -\frac{\tau x_c}{(1+x_c^2+y_c^2)^{3/2}} & -\frac{\tau y_c}{(1+x_c^2+y_c^2)^{3/2}} & \frac{1}{(1+x_c^2+y_c^2)} \end{bmatrix} \tag{2.15}$$

where, (x, y, z) are the components in the Cartesian coordinate and (x_c, y_c, z_c) are the components in the cubed sphere mesh coordinates. After some mathematical simplifications, the analytic form of the Jacobian in cubed sphere mesh is

$$J = \mid T \mid = \frac{v^3 \tau^2}{(1 + {x_c}^2 + {y_c}^2)^{\frac{2}{3}}} \tag{2.16}$$

To analyze the numerical behavior of ray derivatives, I have computed the Jacobian and the relative error on a wavefront in cubed sphere mesh coordinate with two finite-difference methods. The error between the analytic and numerically estimated Jacobian is given by

$$Error = \frac{J - J_a}{J_a} \tag{2.17}$$

where, J is the numerically evaluated Jacobian and J_a is the analytic Jacobian.

Figures (2.7) and (2.8) show the results of the simple single sided forward finite-difference method and the central finite-difference method for the initial meshes of 8 × 8 and 16 × 16 rays on the uppermost surface of the focal cube (Figure 2.3).

The results show that the more initial discretization has the better results and the central finite-difference method has improved in numerical errors, as expected. Also, the significant and very typical grid anisotropy in the forward finite-difference method has been removed by taking central finite-difference method in both cases. This also affects the performance of interpolation tests. As described in the above section, I have chosen the paraxial traveltime perturbation as our interpolation criterion. When I apply this criterion, I tested three different methods of threshold checks utilizing paraxial computation. 1) Taking one corner point with the simple forward finite-

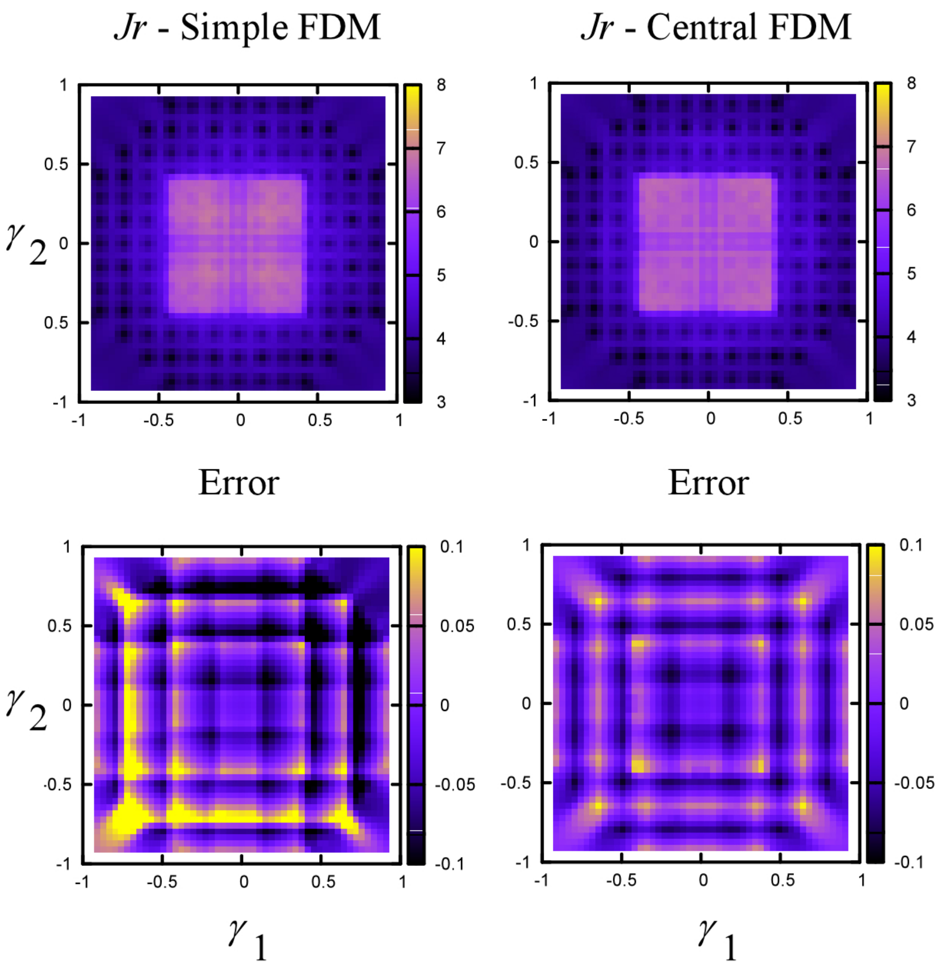

Fig. 2.7. Estimated Jacobian at wavefront of 1.6 seconds and its errors. The initial discretization or initial rays are 8x8 for each focal cube. The results of the simple single side forward finite-difference method are shown in the left and the results of the central finite-difference are shown in the right.

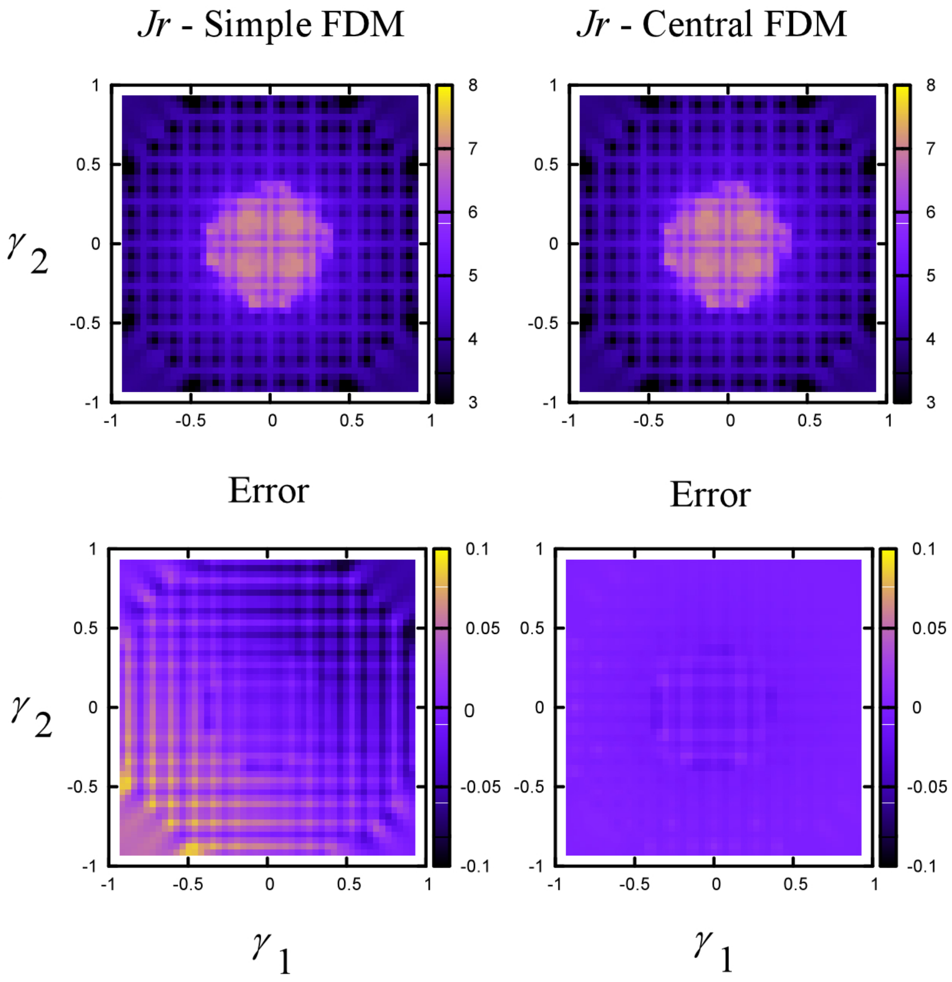

Fig. 2.8. Estimated Jacobian at wavefront of 1.6 seconds and its errors. The initial discretization or initial rays are 16x16 for each focal cube. The results of the simple single side forward finite-difference method are shown in the left and the results of the central finite-difference are shown in the right.

difference method in a wavefront mesh cell, 2) taking four corner points on the mesh cell to estimate paraxial traveltime perturbation for each point with the forward finite-difference and averaging them to make one representative value for the mesh cell, and 3) taking one point and computing paraxial traveltime with the central finite-difference method. The resulting mesh pattern from the first method shows that the interpolated meshes are not evenly distributed (Figure 2.9) and it is very similar with the grid anisotropy pattern in Figures (2.7) and (2.8). When I try to use the second and the third interpolation test , the resulting mesh patterns are evenly distributed (Figure 2.9).

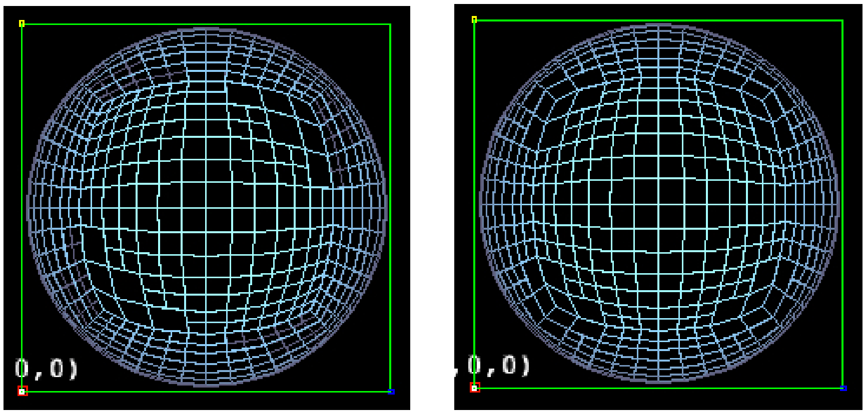

Fig. 2.9. Left: interpolation test with simple forward finite-difference method. Right: interpolation test averaging four points with forward finite-difference method on a mesh cell. The central finite-difference method has similar results with the right.

The numerically evaluated Jacobians in homogeneous and isotropic media for take-off angle mesh coordinates and cubed sphere mesh coordinates on a wavefront are shown in Figure 2.10. The top one in Figure 2.10 shows the very characteristic pattern of the cubed sphere mesh and there are no places with zero values. The lower figure in Figure 2.10 shows conventional take-off angle meshes where the Jacobian values at $\psi \pm 90^\circ$ reached zero. If we calculate the amplitude from the normalized Jacobian,

$$\begin{aligned} J_n &= \frac{J(\tau)}{J(\tau_0)} \propto R \\ A &= \frac{1}{J_n} \propto \frac{1}{R} \end{aligned} \tag{2.18}$$

where $J(\tau)$ is numerically evaluated Jacobian at traveltime τ, $J(\tau_0)$ is the Jacobian at a unit traveltime τ_0, and R is the distance from the source, the zero values in the take-off angle mesh coordinates can be the cause of numerical instability in the computation. To check the numerical behavior of these two mesh generation schemes, error analyses have been performed on both methods. The percent errors between the analytic and the numerical Jacobian have been mapped in Figure 2.11.

The error in the conventional take-off angle mesh (bottom one in Figure 2.11) shows severe numerical instability at or near the pole ($\psi \pm 90^\circ$). However, the results of the cubed sphere mesh (top one of Figure 2.11) show very small amount of errors with the very characteristic pattern. The slightly increased errors with the pattern is caused by the edge effect of the finite-difference implementation. To compute the ray derivatives required in computing the Jacobian, we implemented the central finite-difference scheme whenever all the required neighboring ray components are available. If the conditions for the central finite-difference are not satisfied, the simple forward finite-difference is the next choice. The significant pattern in the error analyses (the top one in Figure 2.11) is the result of the simple forward finite-difference implementation at the edges of the each face on the focal cube, where only single side neighbors are available.

The amplitudes can also be calculated on the surface receiver array by paraxial computation. If we know the traveltime and amplitude at the ray intersection point on the last wavefront before arriving at the surface, the paraxial traveltime correction can be calculated to get the mapped traveltime at the array of surface receivers. If the traveltime on the wavefront is τ and the paraxial traveltime correction to the receiver point from the wavefront is $d\tau$, then the mapped traveltime is $\tau + d\tau$. Recall that the amplitude decreases to the increasing travel distance, $1/A \propto R$, and the travel distance is proportional to the traveltime. If we consider the ratio of the total traveltime arriving at the surface $(\tau + d\tau)$ to the paraxial correction time from the last wavefront to the surface $(d\tau)$, the ratio $d\tau/(\tau + d\tau)$ will be proportional to the

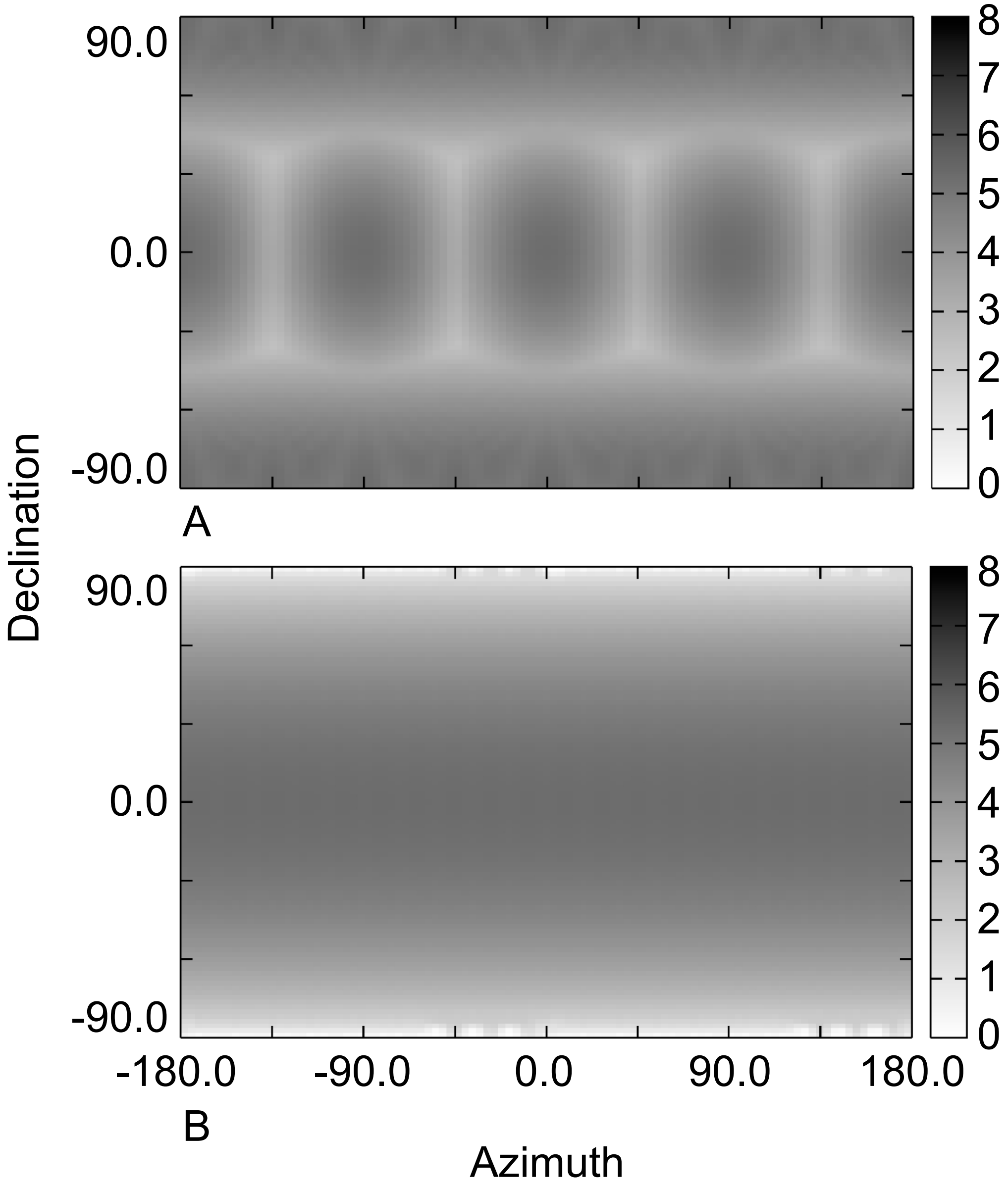

Fig. 2.10. Numerically evaluated Jacobian($1/R$) for homogeneous isotropic media. A: Cubed sphere mesh and B: Take-off angle mesh. Note that the Jacobian in take-off angle mesh coordinate has zero values near ±90° which can cause numerical instability.

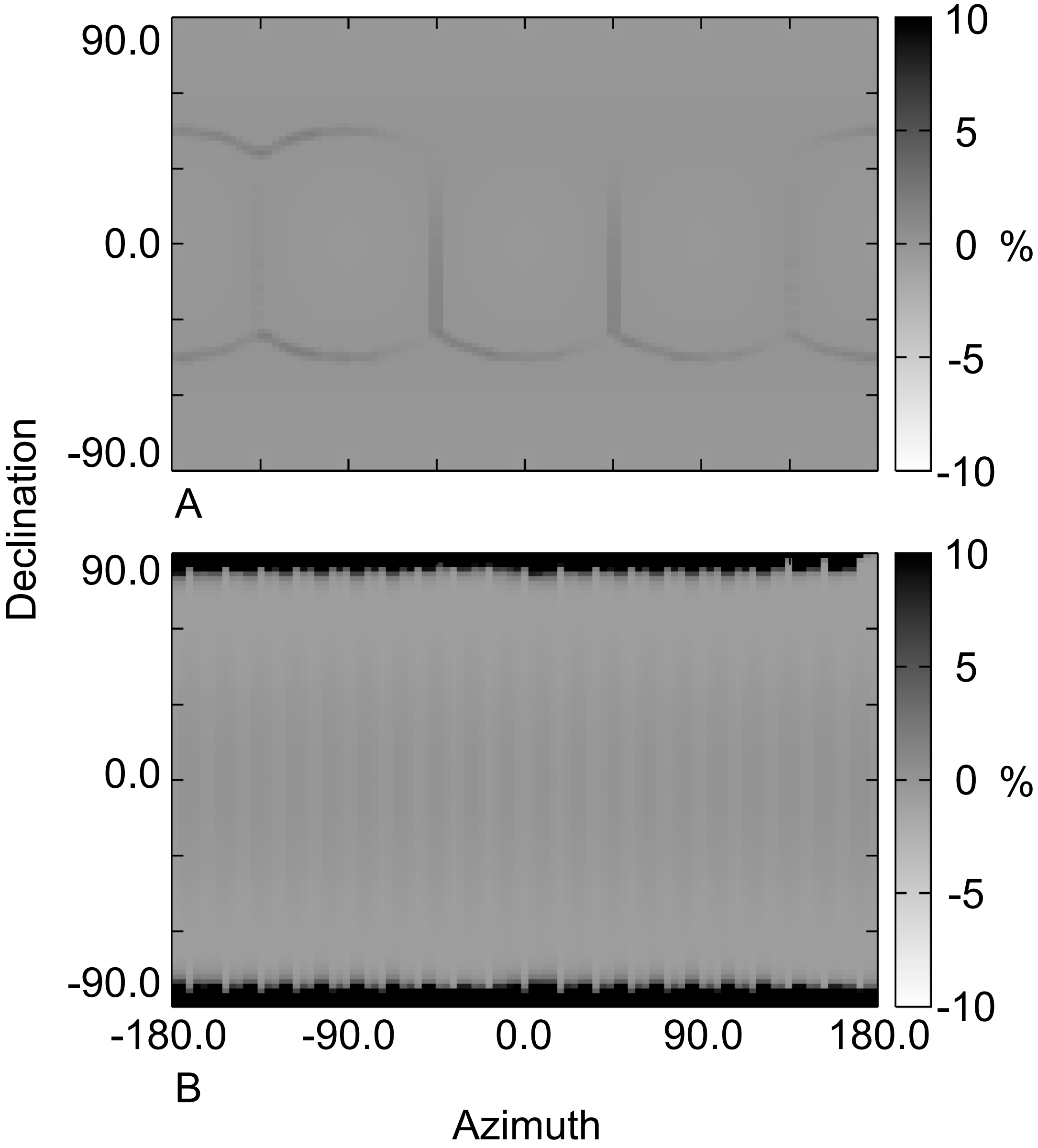

Fig. 2.11. Percent error distribution of normailized Jacobian from between analytic and numerical computation. Note only few percent of errors are distributed along the cube face boundaries. These errors are caused by the differences in the finite-difference method. At the boundaries, the simple single side finite-difference method has been used while central finite-difference method has been used at other points.

negative change in amplitude. The amplitude correction from the last wavefront to the surface will be

$$A_{recv} = A_\tau - A_\tau \left[\frac{d\tau}{\tau + d\tau} \right] \tag{2.19}$$

where A_τ is the amplitude at the ray intersection point on the last wavefront before hitting the model surface and A_{recv} is the corrected amplitude at the receiver on the surface.

Figure 2.12 shows the percent errors of mapped amplitude on the surface array in an isotropic homogeneous medium. The receiver array is composed of 61×61 receivers. Figure 2.12-A is the result of take-off angle mesh coordinates with a total of 9,515 rays after interpolation (≈1,585 rays in surface direction) and Figure 2.12-B is the result of cubed the sphere mesh coordinates with total 9,726 rays after interpolation (≈1,621 rays in surface direction). Note that large errors are located near the center ($\psi = 90°$) in the take-off angle mesh coordinates. The error levels in the cubed sphere mesh is slightly higher, but evenly distributed. Further more, it does not have the large errors resulting from numerical instability near the pole. The assymmetric pattern in the cubed sphere mesh coordinates can be explained by different the finite-difference implementation used to compute the Jacobian as previously described. Some of the wavefront cells are not satisfied with the central finite-difference conditions, and only the simple forward finite-difference scheme is used. Figure 2.13 shows the results of higher number of initial rays [total $\approx 10,080$ rays (1,680 rays in surface direction) for both cases] without interpolation. The average error levels are as low as $< \approx 0.2\%$ for both mesh generation schemes, but we still have numerical instability near the pole in the take-off angle mesh coordinates.

2.4 Conclusion

The wavefront construction method is an efficient modeling tool by explicitly tracking the propagation of wavefronts through a model space instead of tracing of individual rays. By implementing the central finite-difference scheme, the errors introduced by numerically computed ray derivatives have been reduced. Both the wavefront construction and the more traditional ray algorithms suffer from numerical instability and computational inefficiency when the ray take-off angle coordinates is used as the ray parameters. By developing a different set of ray parameters called the cubed sphere mesh coordinates, we have successfully improved the stability and computational efficiency. The proposed ray parameters do not have geometric poles, which is the problem in the take-off angle ray parameters. The analyses of the numerical properties of both ray coordinates systems showed that the proposed cubed sphere mesh ray coordinates system can be used as an alternative for the conventional take-off angle ray coordinate system.

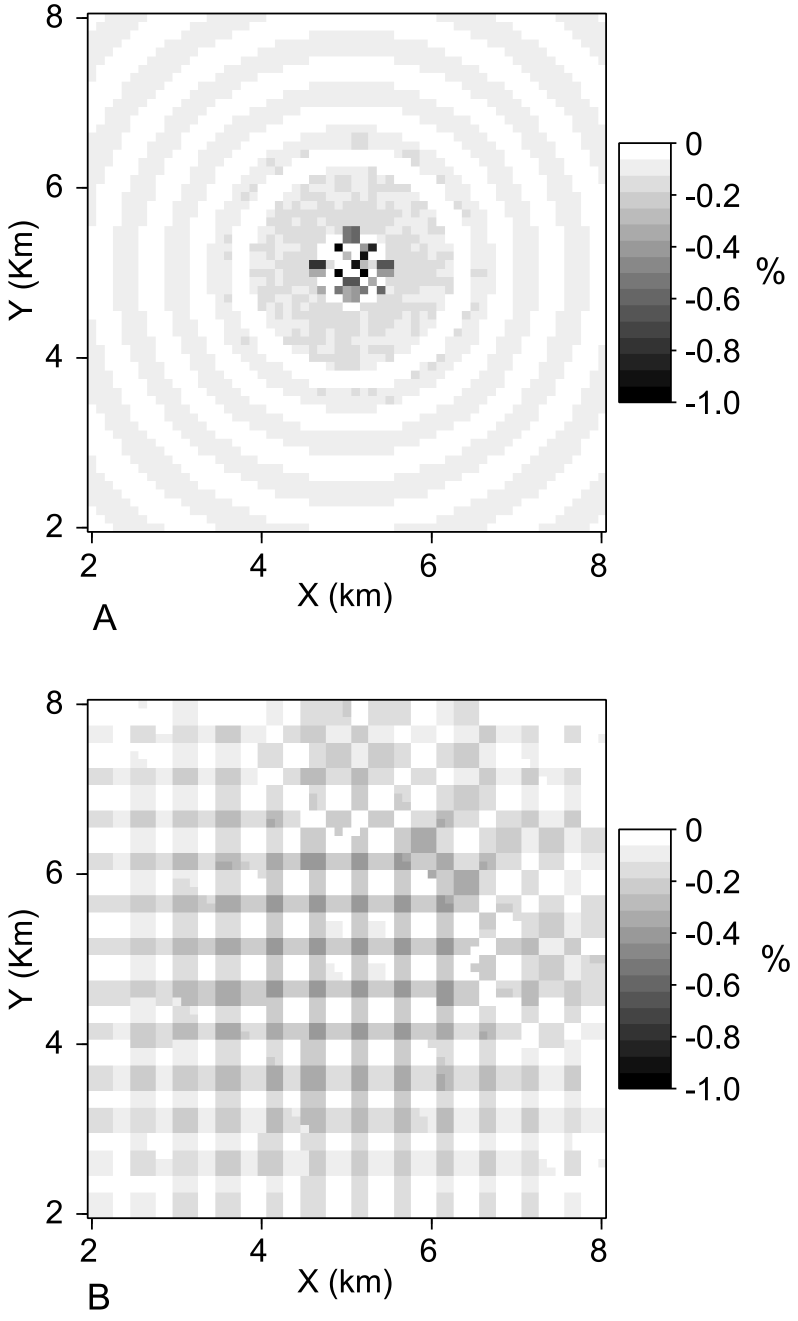

Fig. 2.12. Percent errors of amplitude at the surface receivers. A: Take-off angle mesh of initial 35x76 discretization ended with 9,515 rays after interpolation. Note the numerical instability around the center, which is near the pole. B: Cubed sphere mesh of initial 21x21 discretization ended with 9,726 rays after interpolation. Error levels in the cubed sphere mesh are a little higher than the take-off angle mesh but it does not have any numerical instability near the poles and the error levels are about 0.5% (maximum) in homogeneous isotropic model.

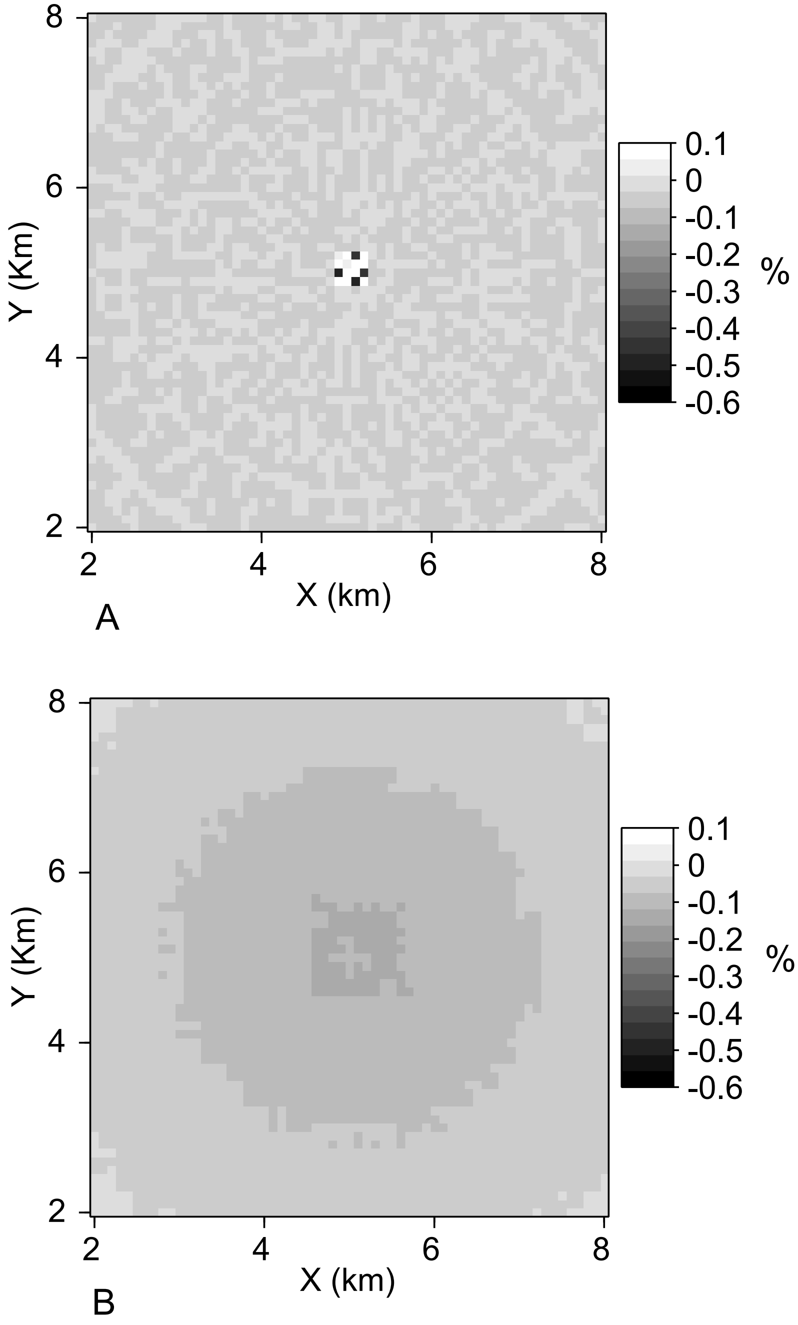

Fig. 2.13. Percent errors of amplitude at the surface receivers. A: Take-off angle mesh of initial 71x142 discretization making 10,082 initial rays without interpolation. Note the numerical instability around the center, which is near the pole. B: Cubed sphere mesh of initial 41x41 discretization making 10,086 rays without interpolation. Error levels in the cubed sphere mesh are a little higher than the take-off angle mesh but it is still numerically stable near the pole and the error levels are about 0.2% (maximum) in homogeneous isotropic model.

CHAPTER III

MODELING AND SYNTHETIC SEISMOGRAMS WITH WAVEFRONT CONSTRUCTION METHOD

Ray tracing is a widely used modeling method in various areas such as traveltime computations for seismic migrations, forward modeling and inverse problems such as tomography (Červený, 2001). Ray tracing methods also allow fast modeling of individual wave types of interest (Červený, 2001). Conventional ray tracing such as the shooting ray method, on the other hand, has well known difficulties in solving two-point problems, especially as model complexity increases in the region. It also suffers from very expensive iterative approach in finding the exact ray path between two points. The paraxial ray tracing method was developed in attempt to address these problems more efficiently (Beydoun and Keho, 1987; Gibson et al., 1991). However, even though the paraxial method is fast and works well in many cases, it has its own limitations associated with selection of ray directions and shadow zones. This is caused by taking separate ray tube based computations without control of ray density over the whole ray field.

One of the other commonly used methods, especially in traveltime estimation, is directly solving the Eikonal equation with numerical methods. The Eikonal solvers are known to be relatively robust and computationally efficient compared to classical ray tracers and have fewer shadow zone problems (Vidale, 1990; Van Trier and Symes, 1991; Kim, 2002). Early developed Eikonal solvers provided robustness and speed but they failed for the later arrivals with strong amplitudes in realistic complicated models (Geoltrain and Brac, 1993). The needs to overcome this weakness led to recent developments in the Eikonal solvers to compute the traveltimes and amplitudes for later arrivals (Qian and Symes, 2002; Buske and Kästner, 2004).

Some other methods have been recently developed such as Huygens wavefront tracing (Sava and Fomel, 2001) and ray tracing with graph theories (Moser, 1991; Cheng and House, 1996; Zhang and Toksöz, 1998; van Avendonk et al., 2001). In Huygens wavefront tracing method, a new wavefront is constructed by finding the next wavefront with a finite-difference computation from the current wavefront. However, it may not be accurate unless a stability condition such as Courant's condition is satisfied (Morton and Mayers, 1994), and it is using 1st order approximations of derivatives. The network ray tracing or shortest ray path method has been developed to overcome the restrictions of the conventional ray tracing such as diffracted ray paths and the paths to shadow zones by taking the shortest or fastest path over a network of subdivided velocity blocks (Moser, 1991). This is also called the graph method because the approach of locating the shortest path is found in the graph theory. The ray paths of shortest traveltime are found by connecting the grid points or nodes and the the grid points act as scatters or secondary sources of the propagating wave as stated in Huygens' principle. This method is stable for finding the global minimum traveltime (Cheng and House, 1996). The major drawback of this method is the computation time of searching the minimum traveltime over the network of cells or velocity blocks (van Avendonk et al., 2001).

The Wavefront construction method is an extension of conventional ray tracing techniques. This method was developed in the early 1990s to improve computational efficiency and overcome the inherited problems of conventional ray tracing systems. Wavefront construction methods compute propagating wavefronts to minimize computational speed and to facilitate tracking of multiple arrivals (Vinje et al., 1993; Lambaré et al., 1996; Lucio et al., 1996; Ettrich and Gajewski, 1996; Gibson, 1999; Vinje et al., 1999; Gibson et al., 2002; Mispel and Williamson, 2001; Lee and Gibson, 2003; Gibson et al., 2005). A quasi-compressional wave modeling using the wavefront construction method was applied in this paper (Gibson, 1999; Gibson et al., 2002; Lee and Gibson, 2003; Gibson et al., 2005). The primary focus of the algorithm is to propagate an initial wavefront through the model space, defined by the mesh of points on a sparse fan of rays, instead of dealing the individual rays. Therefore, it is important to control the ray interpolation on a specific wavefront to obtain accurate results. We have implemented the paraxial traveltime accuracy as the interpolation threshold, which gives more physical ideas than a simple distance or area threshold. Also, we use a rectangular grid with quadrilateral cells for the wavefront mesh, which is more suitable for paraxial computation and easy mapping of the wavefront geometry. In addition to these features, we have also developed cubed sphere mesh coordinates, which can avoid well known pole problems in conventional take-off angle mesh coordinates, while also generating more evenly distributed mesh geometries (Gibson et al., 2002; Lee and Gibson, 2003).

In this paper, examples including anisotropic media are used to demonstrate the validity of the wavefront construction method on various earth models. Also, for realistic application examples and verification of wavefront construction methods, a field Vertical Seismic Profile (VSP) data set from the Gulf of Mexico has been simulated and synthetic seismograms were generated and compared. To generate the synthetic seismograms, Green's tensor quantities (traveltime, amplitudes, and displacement vectors at source and receiver) are computed from the wavefront construction method. These quantities can be used for elastic Kirchhoff type migrations as well as generating synthetic seismograms.

3.1 Background Theory and Method

WFC is an implementation of the ray tracing method. The general idea is that a set of initial rays are traced with take-off directions based on a mesh representing the initial wavefront about the source point, and the wavefront is then propagated in the model space. As the initial set of rays diverges, new rays are inserted in the wavefront to ensure that there is a dense enough set of rays to compute paraxial traveltimes and amplitudes using ray differencing. Thus, the wavefront construction method can be simplified as a three step procedure. The first step is tracing rays according to the initial conditions. The second step is constructing the initial meshes. Generally, conventional take-off angle mesh coordinates are used in step one and two for most cases. However, it is possible to use different kinds of initial meshes such as cubed sphere mesh coordinates (Gibson et al., 2002; Lee and Gibson, 2003). The third step is propagating the wavefront and interpolating new rays if necessary.

3.1.1 Ray Tracing System

To trace the initial rays, solving a set of ray equations is the first step in the wavefront construction method. According to asymptotic ray theory, we can solve the following set of ordinary differential equations (ODEs) for general anisotropic media with numerical ODE solvers such as the Runge-Kutta ODE solver, giving ray paths and traveltimes (Červený, 2001):

$$\begin{aligned}\frac{dx_i}{d\tau} &= a_{ijkl}p_l g_j g_k \\ \frac{dp_i}{d\tau} &= -\frac{1}{2}\frac{da_{ijkl}}{dx_i}p_n p_l g_j g_k,\end{aligned} \tag{3.1}$$

where x_i are spatial coordinate components, τ is traveltime, and the p_i are slowness vector components along the ray path:

$$p_i = \frac{\partial \tau}{\partial x_i}. \tag{3.2}$$

The a_{ijkl} in equation (3.1) is the elastic moduli normalized by density ρ given by

$$a_{ijkl} = \frac{c_{ijkl}}{\rho}. \tag{3.3}$$

The phase velocities and particle motions are calculated by solving the Christoffel equation, $\Gamma_{ik} = a_{ijkl}p_j p_l$ (Červený, 2001).

3.1.2 Ray Amplitude

Solving the transport equation for the amplitude factor, the ray amplitude (Červený, 2001) is

$$A(\tau) = \left[\frac{\rho(\tau_0)v(\tau_0)J(\tau_0)}{\rho(\tau)v(\tau)J(\tau)}\right]^{1/2} A(\tau_0), \tag{3.4}$$

where, ρ is the density, v is the velocity for a wave type, and J is the Jacobian measured at a specific time. In an isotropic homogeneous medium, $\rho(\tau_0) = \rho(\tau)$ and $v(\tau_0) = v(\tau)$, so the equation (3.4) becomes simply

$$A(\tau) = \sqrt{\frac{J(\tau_0)}{J(\tau)}}A(\tau_0) \tag{3.5}$$

The accuracy of computed results can be tested in several ways. For an anisotropic homogeneous medium, the analytic form of the ray amplitude (Pšenčík and Teles, 1996) can be used for the benchmark test of the performance (Mispel, 2001). In this paper, the paraxial ray tracing code (Gibson et al., 1991) has been used to compare the results and to verify the accuracy of the computation by the wavefront construction method.

3.1.3 Mapping on Surface

The wavefront construction results are mapped on the surface by taking each ray tube (or wavefront mesh element) to the surface. By making the final wavefront mesh arrive at the surface (any subsurface reference) of each ray tube, it is possible to map the multiple arrivals.

The ray tube (or wavefront mesh element) is composed of four rays and arriving at the surface without any assumption of hitting any specific receiver locations. Therefore, we have the classic two-point problem in mapping the arriving rays to the receiver positions. The shooting ray method is one classical ray method which is inefficient due to the iterative search of the receiver position. This method has difficulty to implement, especially where multiple arrivals are important. The paraxial ray method (Gibson et al., 1991; Červený, 2001) is essentially another shooting method but it efficiently extrapolates information from a known ray position to nearby locations, reducing the total number of rays and computations. Specifically, the traveltime at a point $\mathbf{x}$ near a point $\mathbf{x^c}$ on a known, central ray is obtained from a Taylor Series expansion with two terms:

$$\tau(\mathbf{x}) \approx \tau(\mathbf{x^c}) + p_i(x_i - x_i^c) + \frac{\partial^2 \tau}{\partial x_i \partial x_j}(x_i - x_i^c)(x_j - x_j^c). \tag{3.6}$$

As shown in this equation, the estimated value depends on the ray derivatives and the distance between the two points. Also, the ray derivatives are obtained from the finite-difference method which uses neighboring rays to compute the derivatives at a point along the given ray. Closer points or more dense rays, in other words, will improve the results. Having sufficiently dense rays near the receiver points, especially at large distance from the source, will result in highly sampled ray shooting near the source. The wavefront construction method is designed to avoid the unnecessarily dense rays near the source by inserting new rays examining the physical conditions such as distance, area of a ray tube cross-section (or wavefront mesh element), slowness perturbations, or paraxial traveltime perturbations. In this paper, we have implemented the paraxial traveltime perturbation for the interpolation threshold based on equation (3.6). More details on the interpolation threshold are described in Gibson et al. (2005).

Figure 3.1 shows the mapping procedure by estimating paraxial correction traveltime as described in equation (3.6). The wavefront time arriving at the surface

τ_{surf} of the ray tube at the reference point is extrapolated by estimating the paraxial correction traveltime $d\tau$ to get the traveltime at the receiver τ_{recv}.

The amplitudes can also be calculated on the surface receiver array by the paraxial computation. If we know the traveltime and amplitude at ray intersection point on the last wavefront before arriving at the surface, the paraxial traveltime correction can be calculated to get the mapped traveltime on the surface of receiver array. If the traveltime on the wavefront is τ and the paraxial traveltime correction to the receiver point from the wavefront is $d\tau$, then the mapped traveltime is $\tau + d\tau$. Recall that the amplitude decreases in increasing travel distances, $1/A \propto R$, and the travel distance is proportional to the traveltime. If we consider the ratio of the total traveltime arriving at the surface $(\tau + d\tau)$ to the paraxial correction time from the last wavefront to the surface $(d\tau)$, the ratio $d\tau/(\tau + d\tau)$ is proportional to the negative change in amplitude. The amplitude correction from the last wavefront to the surface will be

$$A_{recv} = A_\tau - A_\tau \left[\frac{d\tau}{\tau + d\tau} \right] \tag{3.7}$$

where A_τ is the amplitude at the ray intersection point on the last wavefront before arriving at the model surface and A_{recv} is the corrected amplitude at the receiver on the surface for isotropic homogeneous media. For a short distance in computing paraxial correction for receivers, it is close to use this form in general weak anisotropy and weak heterogeneity.

3.1.4 Green's Tensor and Synthetic Seismograms

Synthetic seismograms are obtained from Green's tensor, traveltime, amplitude, and displacement vectors at the source and receiver positions. The high frequency, far-field form of the Green's tensor for isotropic or anisotropic media in the frequency domain is (Ben-Menahem et al., 1991)

$$G_{jm}^{(\eta)}(\vec{r}|\vec{r}_0) = \sum_{\eta=1}^{3} \frac{1}{4\pi v_\eta^2} e^{-iw\tau^{(\eta)}} g_j^{(\eta)}(\vec{r}) g_m^{(\eta)}(\vec{r}_0) A^{(\eta)}(\vec{r}|\vec{r}_0), \quad \eta = 1, 2, 3 \tag{3.8}$$

where the jm component represents the j component of displacement observed at $\vec{r}$ and radiated by a point force applied at $\vec{r}_0$ in the m direction. η is the three types of waves: one quasi-compressional wave (qP) and two quasi-shear (qS) waves, $g_i^{(\eta)}(\vec{r})$ is the unit polarization vectors for the corresponding wave types: $g_i^{(1)}$ is the unit

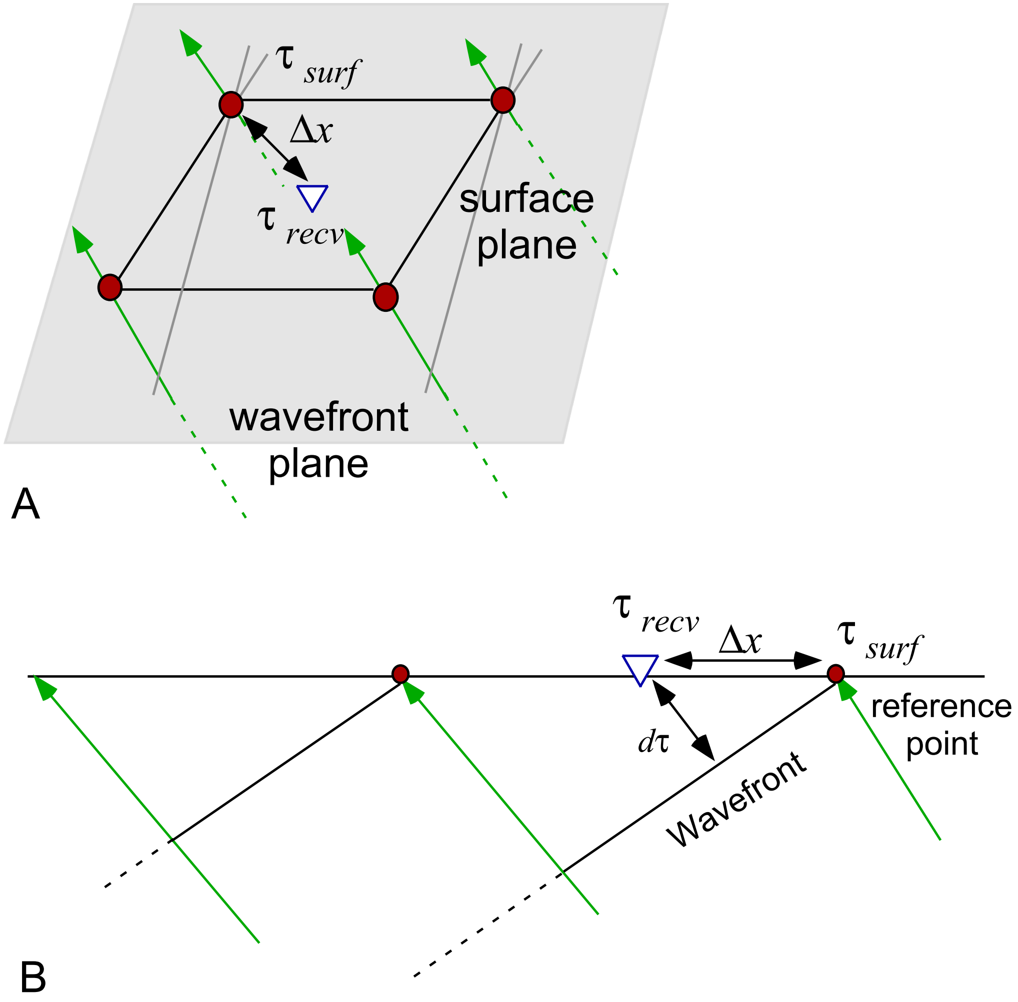

Fig. 3.1. Mapping of rays arriving at the surface with the paraxial approximation.The wavefront time arriving at the surface τ_{surf} of the ray tube at the reference point is extrapolated by estimating the paraxial correction traveltime $d\tau$ to get the traveltime at the receiver τ_{recv}.

polarization vector of the quasi-compressional wave and others are of two quasi-shear waves. v_η is the velocity of the corresponding wave type. $A^{(\eta)}$ is the scalar amplitude function of each wave type and τ is the traveltime from the source to the receiver.

Knowing $\mathbf{G}$, we may calculate the medium's response $\vec{u}$ to an arbitrary point-force $\vec{F}$:

$$u_j = G_{jm}F_m \tag{3.9}$$

3.2 Homogeneous Model Experiments

The accuracy of synthetic seismograms computed with the wavefront method can be verified by comparisons to analytic solutions for homogeneous media and to independent numerical results for transversely isotropic media with a vertical axis of symmetry.

3.2.1 Isotropic Model Test

An isotropic homogeneous model is used to ensure the computed quantities are satisfied in the error bound near the numerical error levels. The model geometry is shown in Figure 3.2. This simplest model has $V_p = 2.0$ km/sec, $\rho = 1.0$ (g/cc), and $V_p/V_s = 1.8$. The size of model is $10 \times 10 \times 10$ (km) with the source located at x=1.0 (km), y=5.0 (km), and z=5.0 (km). The 6×6 matrix of density normalized elastic moduli for this model is

$$C_{mn} = \begin{pmatrix} 4 & 1.53086 & 1.53086 & 0 & 0 & 0 \\ 1.53086 & 4 & 1.53086 & 0 & 0 & 0 \\ 1.53086 & 1.53086 & 4 & 0 & 0 & 0 \\ 0 & 0 & 0 & 1.23457 & 0 & 0 \\ 0 & 0 & 0 & 0 & 1.23457 & 0 \\ 0 & 0 & 0 & 0 & 0 & 1.23457 \end{pmatrix}. \tag{3.10}$$

Figure 3.3 shows an example of the ray paths in the wavefront construction modeling of isotropic homogeneous medium where the source is located at the left of the model space. This figure shows where new rays are inserted into the ray field as the trajectories diverge at increasingly large distances. Computed traveltimes on the surface and the traveltime difference between exact traveltime are shown in Figures 3.4 and 3.5. Due to the insertion of new rays for the far offset arrival rays, we have slightly higher errors. Although the error is slightly worse when rays are interpolated, the wavefront construction method is still a useful algorithm because the traveltime error is less than 5.0×10^{-6} which is much less than the preset traveltime threshold 1.0×10^{-2} for wavefront mesh interpolation in wavefront construction code.

Computed amplitudes and the amplitude differences between the exact values are shown in Figures 3.6 and 3.7. The analytic amplitude in this computation is $1/R$, where R is the distance from the source to the receiver. The results of both traveltime and amplitude differences show that the wavefront construction code is working with high accuracy levels of numerical errors in an isotropic homogeneous medium.

3.2.2 Green River Shale - VTI Model

Vertical Transverse Isotropic (VTI) medium is one of the most common type of anisotropy in the earth (Thomsen, 1986). This type of anisotropy may be an intrinsic property of a rock, or it may be caused by fine-scale layering. In either case, the material is transversely isotropic with a vertical axis of symmetry. Thomsen (1986) has analyzed various measurements on anisotropy of common type of rocks in petroleum environments. He found that most common types of anisotropy in seismology are weak (10-20%). He summarized and introduced a simpler set of parameters known as Thomsen's parameters describing transversely isotropy with vertical axis of symmetry (VTI). The vertical transverse isotropy is basically a hexagonal isotropy which has the following form of the elastic moduli (6 × 6 matrix in Voigt notation).

$$C_{mn} = \begin{pmatrix} C_{11} & C_{11}-2C_{66} & C_{13} & & & \\ & C_{11} & C_{13} & & & \\ & & C_{33} & & & \\ & & & C_{44} & & \\ & & & & C_{44} & \\ & & & & & C_{66} \end{pmatrix} \tag{3.11}$$

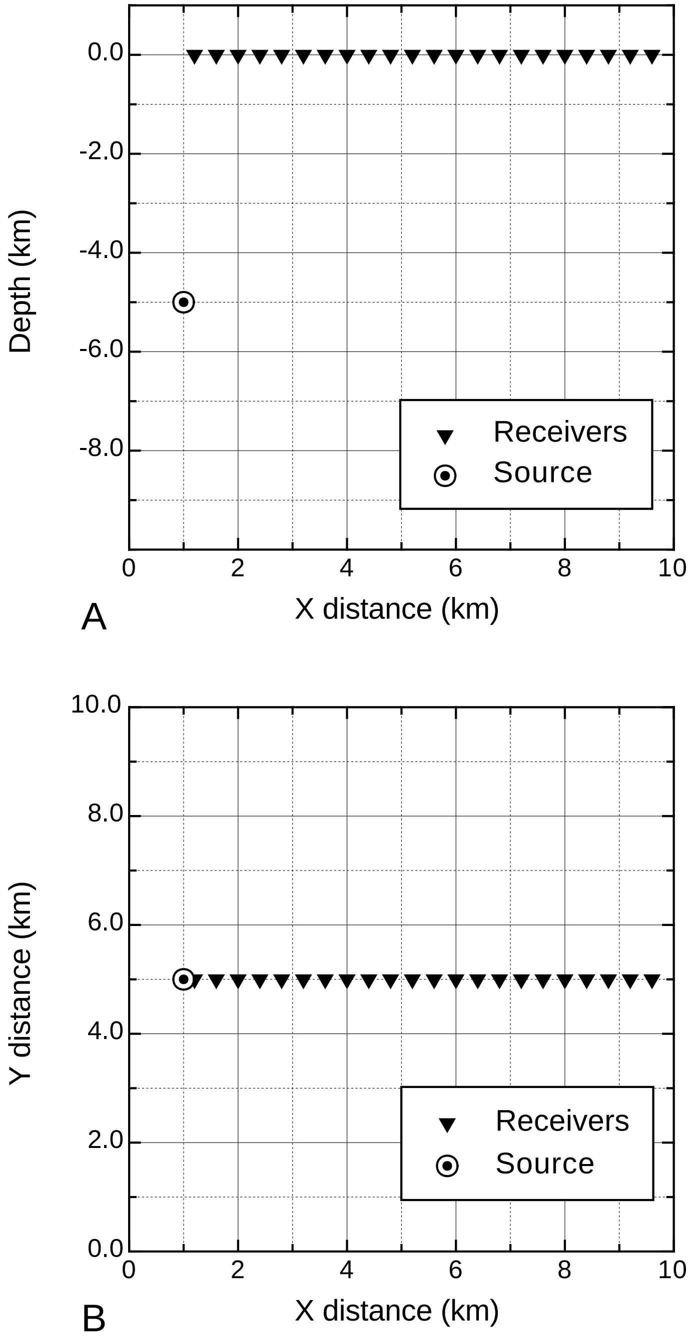

Fig. 3.2. Source and receiver geometry of the homogeneous models. The source is located at the left side at 5 km depth and the receivers are located along the middle of the surface.

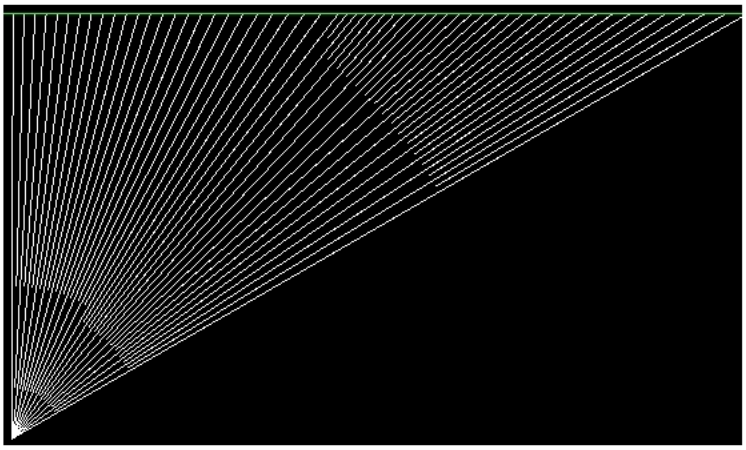

Fig. 3.3. Wavefront construction modeling of isotropic homogeneous medium with the source located at the left of the model space (only ray paths are displayed). New rays are inserted at several distances as the rays diverge away from the source location.

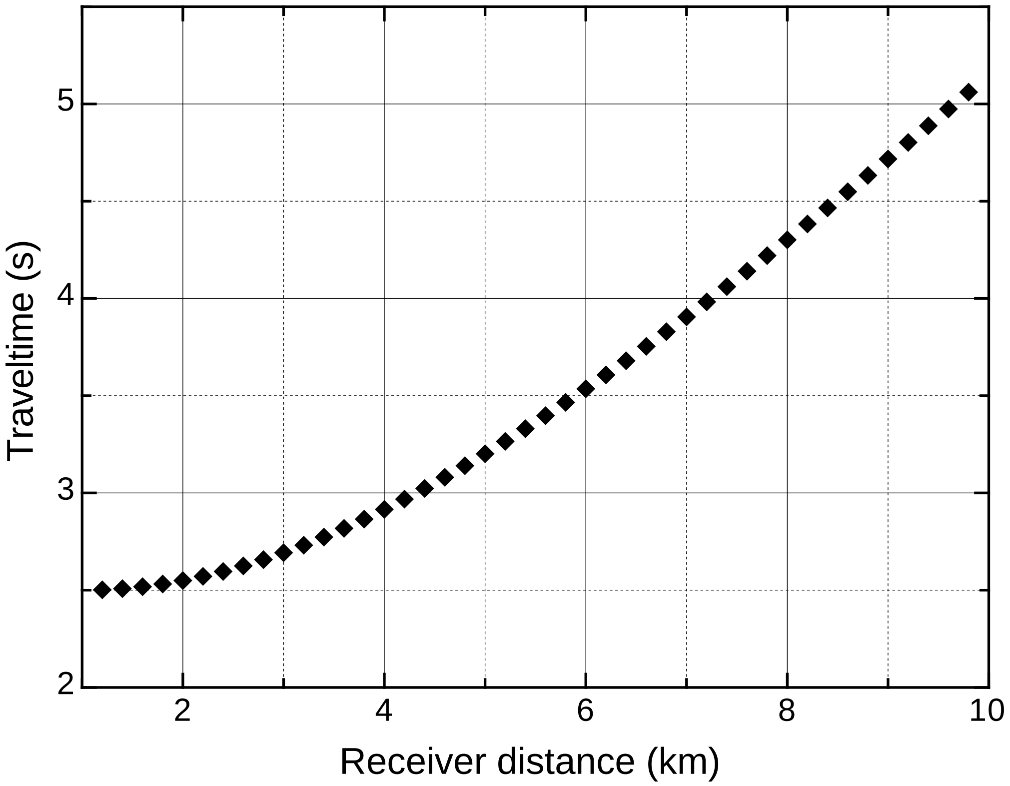

Fig. 3.4. Traveltime results for the isotropic homogeneous medium with the model geometry in Figure 3.2.

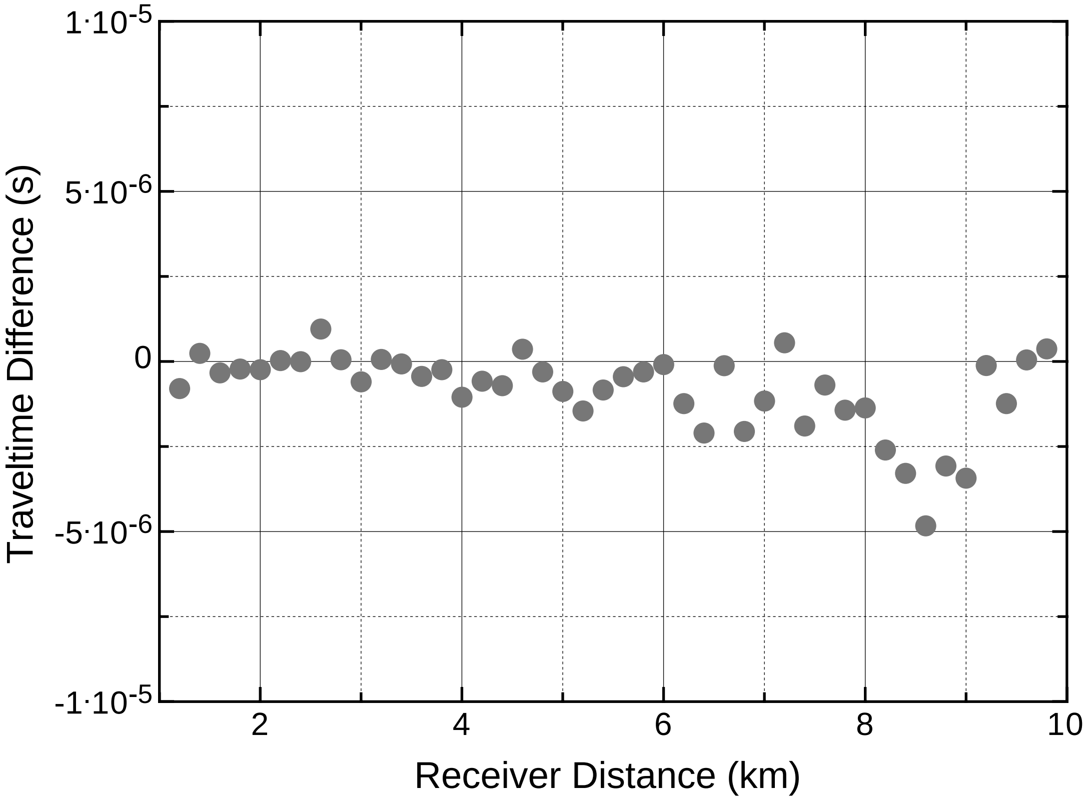

Fig. 3.5. Difference of traveltime values computed with the wavefront construction method and the analytically computed traveltime for an isotropic homogeneous medium. The maximum difference is less than 5.0×10^{-6} seconds. Figure 3.3 shows how the new rays are inserted between the rays at larger distances from the source.

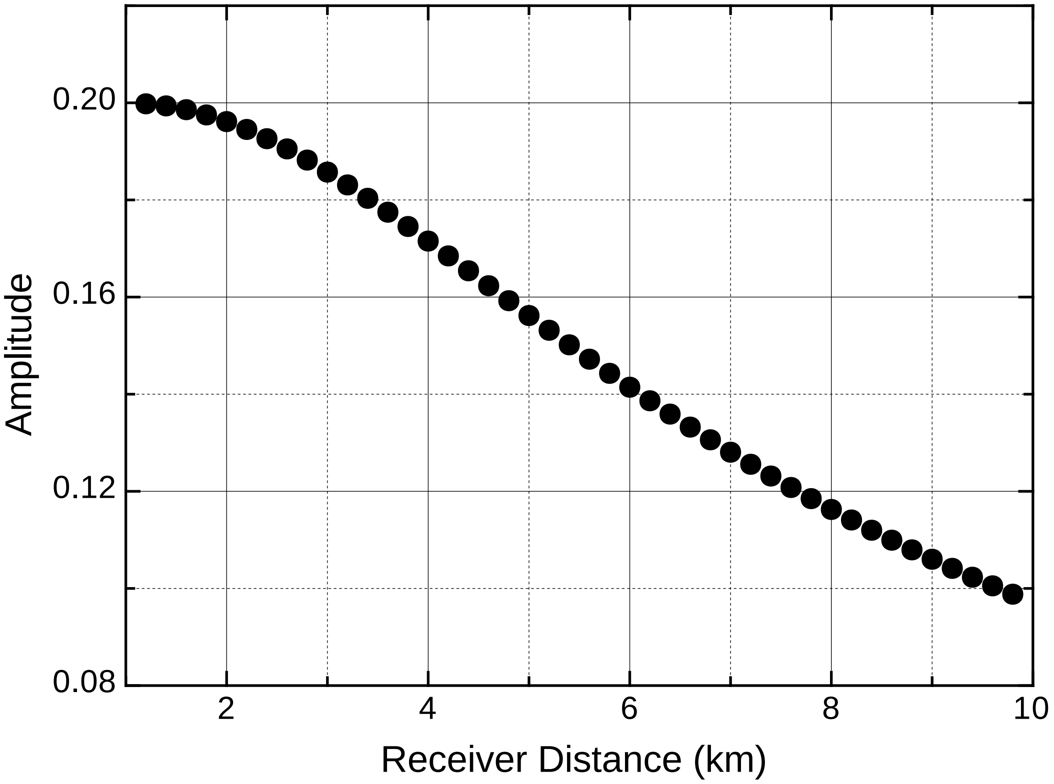

Fig. 3.6. Mapped amplitude $1/R$, where R is the distance from the source to the receiver point.

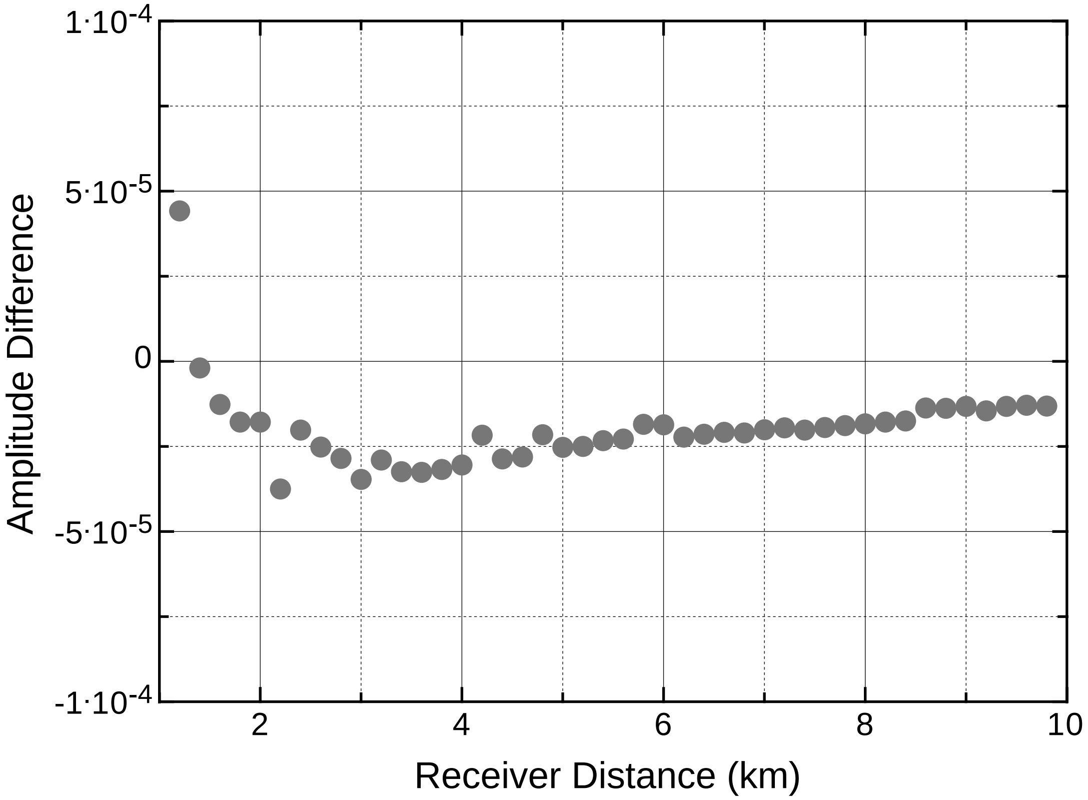

Fig. 3.7. Differences between the mapped amplitude and the exact amplitude. The difference is less than 5.0×10^{-6}.

The Thomsen's parameters are

$$\begin{aligned} \epsilon &\equiv \frac{C_{11} - C_{33}}{2C_{33}} \\ \gamma &\equiv \frac{C_{66} - C_{44}}{2C_{44}} \\ \delta &\equiv \frac{(C_{13} + C_{44})^2 - (C_{33} - C_{44})^2}{2C_{33}(C_{33} - C_{44})} \end{aligned} \tag{3.12}$$

The vertical P- and S-wave velocities are

$$\begin{aligned} V_p &= \sqrt{\frac{C_{33}}{\rho}} \\ V_s &= \sqrt{\frac{C_{44}}{\rho}} \end{aligned} \tag{3.13}$$

The phase velocity of quasi-P wave in terms of Thomsen's parameter and the angle, θ, from the vertical axis is

$$V_p(\theta) = v_p \left[1 + \delta sin^2\theta cos^2\theta + \epsilon sin^4\theta\right] . \tag{3.14}$$

The observed non-dimensional parameters, ϵ, β, and γ, are usually small enough and the anisotropic quasi-compressional velocity [equation 3.14] are not much different from the quasi-compressional vertical velocity [equation 3.13].

Green River shale is one example of the VTI media of weak anisotropy. The Tertiary Green River formation is located in Colorado and well studied for its stratigraphy and anisotropy. Thomsen's parameters for Green River shale are taken from the table of Thomsen's 1986 paper. The parameters are $\epsilon = 0.025$, $\delta = 0.055$, and $\gamma = 0.030$. The following moduli are the density normalized 6×6 matrix ($\rho = 2.31$) used in the wavefront construction simulation.

$$C_{mn} = \begin{pmatrix} 20.365 & 6.49812 & 7.08713 & 0 & 0 & 0 \\ 6.49812 & 20.365 & 7.08713 & 0 & 0 & 0 \\ 7.08713 & 7.08713 & 19.3952 & 0 & 0 & 0 \\ 0 & 0 & 0 & 6.66676 & 0 & 0 \\ 0 & 0 & 0 & 0 & 6.66676 & 0 \\ 0 & 0 & 0 & 0 & 0 & 6.93343 \end{pmatrix} \tag{3.15}$$

I have used the same source and receiver geometry as in isotropic model experiment (Figure 3.2). The traveltimes (Figure 3.8) are computed on the surface receivers and compared with the analytic traveltimes using group velocities in the corresponding ray directions (group velocity direction). The traveltime errors in Figure 3.8-B show that the traveltimes are correctly measured and the maximum error is less than 5.0×10^{-6} seconds. This error level falls into the numerical errors in most systems.

3.2.3 Isotropic, Low Velocity Inclusion Model

An earth model including a low velocity region with spherical symmetry has also been utilized to test wavefront construction code. Figure 3.9 shows the velocity distribution in x-z plane, where the velocity variation is defined using a Gaussian function:

$$C'_{ij} = C_{ij} \left[1 - 0.8\, e^{-\{(x-x_c)^2+(y-y_c)^2+(z-z_c)^2\}} \right] . \tag{3.16}$$

Here the C'_{ij} are the elastic moduli of low velocity region, C_{ij} are the background elastic moduli, x_c, y_c, and z_c are the coordinates of the center of the low velocity zone. This reference point has coordinates $(x, y, z) = (5, 5, 4)$ (all space coordinates have units of kilometers). The background velocity is set to a value of $V_p = 2.0$ km/s for the isotropic medium. Simulations applied a source located at $(x, y, z) = (5, 5, 9)$. The distribution of receiver points is illustrated in Figure 3.10.

Figures 3.11 and 3.12 display the snap shots of the propagating wavefronts of gradient low velocity zone model. It is very clear that we will have crossings at the center of the model space after some wavefront propagation steps have passed. In Figure 3.11, the initial narrow strip of wavefront has been propagated through the

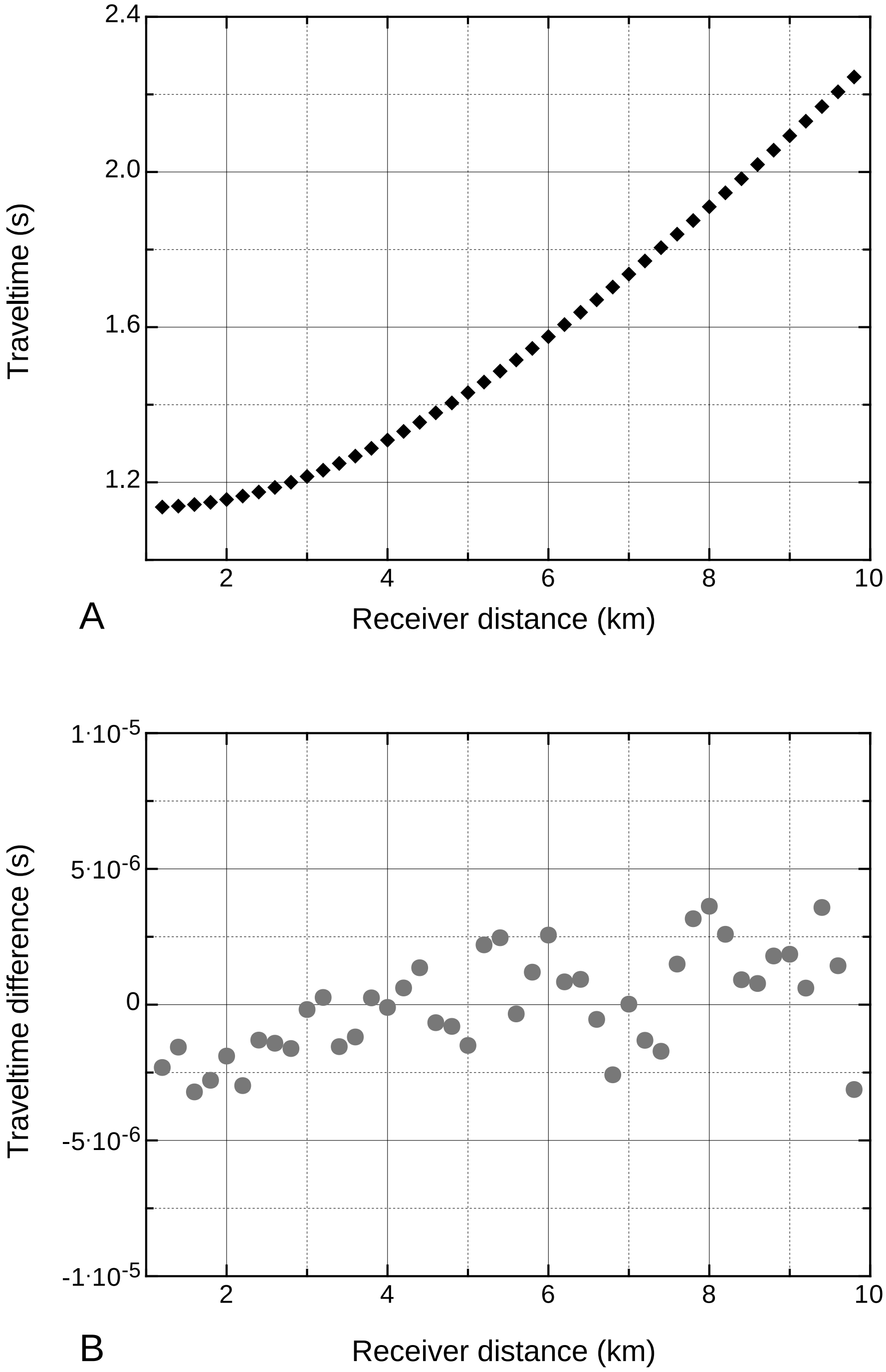

Fig. 3.8. Difference between wavefront and independently computed traveltimes in Green River shale, homogeneous VTI, model simulation. The maximum difference is bounded less than 5.0×10^{-6}.

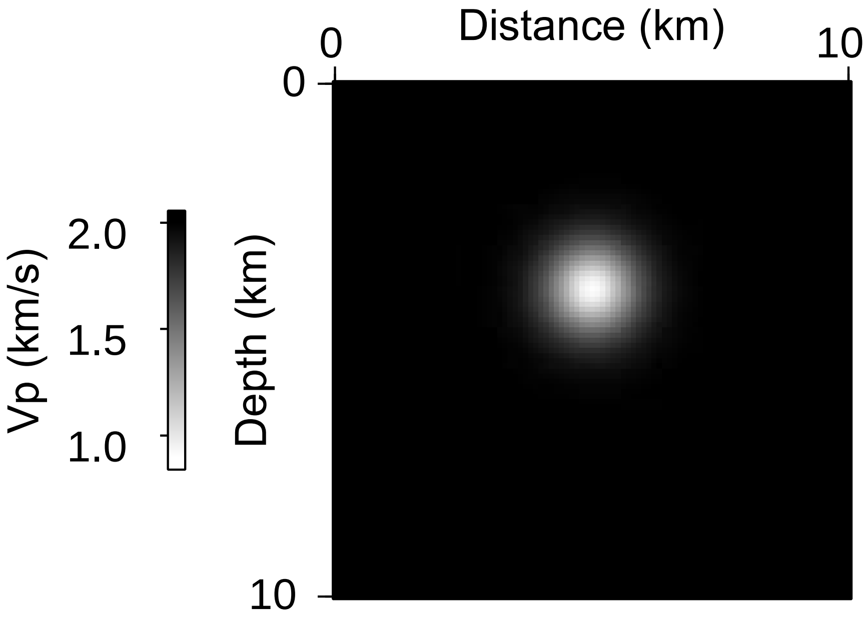

Fig. 3.9. Velocity distribution of the low velocity sphere model with constant background velocity.

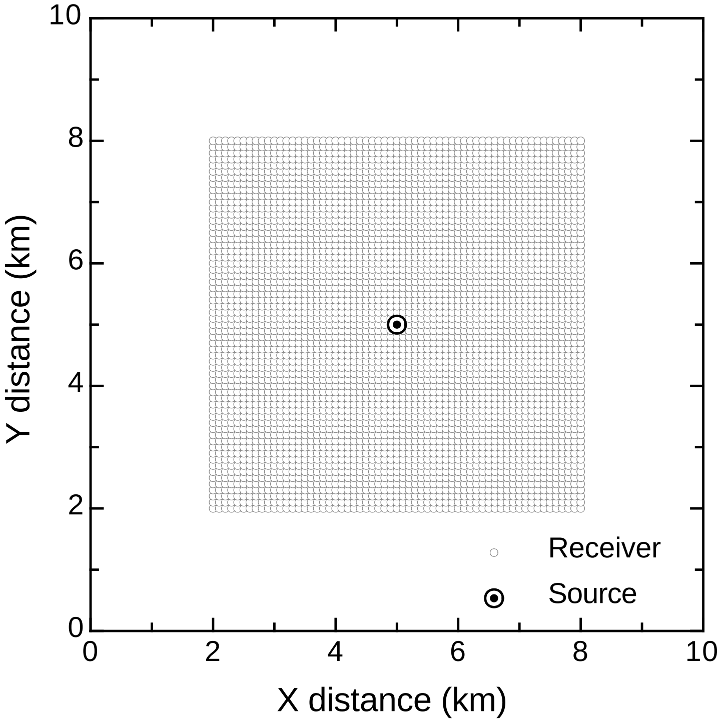

Fig. 3.10. The source and receiver geometry map of the isotropic low velocity blob model. The source is located at the center with a 9 km depth and the receivers are located on the surface from x = y = 2 km to x = y = 8 km with 100 m distance.

model space. At around 2.5 seconds the wavefront started to convex at the center and distorted at around 3.3 seconds. At 3.8 seconds, one can observe the wavefront has been crossed after passing the caustic point making triplication of the wavefront. The wavefronts in Figures 3.11 and 3.12 visualize caustics caused by high velocity gradient across the center of the low velocity region. Figure 3.13 shows some of the ray paths in this model. Rays from the source are bending and crossing each other when they pass the caustic region. The computed traveltimes in Figure 3.14 show the triplication with all the three arrivals at all distances from the center (x = y = 5 km) of the model space.

3.2.4 Gulf of Mexico VSP Model

A multi-component vertical seismic profile data from the Gulf of Mexico (GoM) was processed and studied for the image resolution analysis by Tzimeas (2004) and the anisotropy studies based on traveltime error minimization with the wavefront construction method were performed by Durussel (2002) and Gibson et al. (2005). Tertiary sands at 580 m (1,900 ft) and 1,036 m (3,400 ft) are the hydrocarbon producing formations in the research area (Constance et al., 1999). The salt dome extends to the surface and the faults around the dome are associated with the salt. The surrounding sediments around the salt body are sandstones and shales. Shale formations are often anisotropic (Sayers, 1999), so the seismic velocity anisotropy may be strong in this area.

Durussel (2002) and Gibson et al. (2005) have performed analysis on seismic velocity anisotropy based on the traveltime error estimation with the anisotropic wavefront construction method. The acquisition geometry of these studies is shown in Figure 3.15. Receivers were located on circular arcs, while sources were placed on radial lines extending from a point over the center of the salt dome. The receiver well is also near the salt dome.

They set a model with vertical and horizontal gradients for isotropic and anisotropic elastic moduli. With a simple grid search for minimum errors between the estimated traveltimes from the wavefront construction method and the measured traveltime, they reached the gradient velocity model shown in the figure on page 60 and a set of Thomsen's parameters.

Synthetic seismograms were computed for this model using the ray theoretical

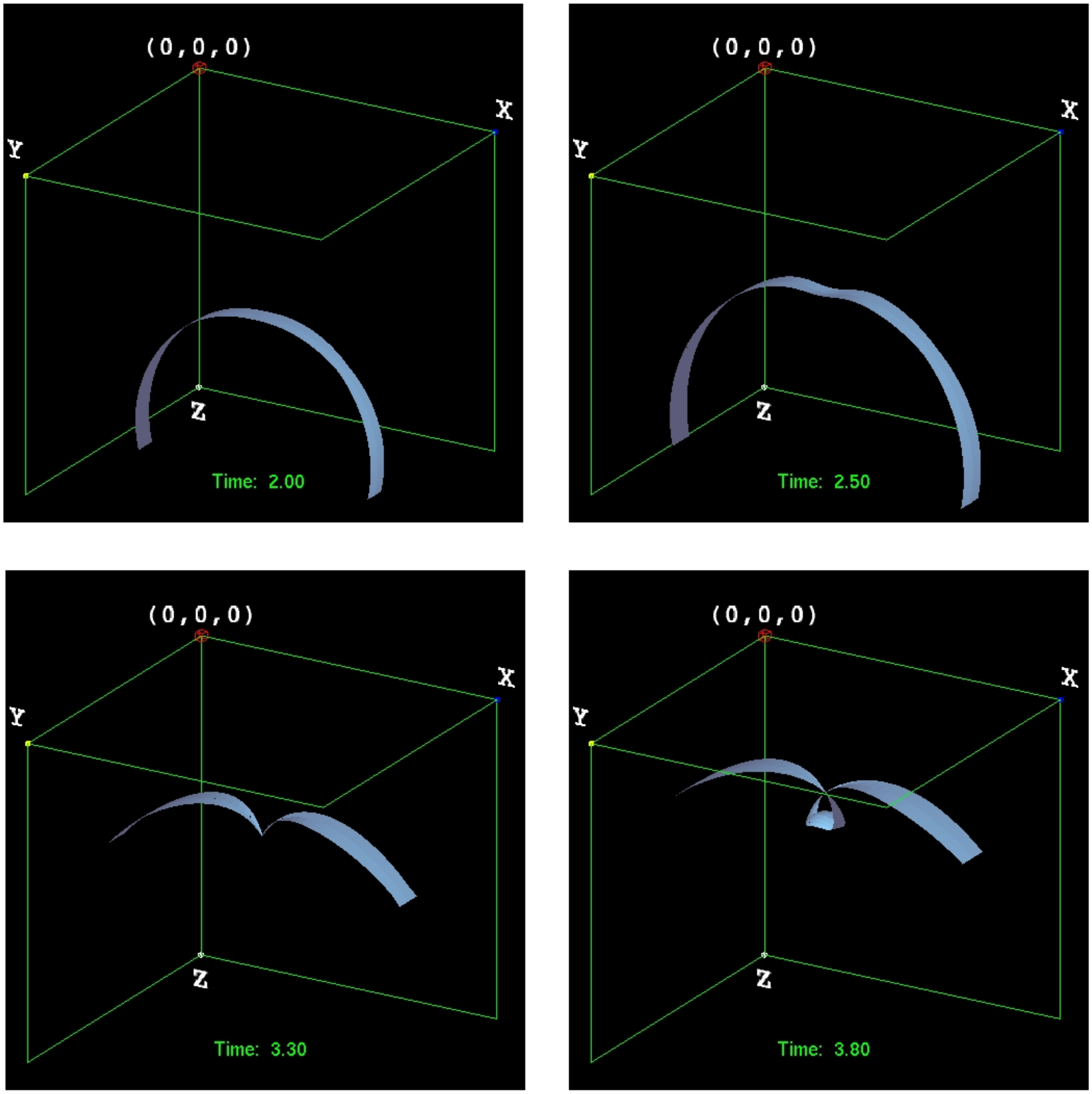

Fig. 3.11. A narrow strip of wavefront has been generated to make the initial wavefront and propagated through the model space.

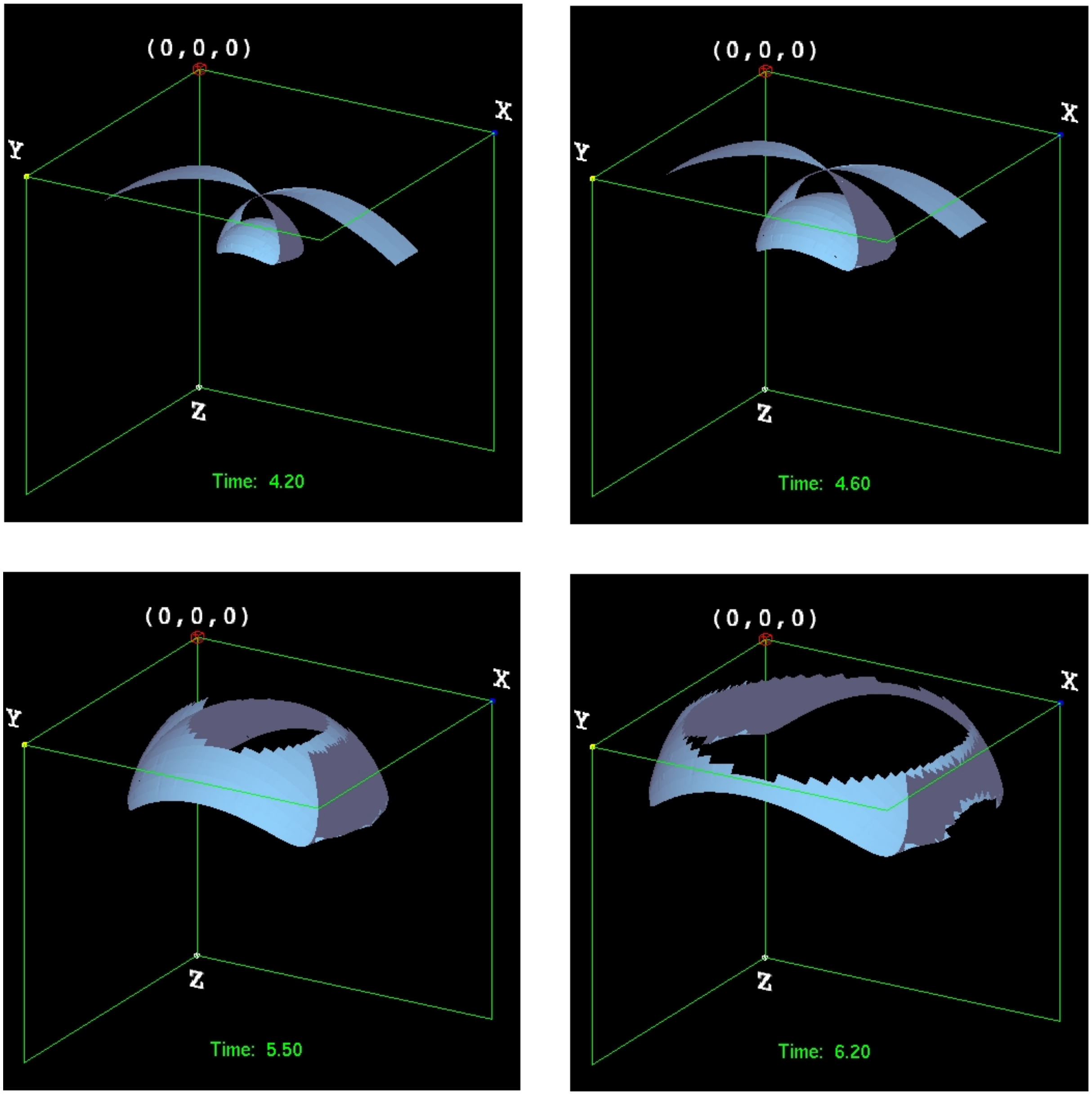

Fig. 3.12. A narrow strip of wavefront has been generated to make the initial wavefront and propagated through the model space. The fast wavefronts arrive at the surface and reveal the caustic shadow.

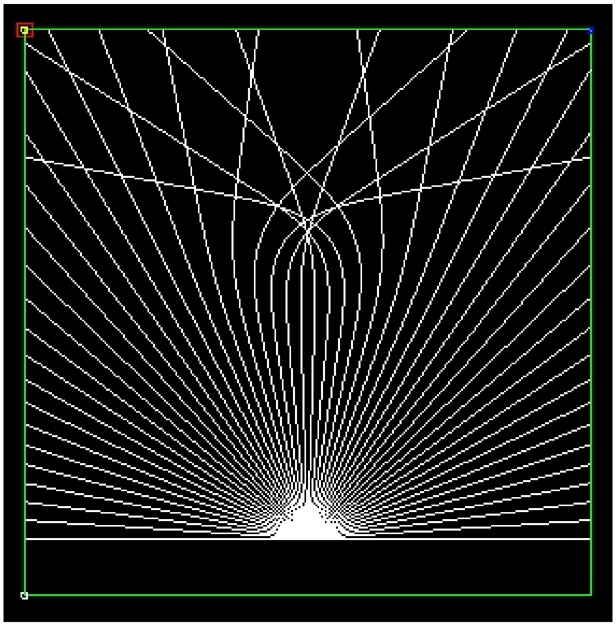

Fig. 3.13. Some ray paths showing caustics in the gradient low velocity blob sphere model. Rays from the source are bending and crossing near the caustic point where the velocity gradient is high.

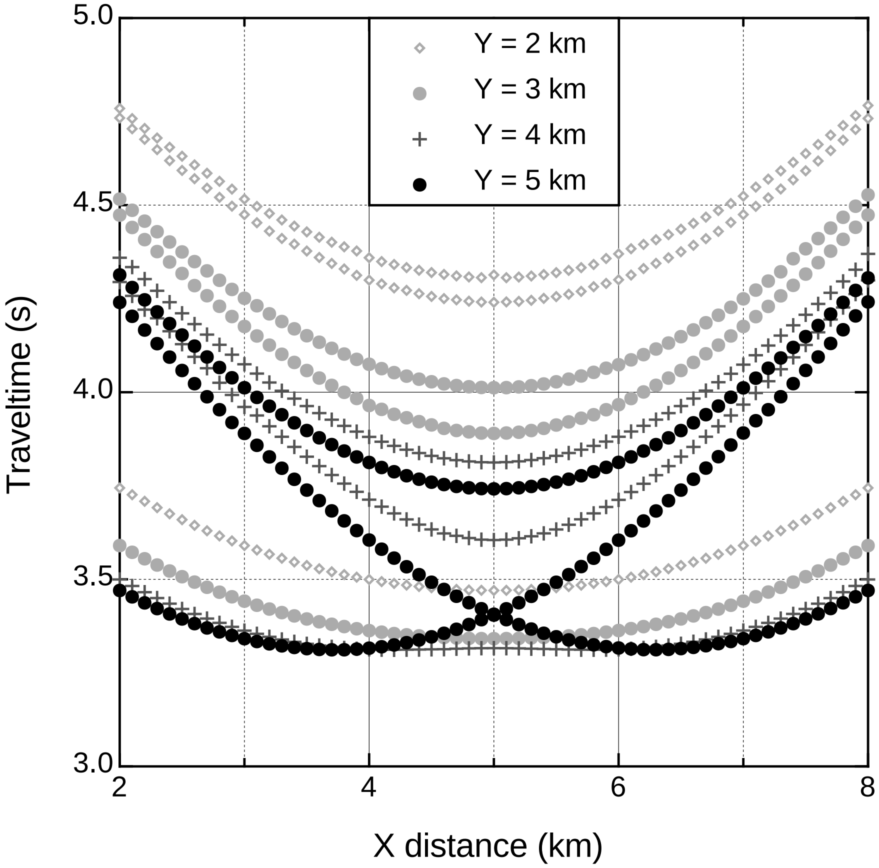

Fig. 3.14. Traveltime results for a few receiver lines within the receiver array (Fig. 3.10). Each line of receivers is parallel to the $x-$axis and has the indicated $y-$coordinate. Three arrivals are detected by each line of receivers.

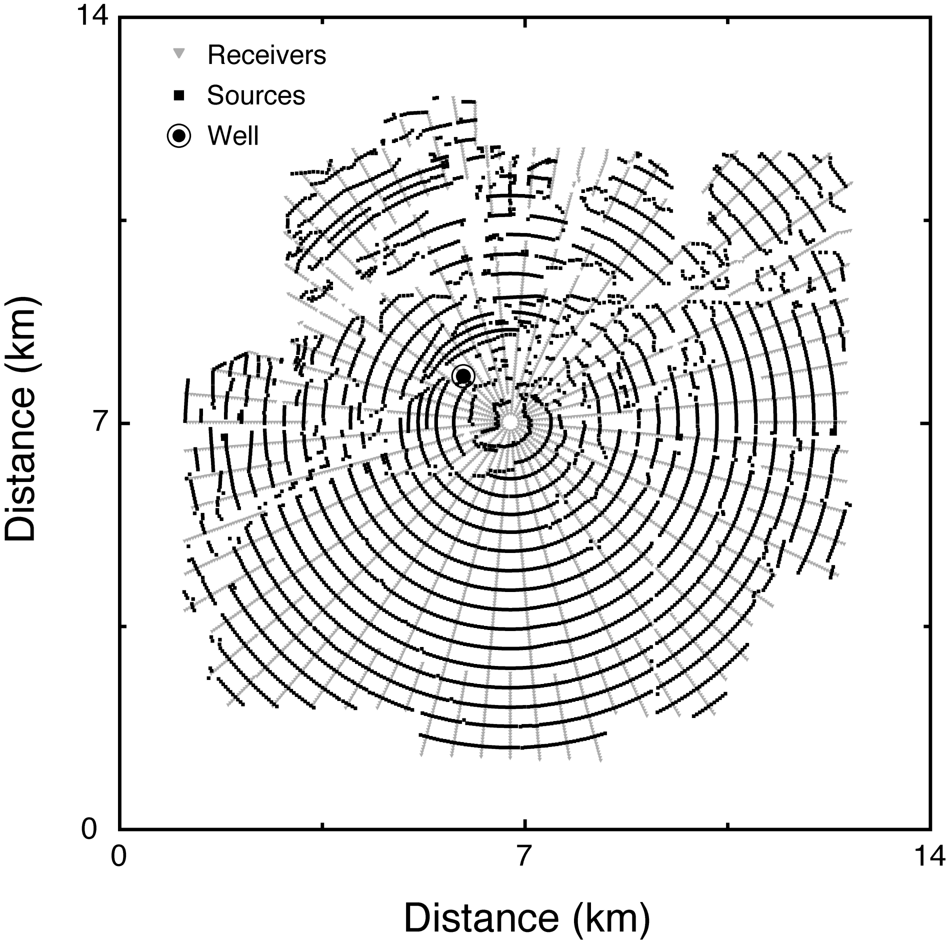

Fig. 3.15. Acquisition geometry of VSP experiments in the Gulf of Mexico salt dome area (Constance et al., 1999; Gibson et al., 2005).

Green's tensor with a explosive source (equation 3.8) (Ben-Menahem et al., 1991). Generating synthetic seismograms and comparing them with the field data helps to confirm the suitability of the application of wavefront construction method to the earth model because it includes all the computation outputs of the wavefront construction method. Computing synthetic seismograms also provides more thorough tests of the accuracy and/or validity of an earth model than just comparing travel-times only.

From the 65 source locations, a near-, mid-, and far-offset source (shot number 5, 21, and 60) were used to compute the synthetic seismograms and are compared with the field data. The velocity profile and the ray paths corresponding to the above three offset data are shown in Figure 3.16. The Thomsen's parameters and elastic moduli found with grid search algorithm (Durussel, 2002; Gibson et al., 2005) are used as the model's input parameters for the wavefront construction code in this paper (Table 3.1).

Table 3.1. Estimated Thomsen's parameters, density and velocities for the VSP data set (Gibson et al., 2005).

Parameters	**Estimated Values**
ϵ	0.045
δ	-0.08
γ	-
ρ	2.7
V_p at surface	1.94365
$\frac{V_p}{V_s}$	1.8

The density normalized 6×6 elastic moduli ($\rho = 2.7$) computed from the Thomsen's parameters are

$$C_{mn} = \begin{pmatrix} 4.14473 & 1.09334 & 1.13109 & 0 & 0 & 0 \\ 1.09334 & 4.14473 & 1.13109 & 0 & 0 & 0 \\ 1.13109 & 1.13109 & 3.8025 & 0 & 0 & 0 \\ 0 & 0 & 0 & 1.17361 & 0 & 0 \\ 0 & 0 & 0 & 0 & 1.17361 & 0 \\ 0 & 0 & 0 & 0 & 0 & 1.52569 \end{pmatrix}. \qquad (3.17)$$

Figures 3.17 to 3.22 show the field recorded VSP data and the synthetic seismograms for the vertical and the radial components for the three representative offset sources. The near-offset and far-offset data show that the vertical component is stronger than the radial one as expected from the ray paths as shown in the figure on page 60, while the mid-offset data has a stronger radial component than the vertical one. To analyze the particle motion and to verify the synthetic seismograms against the field data, hodogram anayses was performed. Hodograms are cross-plots between two components in multi-component data to detect the arrival directions of waves over a certain time window.

The results of the hodogram analyses in Figures 3.23 to 3.25 show that the near-offset and the far-offset data have good agreement between the field data and the synthetic seismograms. The mid-offset data has less agreement with each other. This might be explained by 1) the low signal to noise ratio due to unexpected heterogeneity along the wave propagation or 2) the existence of head waves can change the arrival direction.

3.2.5 Conclusion

The wavefront construction method is an extension of conventional ray tracing system that overcomes the lack of ray density control over propagation. The wavefront construction method adaptively controls the rays by checking the physical conditions for the ray insertions. The simple test on the isotropic and anisotropic homogeneous model showed that it has sufficiently low errors in traveltime and amplitude computation. The more complicated low velocity zone model showed that wavefront construction code successfully modeled the caustics and mapped triplications of arrivals. Synthetic seismograms has been generated using Green's tensor using wavefront construction method. The Wavefront construction simulation in the gradient model on salt dome areas in the Gulf of Mexico showed that the final synthetic seismograms has good agreement with the observed field data. The Green's tensor and its parameters can be used for the inputs of imaging problems such as prestack Kirchhoff depth migration algorithms.

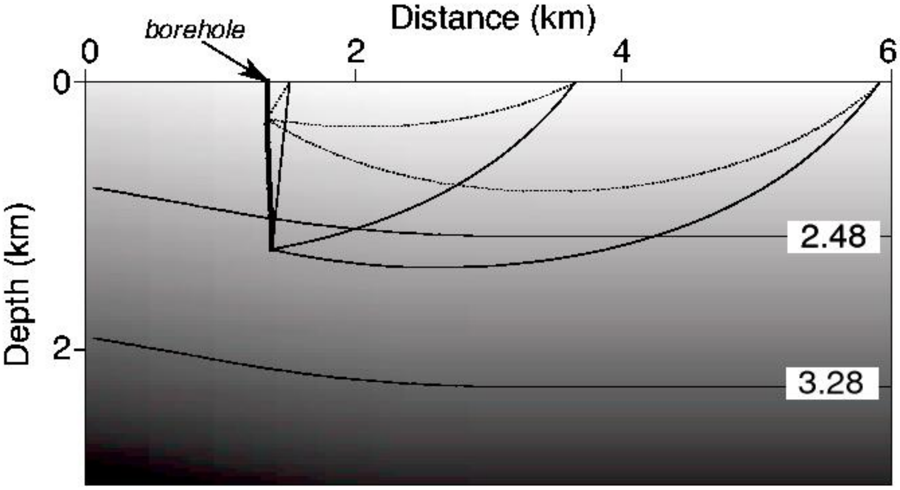

Fig. 3.16. Velocity profile and the ray paths corresponding to the near-, mid-, and far-offset sources of NW line in Figure 3.15. Rays from the mid-offset source arrive at the receiver nearly horizontal (Durussel, 2002).

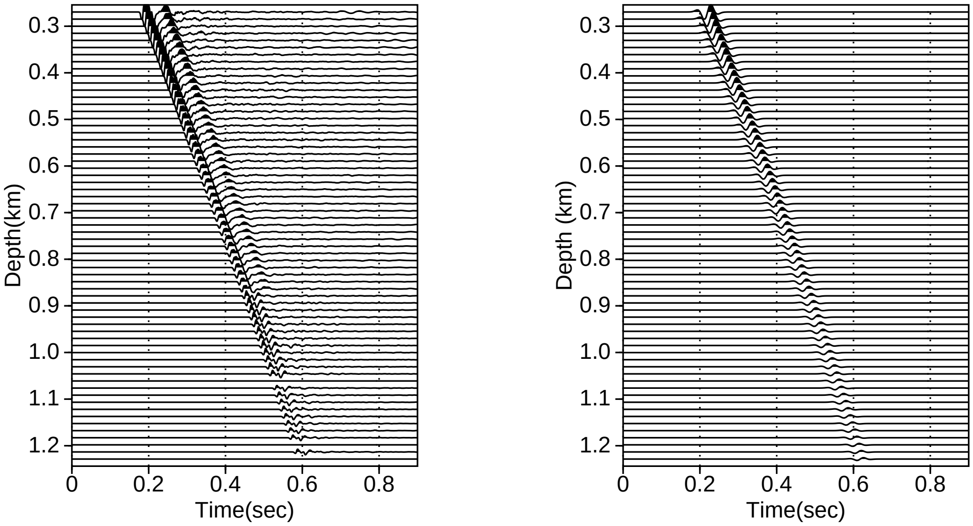

Fig. 3.17. Vertical component of the recorded and the synthetic seismograms for the near-offset source. Left: Recorded VSP data of the salt dome in the Gulf of Mexico. Right: Synthetic seismograms from the wavefront construction method.

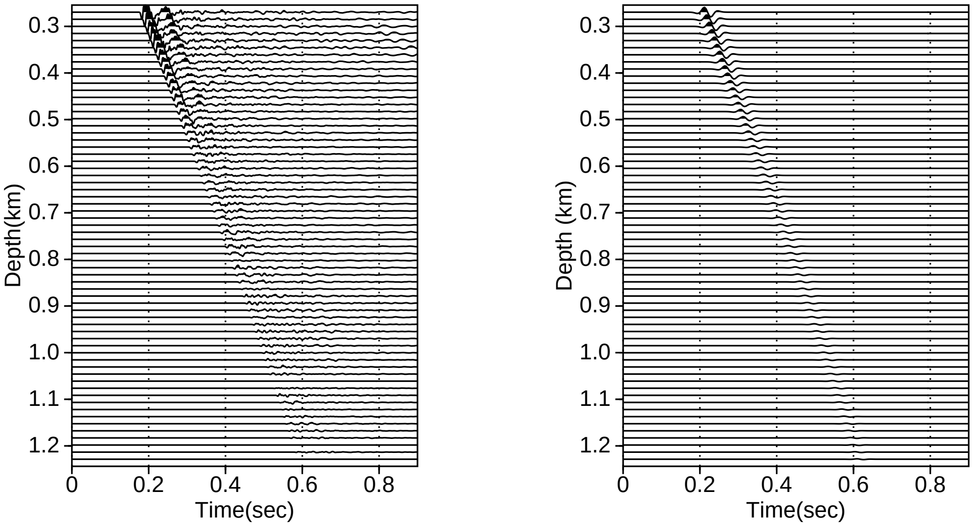

Fig. 3.18. Radial component of the recorded and the synthetic seismograms for the near-offset source. Left: Recorded VSP data of the salt dome in the Gulf of Mexico. Right: Synthetic seismograms from the wavefront construction method.

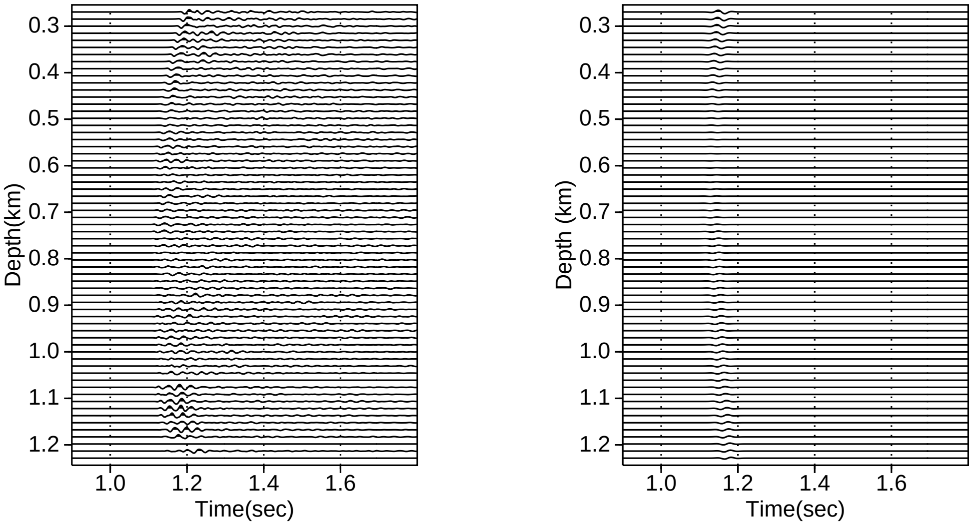

Fig. 3.19. Vertical component of the recorded and the synthetic seismograms for the mid-offset source. Left: Recorded VSP data of the salt dome in the Gulf of Mexico. Right: Synthetic seismograms from the wavefront construction method.

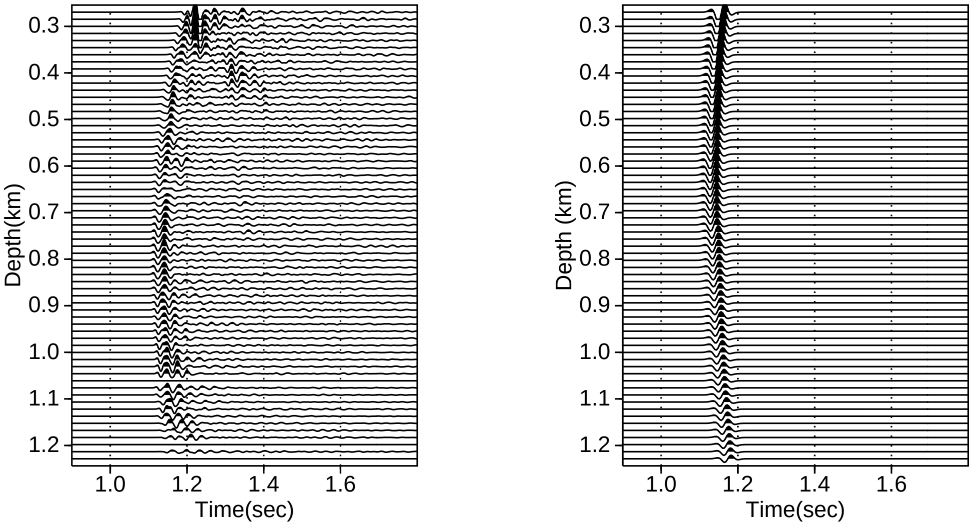

Fig. 3.20. Radial component of the recorded and the synthetic seismograms for the mid-offset source. Left: Recorded VSP data of the salt dome in the Gulf of Mexico. Right: Synthetic seismograms from the wavefront construction method.

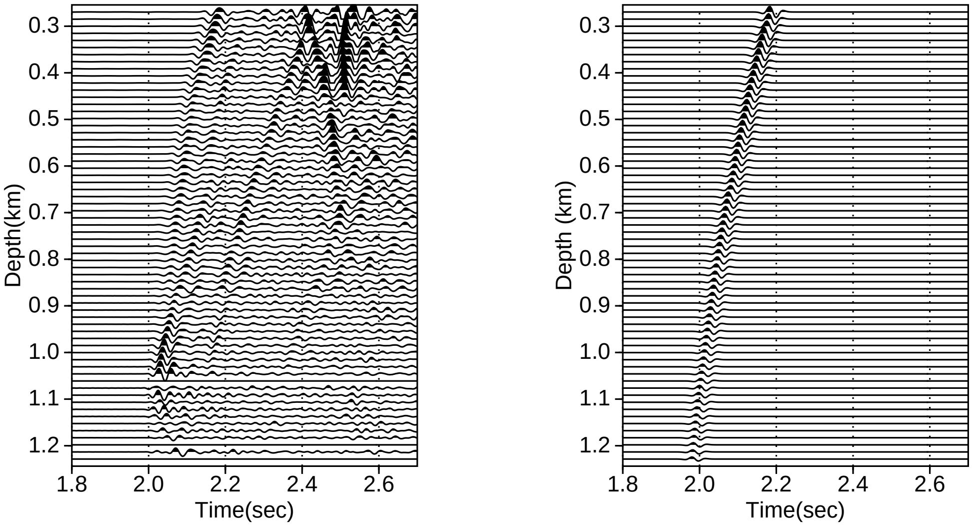

Fig. 3.21. Vertical component of the recorded and the synthetic seismograms for the far-offset source. Left: Recorded VSP data of the salt dome in the Gulf of Mexico. Right: Synthetic seismograms from the wavefront construction method.

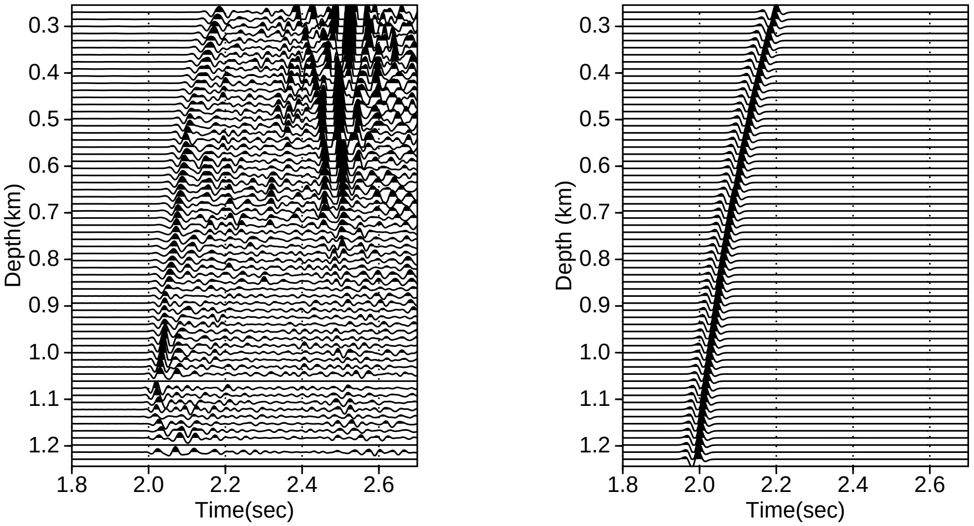

Fig. 3.22. Radial component of the recorded and the synthetic seismograms for the far-offset source. Left: Recorded VSP data of the salt dome in the Gulf of Mexico. Right: Synthetic seismograms from the wavefront construction method.

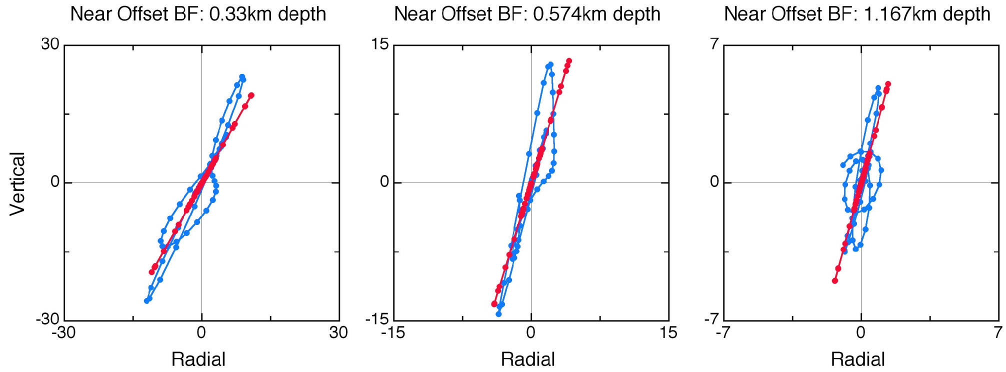

Fig. 3.23. Comparison of the hodograms of field VSP data (blue) and synthetic seismograms (red) for the near-offset source.

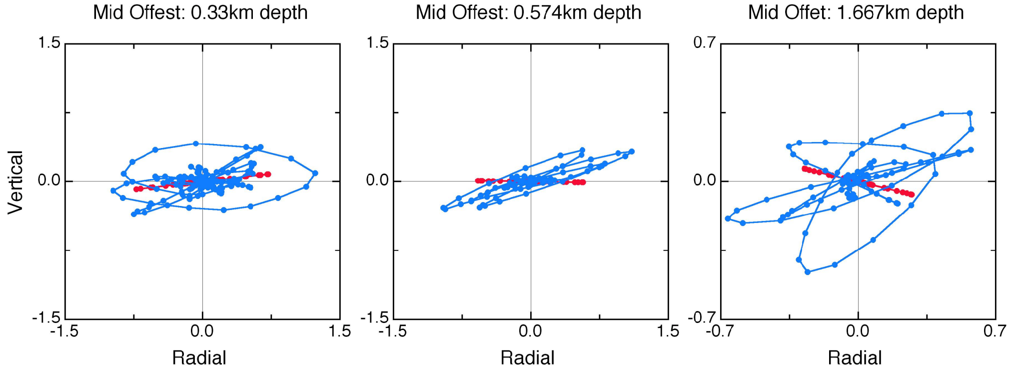

Fig. 3.24. Comparison of the hodograms of field VSP data (blue) and synthetic seismograms (red) for the mid-offset source.

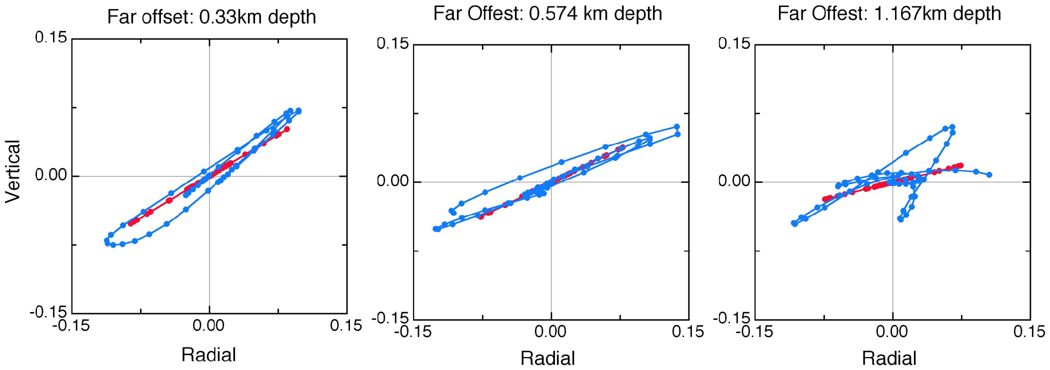

Fig. 3.25. Comparison of the hodograms of field VSP data (blue) and synthetic seismograms (red) for the far-offset source.

CHAPTER IV

TRAVELTIME ESTIMATION WITH MODEL BASED INTERPOLATION RAY TRACING METHOD FOR LAYERED MODELS - WFC APPROACH

The major outputs of forward seismic wave propagation modeling are traveltimes, amplitudes, and displacement vectors. Some methods are specialized to compute certain physical quantities from the modeling. Some popular methods include direct solution of the wave equation with finite-difference methods, solving the eikonal equation with finite-difference, and ray tracing methods.

The finite-difference method (FDM) is solving a wave equation (elastic or acoustic) with finite-difference and, thus can get a complete solution (total wavefield) of the wave equation. Sometimes the total wavefield from the finite-difference mehtod is complicated and it is difficult to interpret. Also, the finite-difference method is computationally expensive and requires huge memory size, especially in 3D simulation.

The eikonal solver with the finite-difference computation is also a popular method in computing the first arrival traveltime and it is known to be relatively robust and fast (Vidale, 1990; Van Trier and Symes, 1991; Kim, 2002). However, it experiences some difficulties with caustics and the eikonal equation fails to track the later arrivals (Geoltrain and Brac, 1993).

The authors compared migration results of the Kirchhoff type prestack migration with the first arrival traveltime and paraxial extrapolator type migration. They showed that the first arrival after caustics is dissipative and resulted in an artificial overmigration.

The needs for the handling of later arrivals led to the recent developments in the eikonal solver to compute reliable traveltimes and amplitudes of the later arrivals (Qian and Symes, 2002; Buske and Kästner, 2004).

The ray tracing method is widely used in computing traveltimes, amplitudes, and displacement vectors for a certain wave type. To avoid the problems in the conventional ray tracing method such as two-point problem and ray density control over diverged rays, the wavefront construction method has been developed (Vinje et al., 1993; Lambaré et al., 1996; Lucio et al., 1996; Ettrich and Gajewski, 1996;

Gibson, 1999; Vinje et al., 1999; Gibson et al., 2002; Mispel and Williamson, 2001; Lee and Gibson, 2003; Gibson et al., 2005). In the wavefront construction method, the geometry of the wavefront surface is tracked instead of handling individual rays. If the ray density on a wavefront at a certain point is less than the preset threshold level, new rays are inserted to keep a certain level of accuracy.

Similar to the wavefront construction method, the wavefront oriented ray tracing inserts new rays, not on the wavefront of interesting but from the source point when the ray density is less than the preset threshold at the considering wavefront (Coman and Gajewski, 2001; Kaschwich and Gajewski, 2003). The merit of the wavefront oriented ray tracing is higher accuracy due to reducing possible errors from ray insertion. Both methods are basically same idea and if the wavefronts are constructed with enough rays, the difference between two methods should be negligible.

Both wavefront type methods generally use continuous earth models. In continuous models, there are no discontinuous boundaries, i.e. the medium's physical properties are continuously changing; this restriction is commonly addressed by other methods such as the finite difference methods.

In layered models, the layer boundary is defined as where the medium's physical properties are changing rapidly. Especially in most commonly used homogeneous isotropic/anisotropic layered models, we will definitely have sudden changes in quasi-P wave and quasi-S wave velocities and densities (it could be not so rapid change for gradient layered models). The main reasons of using the gradient model for wavefront construction method are 1) the high-frequency approximation of ray tracing, and 2) the complicated book keeping problems handling the wavefront at the layer boundaries. By handling layer by layer as in conventional ray tracing, the first problem can be solved, but we still have the second problem.

The proposed Model Based Interpolation (MBI) ray tracing method borrows the idea from the wavefront construction method utilizing the functionalities of the WFC and is adapted to handle the layered models. In MBI ray tracing, the same geometry of WFC is considered by associating neighboring rays required to correctly map solutions on the free surface. Instead of propagating and intepolating the wavefronts with constant increment of traveltime, interpolation is constrained near the layer interfaces in the MBI ray tracing (Figure 4.1). If the rays reach a layer boundary, the ray density on the corresponding wavefront mesh element (ray tube) is checked by some criteria based on various physical quantities such as traveltimes, distance between rays, and area of the cross-section of the ray tube. If the test requires more rays, new rays are inserted starting from the surface of the cross-section of the ray tube with paraxial traveltime correction. In this paper, the interpolation is based on spatial constraints rather than traveltime conditions.

The MBI ray tracing has been developed and implemented on the top of the wavefront construction method as an extension. To test and verify the feasibility of this method, a simple test on isotropic/anisotropic layer model has been performed. The ray tracing results of the conventional paraxial ray tracing (Gibson et al., 1991) used for the comparison. For more complicated models, multiple horizontal/tilted layer models are tested by comparing the traveltime results of the wavefront construction method with initially dense set of rays and the MBI ray tracing. Multiple layers including a salt dome model have been also generated to test the more complicated models.

4.1 Theoretical Background and Method

Ray tracing can be performed by solving the following set of ordinary differential equations (ODEs) (Červený, 1972; Červený, 2001),

$$\begin{aligned}\frac{dx_i}{d\tau} &= a_{ijkl}p_l g_j g_k \\ \frac{dp_i}{d\tau} &= -\frac{1}{2}\frac{da_{ijkl}}{dx_i}p_n p_l g_j g_k,\end{aligned} \tag{4.1}$$

Here, x_i are spatial coordinate components, p_i are slowness vector components, τ is traveltime, a_{ijkl} are density normalized elastic moduli (stiffness tensor), $a_{ijkl} = \frac{c_{ijkl}}{\rho}$, and g_i are eigenvectors of Christoffel matrix, Γ_{ij},

$$\begin{aligned}&(\Gamma_{jk} - v^2\delta_{jk})u_k = 0, \\ &\Gamma_{jk} = a_{ijkl}p_i p_l\end{aligned} \tag{4.2}$$

where v is a phase velocity in the direction of p_i. There are three eigenvalues related to the velocity and each eigenvalue corresponds to a squared phase velocity.

The traveltime and ray trajectory along a ray path can be found by solving the right hand side of $dp_i/d\tau$ and $dx_i/d\tau$ in equation (4.1). The above set of ordinary differential equations is numerically solved with the 5th order Runge-Kutta method

(Press et al., 1992), leading the ray paths, x_i, and the traveltime, τ.

The paraxial ray method (Červený, 2001) efficiently extrapolates information from a known ray position to nearby locations, reducing the total number of rays and computations. The traveltime at a point $\mathbf{x}$ near a known reference point $\mathbf{x^c}$ on the ray path of the central ray is obtained from a Taylor Series expansion:

$$\tau(\mathbf{x}) \approx \tau(\mathbf{x^c}) + p_i(x_i - x_i^c) + \frac{\partial^2 \tau}{\partial x_i \partial x_j}(x_i - x_i^c)(x_j - x_j^c), \tag{4.3}$$

where p_i are slowness vector components and x_i are the Cartesian coordinate components.

The paraxial traveltime estimation is used for setting up a new ray at the interpolation considering the curvature of the wavefront of the ray tube (Figure 4.1). To compute the ray derivatives in (4.3), we implemented the central finite-difference method when the corresponding neighbor rays are available.

The model based interpolation ray tracing method is implemented in three steps utilizing the related functionality of the wavefront construction method.

1. Initial ray tracing with given initial mesh geometry. This initial ray tracing is performed considering reflection or transmission at the layer boundary. The conventional take-off angle mesh or a different initial mesh generation scheme, such as a cubed sphere mesh (Lee and Gibson, 2003), can be used to set up the initial mesh geometry.

2. Loop over region/layer boundaries for each ray tube and checking the ray density on the ray tube wavefront at or near the layer boundary. The condition is checked by setting up a wavefront in the ray tube before where the rays are arriving at the boundary. The wavefront is constructed by finding a traveltime slightly earlier than the minimum traveltime in the ray tube before hitting the boundary.

3. If a new ray is required to satisfy the preset ray density criterion, trace a new ray from a cross section or the wavefront of the ray tube with paraxial correction in traveltime considering curvature.

A schematic example of the model based interpolation ray tracing for a salt dome model is shown in Figure 4.2. For each ray tube, a wavefront is constructed when the

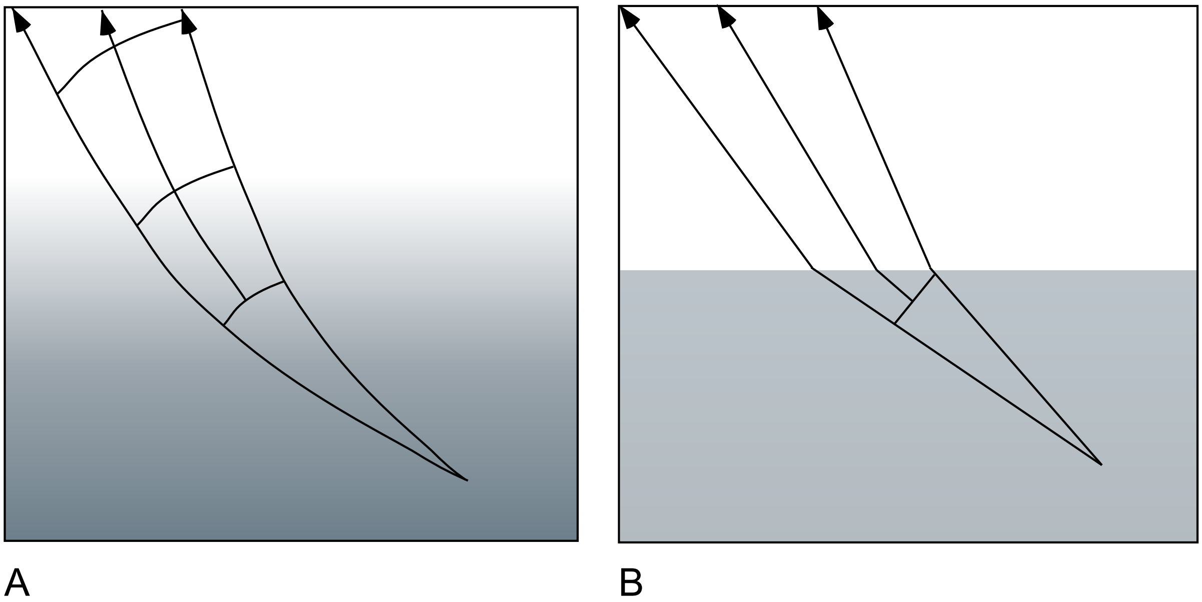

Fig. 4.1. A schematic figure illustrating the basic ideas of wavefront construction method applied on a smoothed gradient velocity model(A) and the model based interpolation (MBI) ray tracing method applied on a layered model (B).

ray tube hits the layer boundary. If necessary, a new ray is inserted at the wavefront after checking the ray density condition. Figure 4.3 shows an example of interpolated rays in MBI ray tracing where the rays are diverged near the layer boundary. When the interpolated rays still can't satisfy the ray density criterion, the ray interpolation can be performed recursively (Figure 4.4) till it satisfeis the preset condition. The overall computing time slows down when the recursive refining is activated due to rigorous checking of the ray density condition in every recursive step. The analysis of the refining will not be covered in this paper because it is not efficient in terms of computing resources.

One of the parameters to be determined in the model based interpolation ray tracing method is deciding the wavefront in a ray tube. The wavefront is decided by taking a certain traveltime along the ray before arriving at the model boundary. By taking at least the minimum traveltime of four rays in a ray tube can make a wavefront. To build a stable wavefront for the ray tube, it is safer to take a traveltime which is slightly earlier than the minimum traveltime.

$$\tau = \tau_{min} + \Delta\tau$$

This is due to the finite-difference implementation in computing ray derivatives. To compute ray derivatives in the MBI ray tracing, the central finite-difference scheme has been implemented requiring four neighboring rays (Figure 4.5). Finding the minimum traveltime in a ray tube before arriving at the boundary can gurantee the condition for the simple single sided forward finite-difference method. However, for the same traveltime, the position on a ray path for other rays required for the central-finite difference can be located in other regions (Figure 4.6). This could happen for more obliquely arriving (the larger incident angles) ray tubes than vertically arriving (the smaller incident angles) ones. The correction time $\Delta\tau$ for the rays with the larger incident angles in Figure 4.6 is larger than the ray tube with the smaller incident angles. For the incident ray tubes with the larger incident angles, we may not have both ray tubes in the same region. Considering the above situation, first, the MBI algorithm is searching the minimum $\Delta\tau$ for the central finite-difference by adapting its values in the region. If the MBI algorithm can't find $\Delta\tau$ satisfying central finite-difference condition, then it automatically switches to the single sided forward finite-difference method.

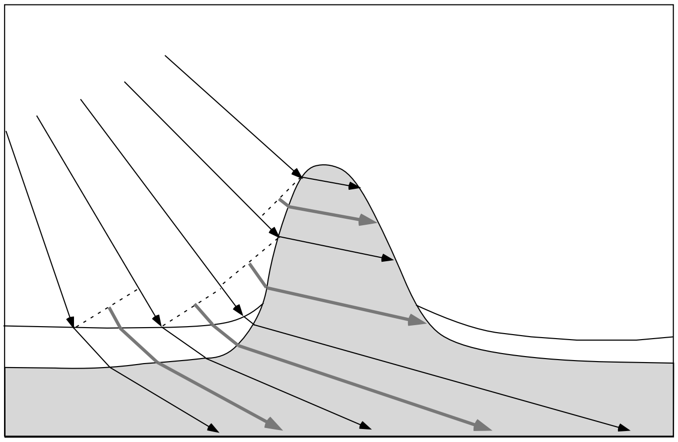

Fig. 4.2. A schematic figure showing possible implementation for a salt dome model.

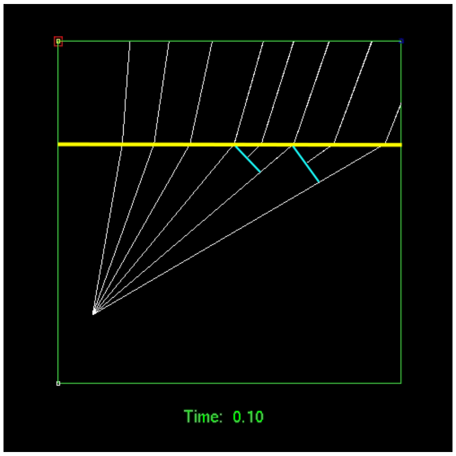

Fig. 4.3. The model based interpolation ray tracing showing inserted rays at the wavefront on some ray tubes in order to satisfy the ray density criterion.

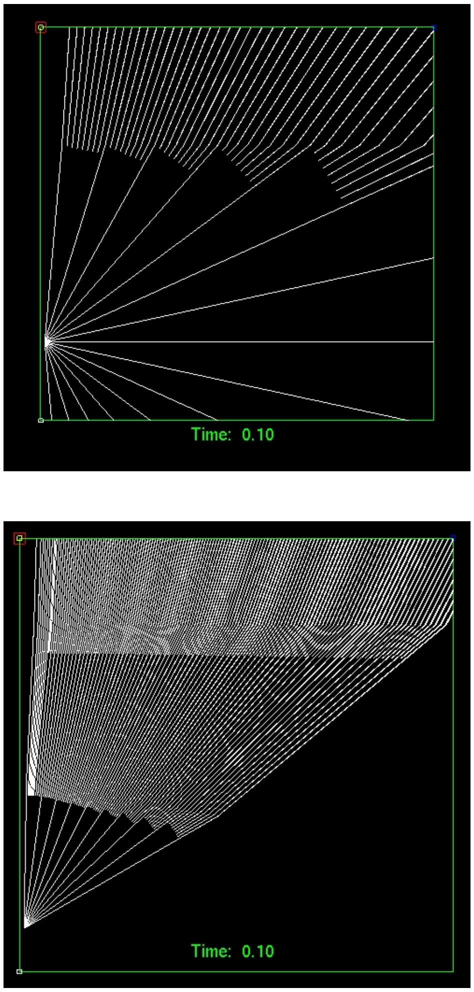

Fig. 4.4. Examples of the MBI refining on the boundaries. Top: two layers model with cubed sphere mesh coordinates. Bottom: three layers model with take-off angle mesh coordinates.

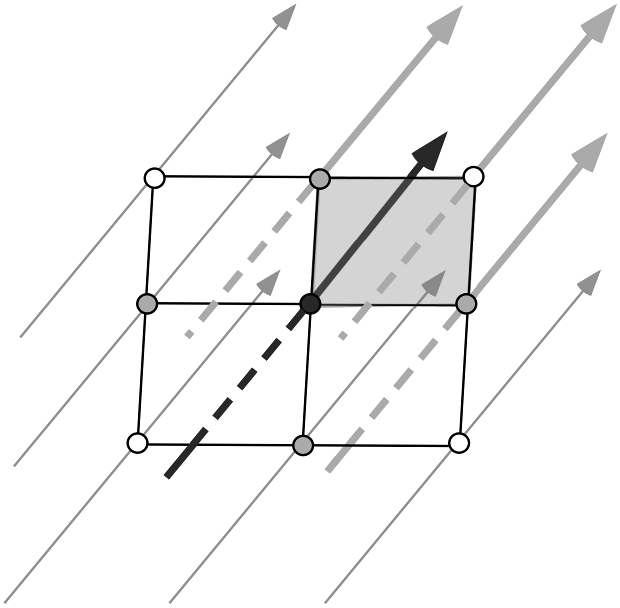

Fig. 4.5. Ray nodes on a wavefront for the central finite-difference computation. For the central finite-difference computation, the current ray tube (gray cell) and one more ray tube in the lower-left side is required. If the neighboring rays are not available, the single forward finite-difference is used to compute ray derivatives.

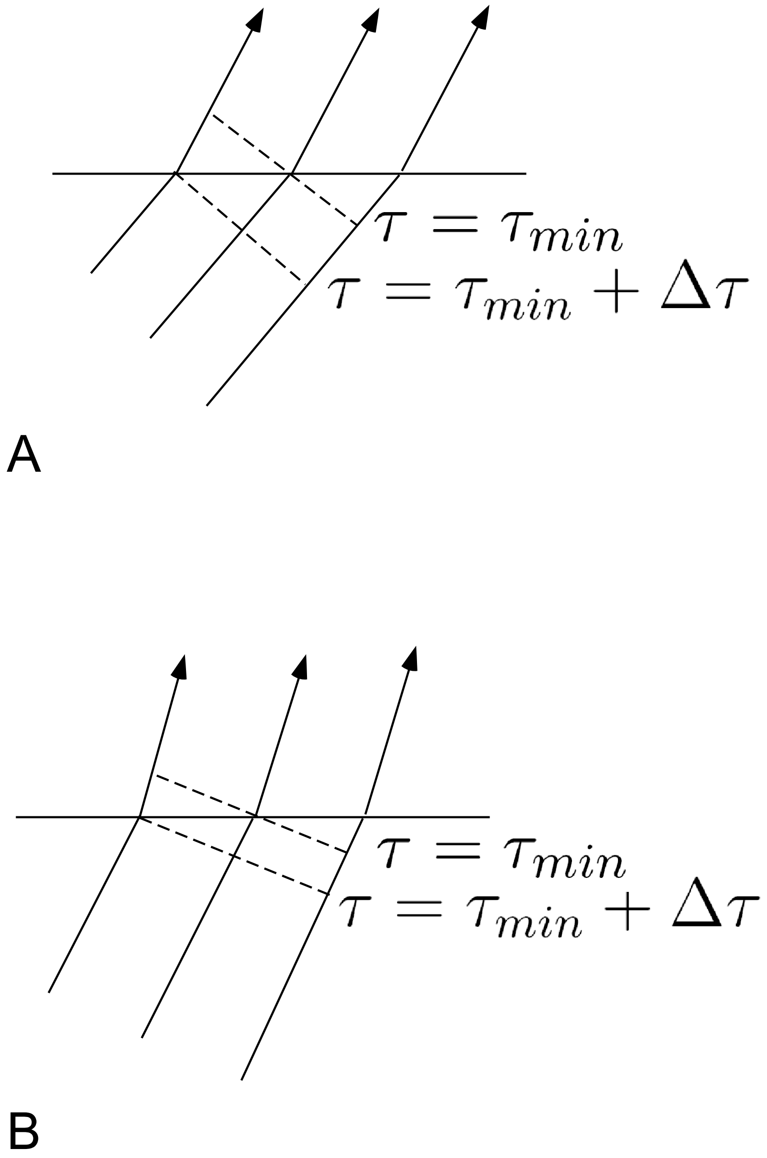

Fig. 4.6. Selection of a wavefront time for a ray tube. The wavefront time is selected earlier than the minimum traveltime of four rays in a ray tube before arriving at the boundary. Depending on the arrival angle the compensation time $\Delta\tau$ can be different. A ray tube with the larger incident angle (A) has larger correction time than the rays with the smaller incident angle (B) to compute the central finite-difference.

4.1.1 Reflections and Transmissions at the Interface of General Anisotropic Media

The reflections and transmissions from an incident wave at the interface for isotropic media are easily determined by Snell's law (4.4). For isotropic media, the slowness surface is spherical and the velocity in an arbitrary direction is fixed; by setting velocities for each wave type and incident angle, the transmission or reflection angle is easily computed. Snell's law is

$$\frac{sin\theta_i}{\alpha_1} = \frac{sin\theta_r}{\alpha_1} = \frac{sin\psi_r}{\beta_1} = \frac{sin\theta_t}{\alpha_2} = \frac{sin\psi_t}{\beta_2}, \tag{4.4}$$

where θ is the angle associated with the compressional wave and ψ is the angles assocaited with shear waves. The subscripts in the angles represent incident (i), reflection (r), and transmission (t) of the corresponding wave type and α and β are compressional and shear wave velocities. For general anisotropic media, the slowness surface is not spherical and the velocity is changing as a function of the angle. We have one more unknown in the above equation and Snell's law can't be used to directly determine reflection/transmission waves in anisotropic cases. This problem has been studied by many researchers (Fedorov, 1968; Henneke II, 1972; Rokhlin et al., 1986; Rathore et al., 2003; Gajewski and Pšenčik, 1987). The general physical condition for the solid/solid boundary is a continuation of all stress and displacement vectors. Figure 4.7 shows the slowness vector surface in 2D. The horizontal vector, $\vec{b}$, on the interface shared by all incident, reflected, and transmitted waves is satisfying the continuation condition. The general expression for the reflected and transmitted vectors (Figure 4.7) with the normal vector can be simply expressed as

$$\mathbf{m}_j^{\eta} = \mathbf{b} + \xi\hat{\mathbf{n}}, \tag{4.5}$$

where $\hat{\mathbf{n}}$ is the unit normal vector to the interface, η indicates reflection or transmission, and j indicates the wave type (quasi-shear or quasi-compressional). The vectors $\mathbf{b}$ and $\hat{\mathbf{n}}$ are known while the parameter ξ, the projection of the slowness vectors on the normal to the interface, needs to be determined. Inserting (4.5) into the Christoffel equation (4.2) with the corresponding elastic moduli leads to the 6th order polynomial in ξ (Fedorov, 1968; Gajewski and Pšenčik, 1987). The 6th order polynomial can be solved with widely used numerical tools (Press et al., 1992).

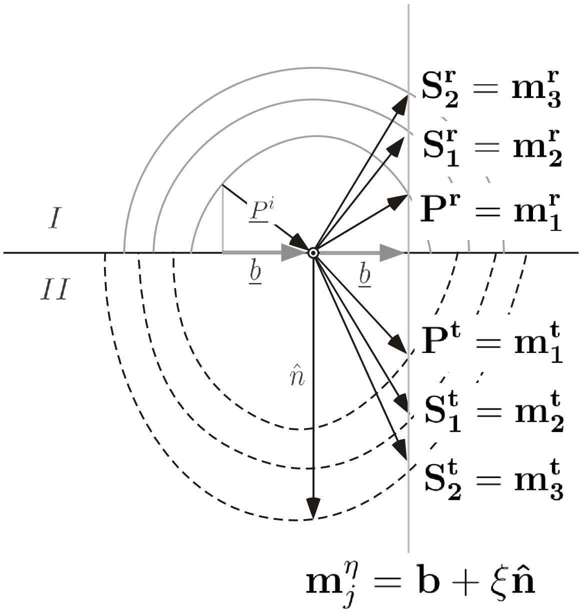

Fig. 4.7. Determination of the reflection and transmission at the interface of two anisotropic media based on the slowness surface. The incident wave is quasi-P wave and three possible types of reflection/transmission waves are illustrated.

4.1.2 Smoothed and Layered Models

Due to the high frequency approximation of the ray tracing system, many ray tracing methods and the wavefront construction codes use gradient or smoothed velocity models. A common way of smoothing a velocity model starts from a layered or blocky velocity model constructed by recursive velocity analysis procedures (including tomography and migration) and using some kinds of smoothing functions. The degree of smoothness for valid modeling is an open question. However, it is easy to show how the simple smoothing can change the traveltime computation results from the original layered model. One simple example is taking a two isotropic layer model which is a Heaviside step velocity function and smoothly approximated one (4.6) at the boundary (Figure 4.8). The Heaviside step function is

$$v_1 + \Delta v \left[\frac{1}{1 + e^{-\frac{z - z_c}{h}}} \right] \tag{4.6}$$

where h determines the degree of smoothness and it becomes a step function when $h \to 0$. $v_{p1} = 3.0 km/s$, $\rho_1 = 2.6 \ g/cc$, $v_{p2} = 3.5 \ km/s$, and $\rho_2 = 2.7 \ g/cc$. The wavefront construction method for compressional wave modeling has been performed for the gradient model and a conventional ray tracing method has been applied to the layered model (Figure 4.9).

The mapped traveltime results are compared to each other by subtracting the results of the wavefront construction method from the results of the conventional ray tracing (Figure 4.10). Even though the ray paths in Figure 4.9 look similar, the results show that the maximum difference is over 5ms, which is significant. This simple experiment implies that if the process of model building does not meet the gradient velocity assumption, simple smoothing from the blocky velocity model can change the traveltime results significantly. Therefore, if the velocity model has been estimated with a homogeneous layered model assumption (which is more popular), simple smoothing can be dangerous by estimating incorrect traveltimes for imaging. The model based interpolation method is designed to take the widely used layered velocity model as well as improving on the weak point of the conventional ray tracing system on ray density control over diverging rays.

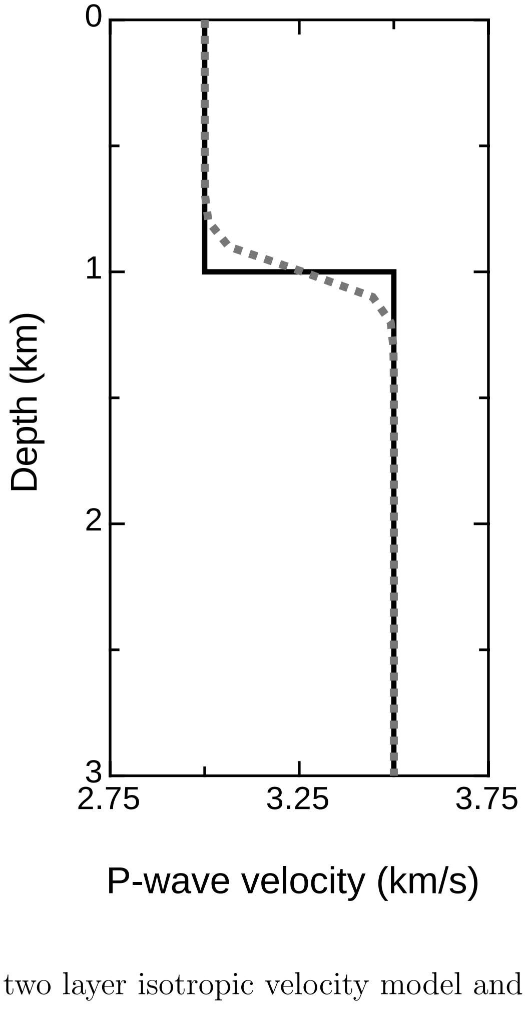

Fig. 4.8. Simple two layer isotropic velocity model and smoothed model.

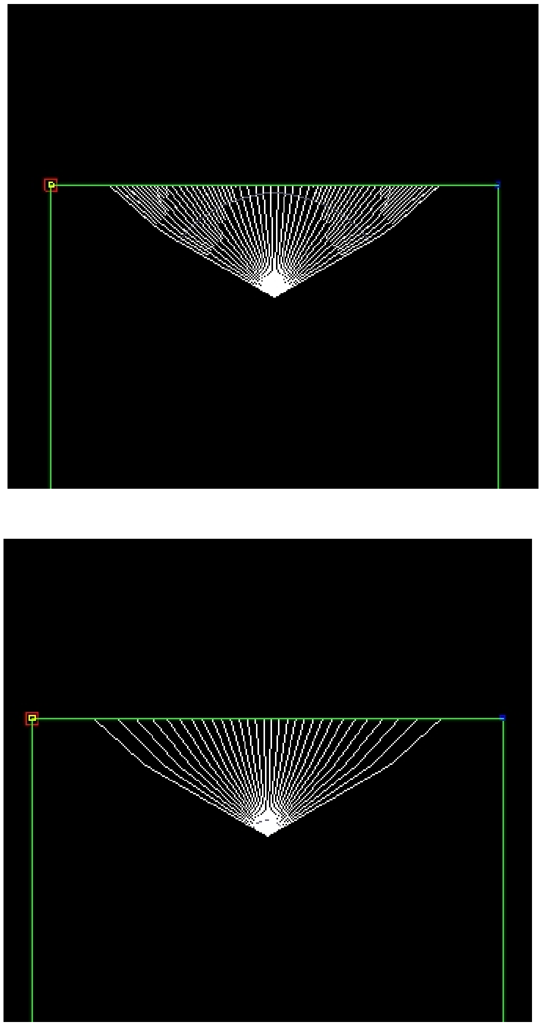

Fig. 4.9. Modeling results of Figure 4.8. Top: wavefront construction results with a smoothed velocity model. Bottom: conventional ray tracing with a two layer model.

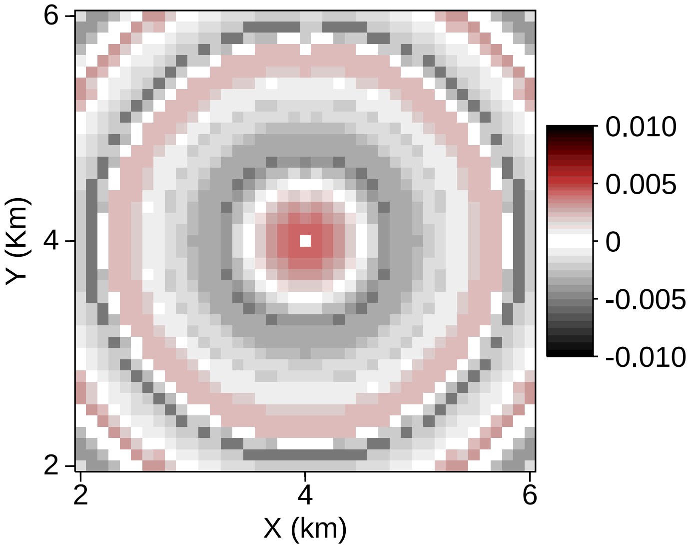

Fig. 4.10. Traveltime difference between the wavefront construction method with a smoothed model and the MBI ray tracing method with a layered model.

Table 4.1. Velocities and densities of the isotropic 2 layer model.

Layers	Vp (km/s)	Vs (km/s)	ρ (g/cc)
Upper Layer	3.0	1.5	2.6
Lower Layer	3.5	1.75	2.7

4.2 Traveltime Error Analyses for Isotropic and Anisotropic Media

Validations of the MBI ray tracing method was performed with two layer models for isotropic and anisotropic media. The MBI traveltimes were compared with the conventional paraxial ray tracing (Gibson et al., 1991) results for validation purposes. The conventional ray tracing was initally traced with four times denser than MBI tracing to make sure they are comparable in terms of the final ray density at the surface receiver stations. Figure 4.11 shows the ray paths of conventional ray tracing and MBI ray tracing interpolated near the boundary of the 2 layer model. The basic model is composed of two layers with a boundary at 1km depth. A plane of receiver array is located on the surface from x=3 km, y=3 km to x=7 km, y=7 km with 0.1km interval spacing (Figure 4.12).

4.2.1 Isotropic Layers

The first experiment was performed with two isotropic layers. The velocities and densities are described in Table 4.1. Rays in the conventional method are traced with declinational angle interval of 1.5° ($\Delta\psi = 1.5°$) and azimuthal interval of 3.0° ($\Delta\theta = 3.0°$). The initial rays in MBI tracing were traced with declinational angle interval of 3.0° ($\Delta\psi = 3.0°$) and azimuthal interval of 6.0° ($\Delta\theta = 6.0°$).

Figure 4.13 shows that the traveltime difference between the legacy code and the MBI ray tracing, and between the legacy code and the conventional ray tracing with the dense initial ray. Both differences are almost in the same range as shown in Figure 4.14 and the difference between two methods is less than $\approx 2 \times 10^{-5}$(Figure 4.15). It is interesting to compare the computation time for this simple experiment. The computation time for conventional ray tracing and MBI ray tracing has been

Table 4.2. Computation time comparison for the conventional and the MBI ray tracing methods for the isotropic 2 layer model.

	Conventional	MBI
CPU time (sec)	4.92	3.64

measured on a Linux box with AMD 2.4 GHz CPU. The average computation time for conventional ray tracing took $\approx$ 4.92 seconds while MBI ray tracing took $\approx$ 3.64 seconds (Table 4.2). The traveltime results show that the outputs are in a similar ranges (the MBI ray tracing generated slightly better results) and the MBI ray tracint took less computation costs ($\approx$ 26% less).

4.2.2 Anisotropic HTI Layers

To test the MBI ray tracing algorithm for the anisotropic media, horizontal transverse isotropic (HTI) media with a horizontal axis of symmetry in x-y plane were selected. The same model and receiver geometry used in isotropic media experiment was used to compare the results for both cases. The ray paths for the isotropic and anisotropic media are projected on the surface and shown in Figure 4.16. Figure 4.17 shows the differences in ray paths as the composite effects of elastic moduli in whole layers. It is easy to see that the HTI media has an elliptical ray arrival pattern on the surface. The mapped traveltime on the surface can be used to test if the ray tracing and new ray insertion are working effectively for the anisotropic media. The 6x6 density normalized elastic moduli used in this experiment are given as

$$C^1_{mn} = \begin{pmatrix} 10.0296 & 5.0148 & 5.0148 & 0 & 0 & 0 \\ 5.0148 & 12.9506 & 5.9885 & 0 & 0 & 0 \\ 5.0148 & 5.9885 & 12.9506 & 0 & 0 & 0 \\ 0 & 0 & 0 & 3.4811 & 0 & 0 \\ 0 & 0 & 0 & 0 & 3.1282 & 0 \\ 0 & 0 & 0 & 0 & 0 & 3.1282 \end{pmatrix}$$

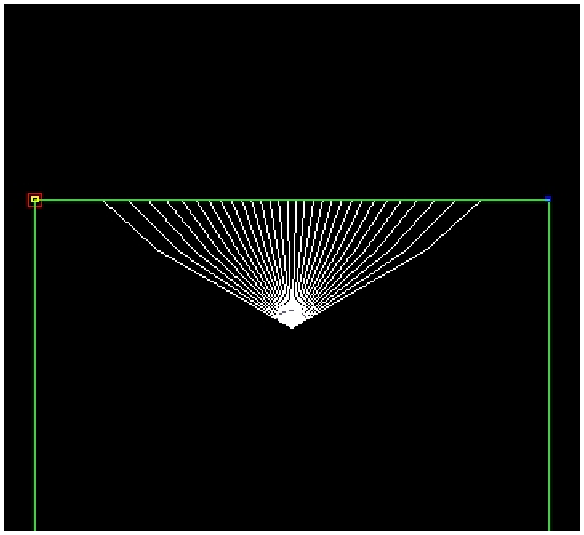

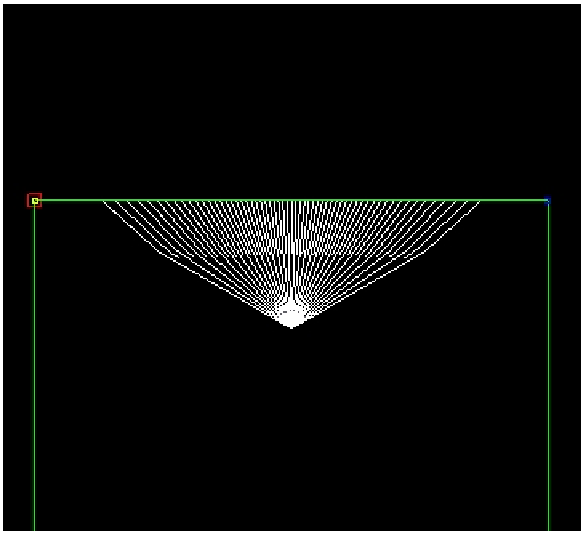

Fig. 4.11. Ray tracing showing the conventional method (top) and MBI method (bottom). Initial ray density of the MBI is half of the conventional method (the same ray density is set for both in this figure just for illustration purposes).

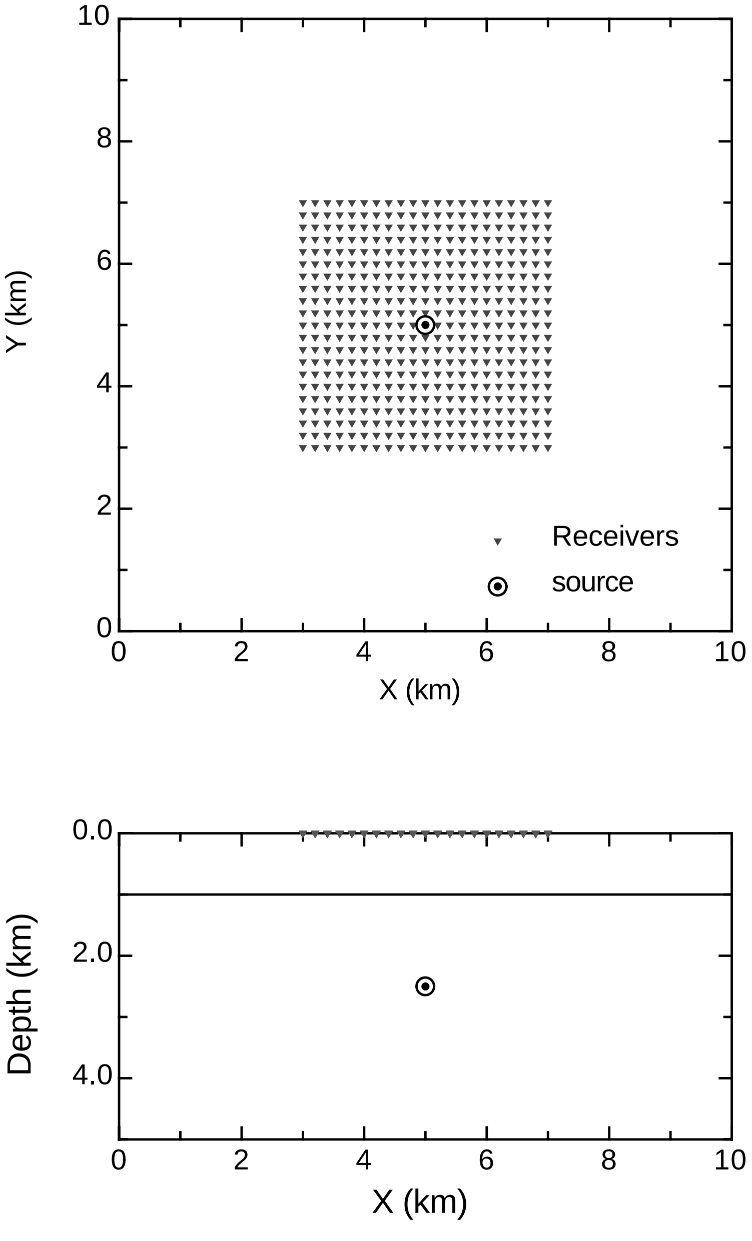

Fig. 4.12. The model and receiver geometry of the traveltime error analyses. The source is located at x=5km, y=5km, z=2.5km and the boundary is at 1km depth.

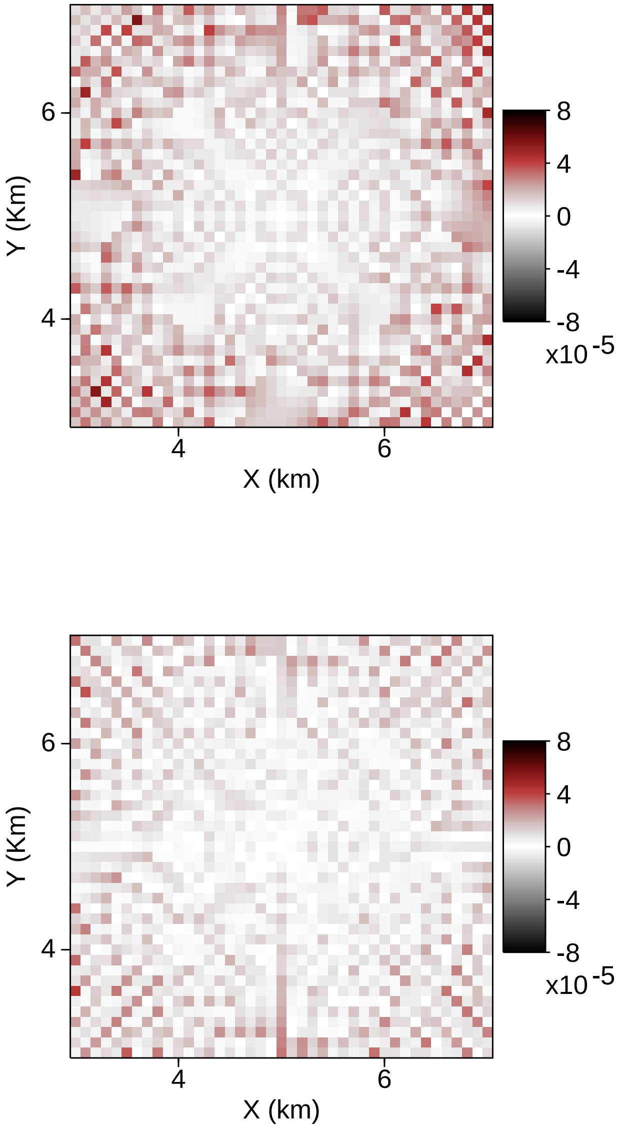

Fig. 4.13. Distribution of the traveltime difference from the results of the legacy code in the isotropic model. Top: difference between the results of legacy and ray tracing without the MBI. Bottom: difference between the results of the legacy and the MBI. The ray density without the MBI is four times higher than ray tracing with the MBI.

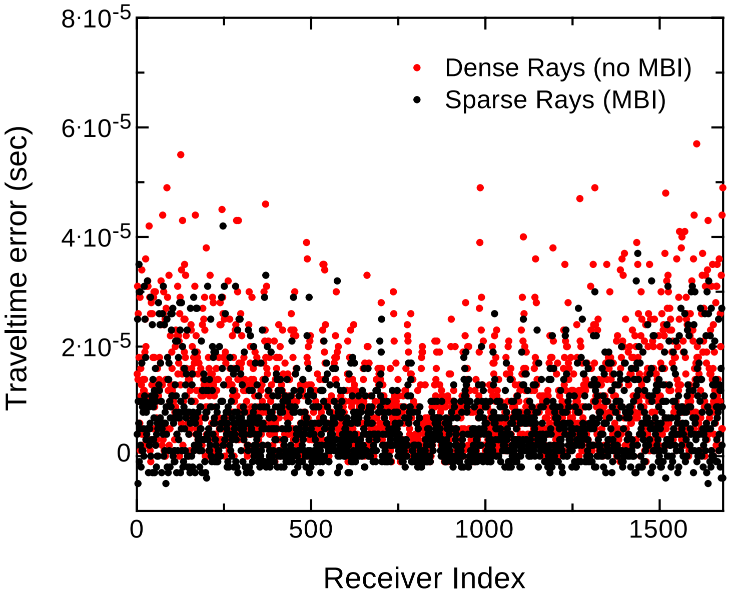

Fig. 4.14. Distribution of the traveltime difference from the results of the legacy code in istropic layer model. Both the MBI and the conventional type ray tracing has similar difference range.

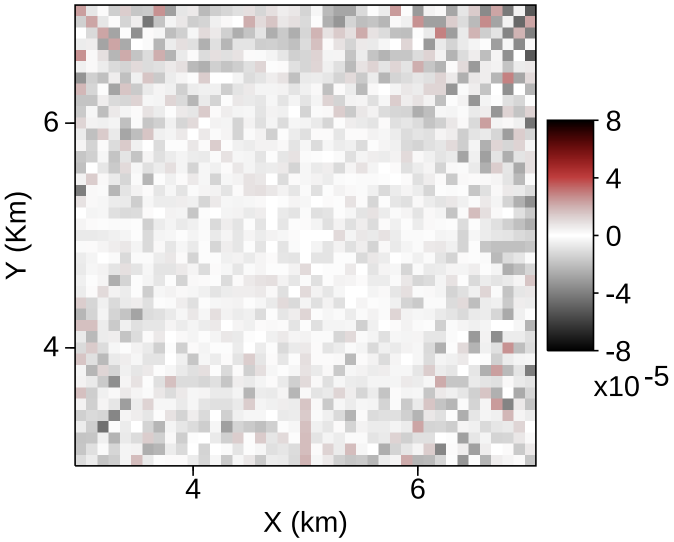

Fig. 4.15. Distribution of the traveltime difference of the MBI and the conventional ray tracing results on the receiver surface (istropic layer model). Differences are a little higher for the edges of the receiver array.

Table 4.3. Computation time comparison for conventional and MBI ray tracing methods for isotropic 2 layer model.

	Conventional	MBI
CPU time (sec)	3.092	2.391

and

$$C^2_{mn} = \begin{pmatrix} 15.9932 & 6.3173 & 6.3173 & 0 & 0 & 0 \\ 6.3173 & 15.9989 & 6.3189 & 0 & 0 & 0 \\ 6.3173 & 6.3189 & 15.9989 & 0 & 0 & 0 \\ 0 & 0 & 0 & 4.8400 & 0 & 0 \\ 0 & 0 & 0 & 0 & 4.3299 & 0 \\ 0 & 0 & 0 & 0 & 0 & 4.3299 \end{pmatrix},$$

where C^1_{mn} is the elastic moduli in the upper region, and C^2_{mn} is the elastic moduli in the lower region.

The initial ray density condition is kept the same in the isotropic layer experiment. The conventional type ray tracing without MBI is four times denser than the MBI ray tracing. The computation time for this model was measured (Table 4.3) and the CPU time for MBI took $\approx 22.67\%$ less than the conventional type ray tracing.

The traveltime results of conventioal ray tracing and MBI ray tracing were compared with the results of legacy code and the differences are shown in Figure 4.17 and Figure 4.18. The difference in distribution between the traveltime outputs from conventional ray tracing and MBI ray tracing was plotted on the the receivers (Figure 4.19). The differences of two results are in a similar range, though the MBI generated slightly better results.

4.3 Multi-layer and Salt Dome Models

Testing the MBI ray tracing method on more realistic models is an interesting challenge. For this test, simple three layer models and a salt dome model have been

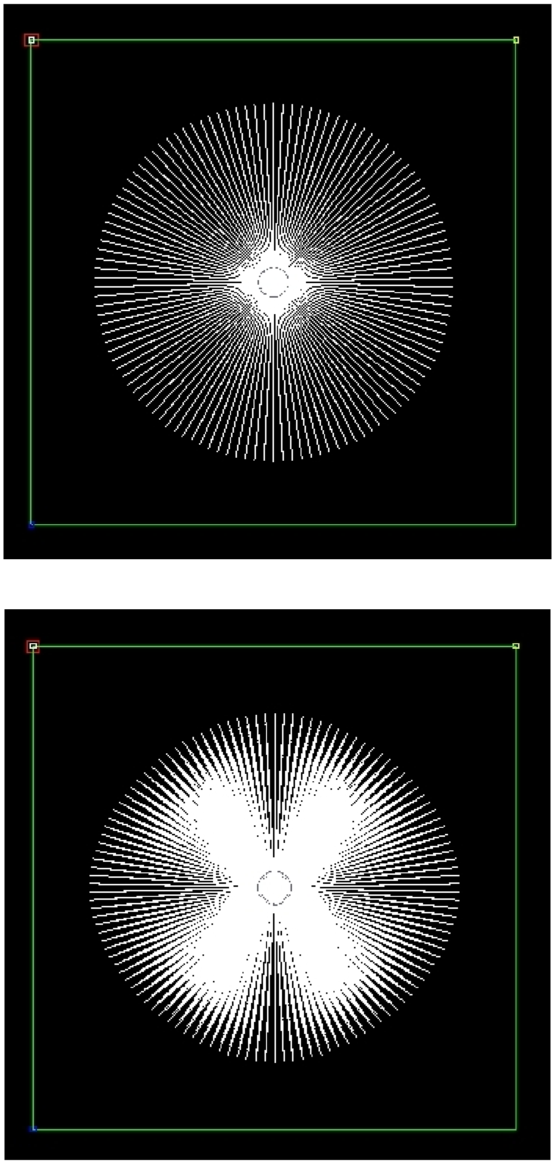

Fig. 4.16. The ray paths viewed from the surface. The ray paths in the isotropic media are perfectly circular (top) but the HTI media has an elliptical pattern (bottom).

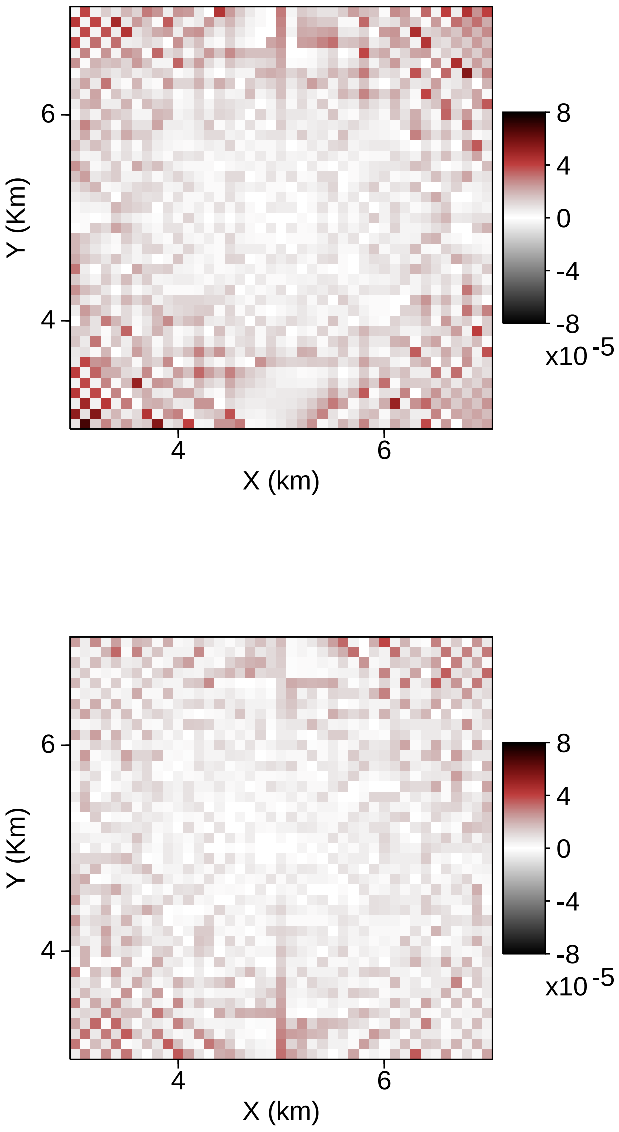

Fig. 4.17. Distribution of the traveltime difference from the results of the legacy code and the MBI in the HTI model. Top: difference between the results of legacy and ray tracing without the MBI. Bottom: difference between the results of the legacy and the MBI. The ray density without the MBI is four times higher than the ray tracing with the MBI.

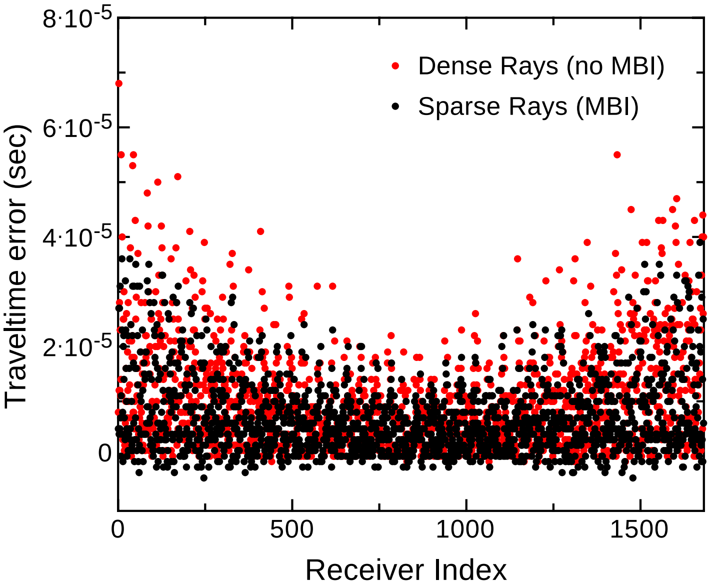

Fig. 4.18. Distribution of the traveltime difference from the results of the legacy code and the MBI in the HTI model. The differences from the two methods are in similar range.

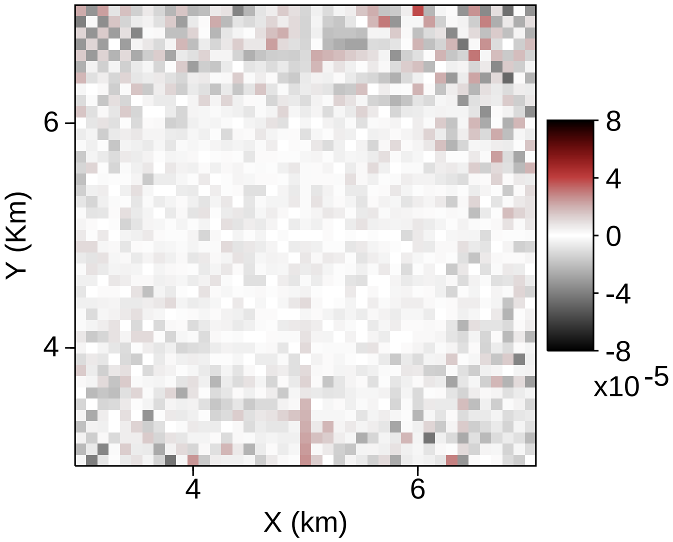

Fig. 4.19. Distribution of the traveltime differences between the results of ray tracing without the MBI and with the MBI (HTI model).

prepared for the experiment.

4.3.1 3 Layer Model

The isotropic three region models include one horizontal shallow boundary, and one with deeper horizontal boundary, dipping in left (up dip) and dipping in right (down dip) layer bounary. The test was performed by comparing the traveltime results of the conventional ray tracing without interpolation near the layer boundaries (no MBI) and the MBI ray tracing. The initial ray density in the conventional ray tracing is very high to ensure that we have a good estimation of traveltimes. The geometries and shot/receiver positions are shown in Figure 4.20. The velocities and densities of each layer are listed in Table 4.4.

Table 4.4. Velocities and densities of the 3 region models.

Regions	Vp (km/s)	ρ (g/cc)
region 1	1.5	1.0
region 2	3.0	2.5
region 3	3.5	2.6

The dipping angle is 11.31° for the two dipping models. A line array of receivers are located on the surface from 0.1 km to 9.9 km with 0.1 km increment. Figures 4.21 and 4.22 show the ray paths for the source positions of top and bottom of the model space. The traveltimes on the line array are displayed in Figure 4.23 for the three models. To check the errors of the MBI method, the traveltime results of a massive, very dense ray tracing without interpolation were compared. The initial angle increment of the dense ray tracing without interpolation is $< 1°$ and the MBI method has $\approx 4.5°$ angle increments in the cubed sphere mesh coordintaes.

The difference between the traveltime results of the massive initial dense rays and the MBI were computed (Figure 4.23) and showed the average error level of less than 5.0×10^{-5} seconds. This difference is simialr with the results in the isotropic

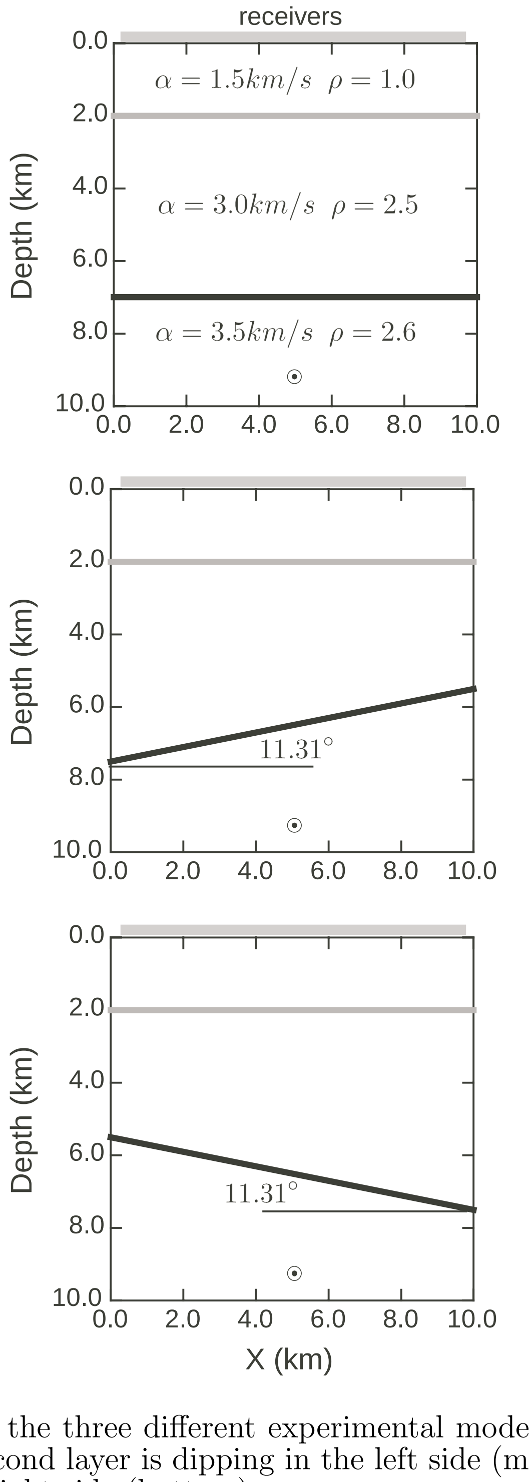

Fig. 4.20. Geometry of the three different experimental models: the second layer is horizontal (top), the second layer is dipping in the left side (middle), and the second layer is dipping in the right side (bottom).

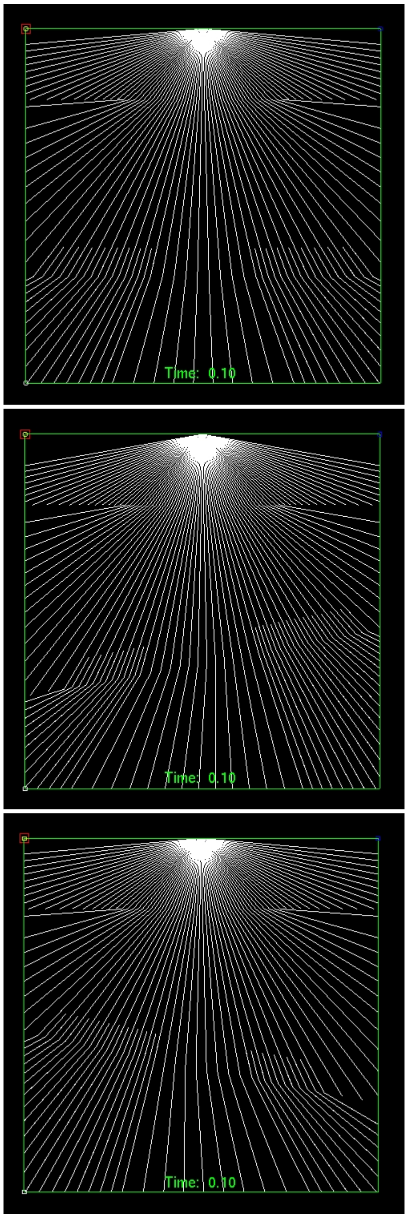

Fig. 4.21. Examples of the MBI ray tracing for the three layer models. The ray paths showing the three different models with the source location at 1 km depth.

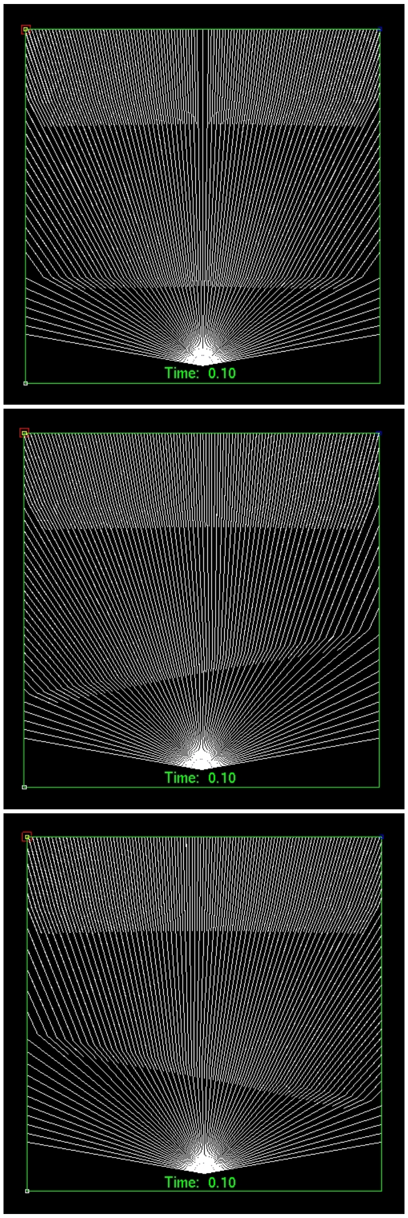

Fig. 4.22. Examples of the MBI ray tracing for the three layer models. The ray paths showing the three different models with the source location at 9.5 km depth.

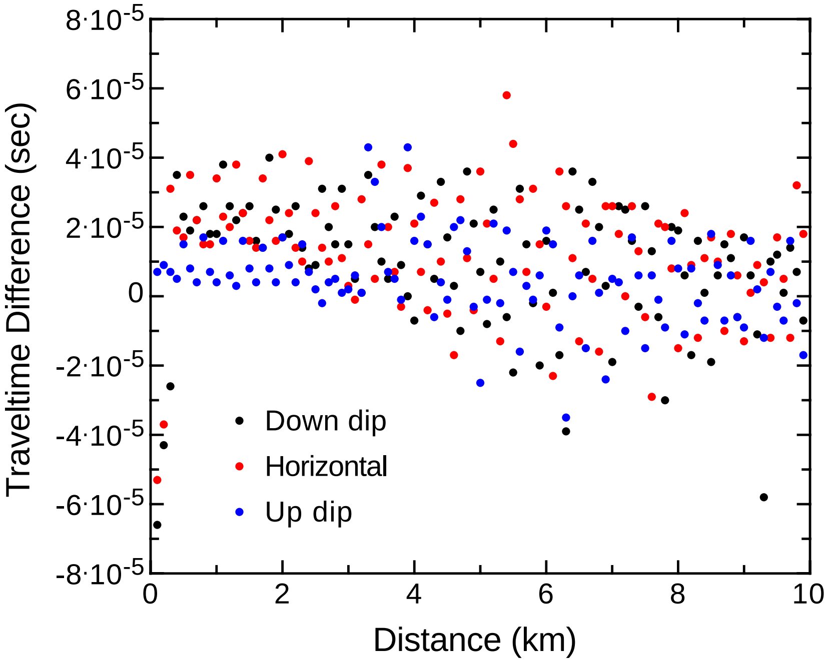

Fig. 4.23. Traveltimes are estimated along the line array of the receivers on the surface for the three models (top). The differences between the modeling results of the initially massive dense rays and the MBI are computed (bottom). The average difference is less than 5.0×10^{-5}.

and HTI media models and confirms that MBI can be used for the modeling with fewer initial rays.

4.3.2 Salt Dome Model

A more interesting salt model, composed of three layers and one salt dome built with a Gaussian function, was constructed. This model is a 2.5D model which is 2D in one direction and it has been extended to the other direction. The model and source/receiver geometry is illustrated in Figure 4.24. The velocities and densities for each layer are listed in Table 4.5.

Table 4.5. Velocities and densities of the salt model.

Regions	Vp (km/s)	ρ (g/cc)
region 1	2.55	2.2
region2: VTI shale	4.4	2.5
region 3	3.1	2.4
region 4: salt	4.5	2.1

The second layer is a simulated vertical transverse isotropic (VTI) shale, representing Green River shale, which has the following 6 by 6 elastic moduli:

$$C_{mn} = \begin{pmatrix} 20.365 & 6.49812 & 7.08713 & 0 & 0 & 0 \\ 6.49812 & 20.365 & 7.08713 & 0 & 0 & 0 \\ 7.08713 & 7.08713 & 19.3952 & 0 & 0 & 0 \\ 0 & 0 & 0 & 6.66676 & 0 & 0 \\ 0 & 0 & 0 & 0 & 6.66676 & 0 \\ 0 & 0 & 0 & 0 & 0 & 6.93343 \end{pmatrix}. \qquad (4.7)$$

These elastic moduli corresponds to the following Thomsen's parameters representing weak anisotropy (Thomsen, 1986): $\epsilon = 0.025$, $\delta = 0.055$, and $\gamma = 0.030$.

Three different types of computation were performed. The first one was conventional ray tracing with initially dense rays and without MBI. The second computation was MBI only for the salt boundary and no interpolation at the other boundaries. The last one was MBI at all boundaries. The ray paths for these three types of configurations are shown in Figure 4.25. The initial condition of the conventional ray tracing is an angle increment of $< 1^\circ$ and and the MBI ray tracing has angle increments of $\approx 3^\circ$. For this experiment, only a limited angle range in y direction (extended direction in the 2.5D model) was used. The difference in mapped traveltimes of the three experiments are shown in Figure 4.26. The traveltime differences show that MBI ray tracing with interpolation at all boundaries has more errors than interpolation at the salt boundary only. Because the acoustic impedance changes at the salt layer are more significant than any other layers, so this implies that using MBI ray tracing selectively can reduce the computation times while keeping certain levels of accuracy. The computation time of this model in Table 4.6 shows that the MBI ray tracing at the salt boundary is more computationally effective than any other modes. The computation time of the salt dome in the MBI only is $\approx 36.4\%$ less and the full MBI is $\approx 19\%$ less than conventional type ray tracing with initial desne rays. If this experimental algorithm can be expanded and stabilized to perform for real size data, it can be useful to estimating traveltimes and other migration parameters for seismic imaging.

Table 4.6. CPU time for computing salt dome model with the dense rays without interpolation, the MBI ray tracing with interpolating option at all the boundaries, and MBI ray tracing interpolating option at the salt boundary only. The total time for all the three models is small because limited range of angles in y direction (extended direction in 2.5D model) is used for this modeling.

	MBI (salt)	MBI (all)	Dense rays
CPU time	≈ 534 msec	≈ 680 msec	≈ 840 msec

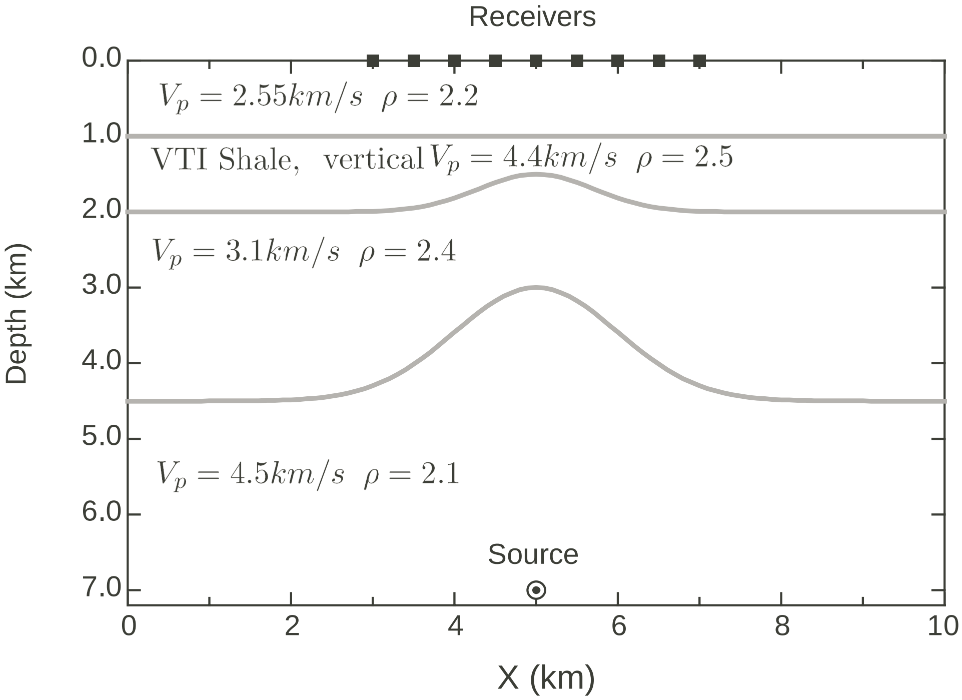

Fig. 4.24. Model geometry of the extended 2D (2.5D) salt dome model. The source is located at the bottom and the line array of the receivers are located on the surface.

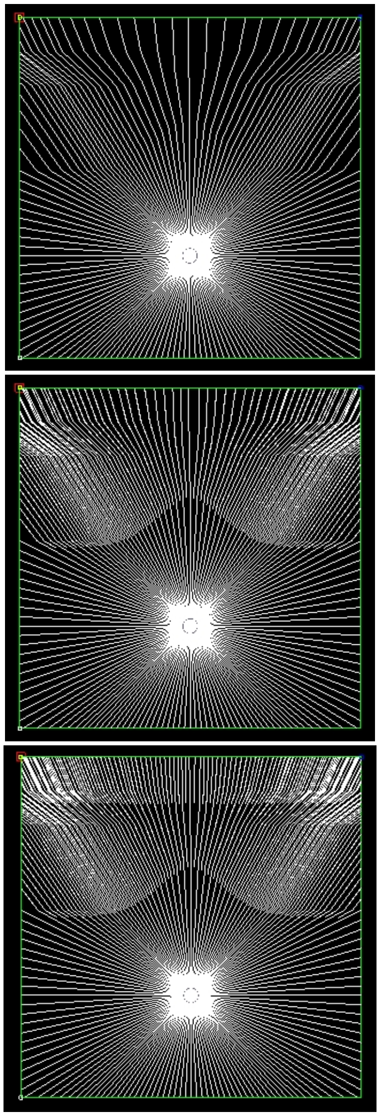

Fig. 4.25. The ray paths of the salt dome model. The top is the conventional ray tracing with the same initial rays of the MBI to illustrate the effects of the MBI. The middle is the MBI ray tracing interpolating the salt boundary only. The bottom is the MBI ray tracing interpolating all the layer boundaries.

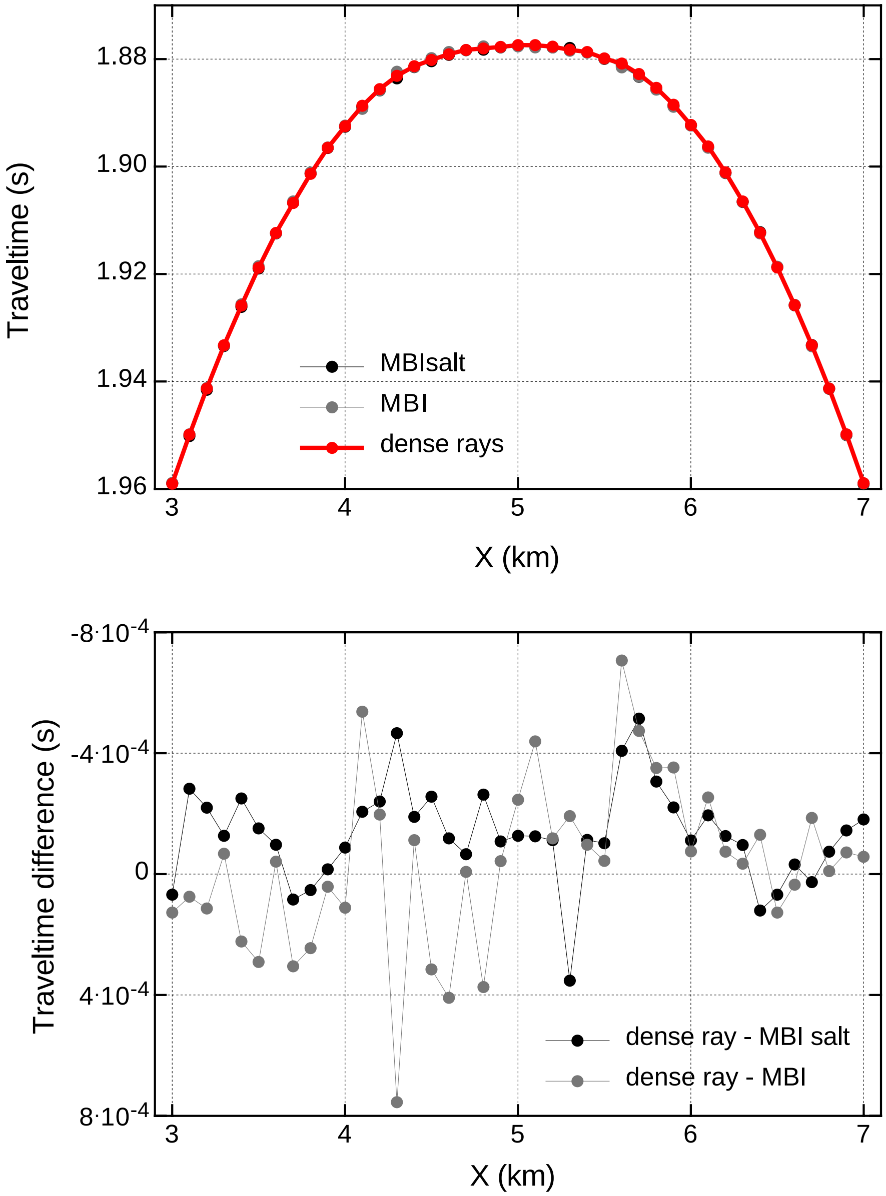

Fig. 4.26. Estimated traveltimes for the three experiments. The difference between the dense ray tracing and the two other MBI ray tracing results are compared.

4.4 Conclusion

The wavefront construction method is an effective modeling tool extended from the conventional ray tracing system. However, most wavefront construction methods are restricted for using gradient or smoothed velocity models due to its high frequency approximation and complicated book keeping problems of handling wavefront at the boundries. Old fashioned layer stripping style ray tracing can handle layered models but it does not have smart control of the ray density over wave propagation. Also, layered models are the most widely used velocity models built in most applications. The model based interpolation (MBI) ray tracing system has been proposed and tested to take the merits of wavefront construction code and overcome the discrepancy of controlling ray density over wave propagation in the conventional ray tracing system. The test results of some simple models showed the potentials of this method which can be a useful and effective tool to model layered velocity models without sacrificing accuracy.

CHAPTER V

CONCLUSION

Ray tracing is a widely used modeling tool for studies in seismic wave propagation. To correctly image subsurface structures, it is important to have traveltimes and other information. However, conventional ray tracing is limited in controlling ray density over propagation, possibly resulting in insufficient ray coverage on interesting subsurface structures. The wavefront construction method, on the other hand, tracks the propagation of wavefronts through the model space performing more efficient calculations than the conventional ray tracing (which handles individual rays). The wavefront construction method does not need to specify the number of rays in a given directions because it refines the wavefront adaptively and keeps the optimal number of rays satisfying ray density criterion.

Both the wavefront construction method and conventional ray algorithms suffer from limitations when take-off angles are used as ray parameters. The mesh constructed with take-off angle ray parameters will have a very dense set of rays near the poles (±90°). The resulting wavefront construction ray tracing will have inefficient ray calculations from computing the very dense set of rays concentrated near the poles and it has numerically unstable ray derivatives along the vertical rays. The Cubed Sphere Mesh is proposed as an alternative way of constructing the initial mesh. In Cubed Sphere Mesh ray parameters, an imaginary cube is constructed with the source located at the center of the cube. Each face of the cube is regularly discretized and a ray is traced from the source through the discretized point. Then the information of the discretized points and the traveltime are the new types of ray parameters. With these new types of ray parameters, there are no poles defined as per the nature of the geometry of the mesh. The numerical properties of conventional take-off angle and the cubed sphere mesh ray parameters were analyzed. The Jacobian and amplitude distribution over the wavefront showed both methods have slightly different error distributions compared with the analytic values, except at the poles. The cubed sphere mesh does not have any pole problems, such as an extra ordinarily dense set of rays and numerical instability, which are observed in the take-off angle mesh. Even though the overall error levels using the take-off angle mesh (except for the poles) are slightly better, the cubed sphere mesh coordinates is more robust regardless of the ray directions.

In this dissertation, a wavefront construction code has been developed for quasi-compressional wave and this method was applied to a low velocity inclusion model which shows strong triplication and a gradient velocity model simulating vertical seismic profiles (VSP) in the Gulf of Mexico. In a low velocity inclusion model where rays are cross bending, which makes triplications in traveltime, and multiple arrivals are still correctly mapped out by the wavefront construction method. Synthetic seismograms were also generated for the VSP data set using the first arrival traveltime, amplitudes, and displacement vectors (Green's tensor parameters).

Many wavefront construction methods require gradient or smoothed velocity models as inputs. A popular way of generating them is by making layered velocity models. In layered velocity models, the model is described with several isotropic or anisotropic layers, usually homogeneous in each layer. Due to the high-frequency approximation of ray tracing embedded in the wavefront construction method, and the complicated bookkeeping problems of the wavefront mesh elements at the hard edge boundaries of the layers, many of the wavefront construction methods do not usually take the layered models. On the other hand, many conventional ray tracing methods can handle layered models, such as the layer stripping method, but they do not have any smart control of ray density over wave propagation. Model based interpolation (MBI) ray tracing is designed to take advantages of both methods by overcoming their drawbacks.

In the MBI ray tracing, the same geometry of WFC is considered by associating neighboring rays required to correctly map solutions on the free surface. Instead of propagating and intepolating the wavefronts with constant increment of traveltime as in the WFC, interpolation is constrained near the layer interfaces in the MBI ray tracing. The wavefronts can be constructed to insert new rays in more localized wavefront mesh elements rather than the global wavefront. For the interpolation threshold, the spatial constraint was selected rather than the traveltime conditions. The modeling results of several isotropic and anisotropic layered models and a salt dome model showed possible potentials of this method as an efficient modeling tool.

REFERENCES

Ben-Menahem, A., and Beydoun, W. B., 1985, Range of validity of seismic ray and beam methods in general inhomogeneous media – I. General theory: Geophys. J. Roy. Astr. Soc., **82**, 207–234.

Ben-Menahem, A., Gibson, R. L. Jr., and Sena, A., 1991, Green's tensor and radiation patterns of point sources in general anisotropic inhomogeneous elastic media: Geophys. J. Int., **107**, 297–308.

Beydoun, W., and Keho, T., 1987, The paraxial ray method: Geophysics, **52**, 1639–1653.

Buske, S., and Kästner, U., 2004, Efficient and accurate computation of seismic traveltimes and amplitudes: Geophys. Prosp., **52**, 313–322.

Červený, V., 1972, Seismic rays and ray intensities in inhomogeneous anisotropic media: Geophys. J. Roy. Astr. Soc., **29**, 1–13.

——— 1985, The application of ray tracing to the propagation of shear waves in complex media:, *in* Doher, G. P., Ed., Seismic shear waves, part A: Theory: Geophysical Press, 1–124.

——— 2001, Seismic ray theory: Cambridge University Press.

Chapman, C., and Shearer, P., 1989, Ray tracing in azimuthally anisotropic media – II. quasi-shear wave coupling: Geophys. J., **96**, 65–85.

Cheng, N., and House, L., 1996, Short note: Minimum traveltime calculation in 3-d graph theory: Geophysics, **61**, 1895–1898.

Coman, R., and Gajewski, D., 2001, Estimation of multivalued arrivals in 3-d models using wavefront ray tracing: 71st Internat. Meeting Abstract, Soc. Expl. Geophys., 1265–1268.

Constance, P., Holland, M., Roche, S., Bicquart, P., Bryans, B., Gelinsky, S., Ralph, J., and Bloor, R., 1999, Simultaneous acquisition of 3-D surface seismic data and 3-C, 3-D VSP data: 69th Ann. Internat. Mtg., Expanded Abstracts, Soc. Expl. Geophys., 104–107.

Durussel, V. B., 2002, Simulation of anisotropic wave propagation in vertical seismic profiles: M.S. thesis, Texas A&M University, College Station.

Ettrich, N., and Gajewski, D., 1996, Wave front construction in smooth media for prestack depth migration: Pure Appl. Geophys., **148**, 481–502.

Fedorov, F. I., 1968, Theory of elastic waves in crystals: Plenum Press.

Gajewski, D., and Pšenčik, I., 1987, Computation of high-frequency seismic wavefields in 3-D laterally inhomogeneous anisotropic media: Geophys. J. Roy. Astr. Soc., **91**, 383–411.

Geoltrain, S., and Brac, J., 1993, Can we image complex structures with first-arrival traveltime?: Geophysics, **58**, 564–575.

Gibson, R. L. Jr., 1999, Ray tracing by wavefront construction in 3-D, anisotropic media: Eos Trans., Amer. Geophys. Union, **80**, F696.

Gibson, R. L. Jr., Sena, A. G., and Toksöz, M. N., 1991, Paraxial ray tracing in 3d inhomogeneous, anisotropic media: Geophys. Prosp., **39**, 473–504.

Gibson, R. L. Jr., Lee, K. J., and Durussel, D., 2002, Efficient meshes for wavefront construction applied to anisotropic media: 72nd Internat. Meeting Abstract, Soc. Expl. Geophys., 1943–1946.

Gibson, R. L. Jr., Durussel, V. D., and Lee, K. J., 2005, Modeling and velocity analysis with a wavefront construction algorithm for anisotropic media: Geophysics, in press.

Gjøstdal, H., Iversen, E., Lecomte, I., Vinje, V., and Åstebøl, K., 2002, Review of ray theory applications in modeling and imaging of seismic data: Stud. geophys. geod., **46**, 113–164.

Hanyga, A., 1982, Dynamic ray tracing in an anisotropic medium: Tectonophysics, **90**, 243–251.

Henneke II, E. G., 1972, Reflection-refraction of stress wave at a plane boundary between anisotropic media: J. Acoust. Soc. Amer., **51**, 210–217.

Kaschwich, T., and Gajewski, D., 2003, Wavefront-oriented ray tracing in 3-D anisotropic media: 65th Conference & Technical Exhibition, European Association of Geoscientists and Engineers (EAGE), P–041.

Kim, S., and Cook, R., 1999, 3-d traveltime computation using second-order eno scheme: Geophysics, **64**, 1867–1876.

Kim, S., 2002, 3-d eikonal solvers: First-arrival traveltimes: Geophysics, **67**, 1225–1231.

Lambaré, G., Lucio, P. S., and Hanyga, A., 1996, Two-dimensional multivalued traveltime and amplitude maps by uniform sampling of a ray field: Geophys. J. Int., **125**, 584–598.

Lee, K. J., and Gibson, R. L. Jr., 2003, Numerical properties of cubed sphere meshes in wavefront construction: 73rd Internat. Meeting Abstract, Soc. Expl. Geophys., 1793–1796.

Leidenfrost, A., EttrichN. Gajewski, D., and Kosloff, D., 1999, Comparison of six different methods for calculating traveltimes: Geophys. Prosp., **47**, 269–297.

Levander, A. R., 1988, Fourth-order finite-difference p-sv seismograms: Geophysics, **53**, 1425–1436.

Lucio, P. S., Lambaré, G., and Hanyga, A., 1996, 3D multidimensional travel time and amplitude maps: Pure Appl. Geophys., **148**, 449–479.

McMechan, G., and Mooney, W., 1980, Asymptotic ray theory and synthetic seismograms for laterally varying structure: Theory and application to the Imperial Valley, California: Bull. Seis. Soc. Amer., **70**, 2021–2035.

Mispel, J., 2001, Transversely isotropic media, 3-d wavefront construction method and prestack depth migration: Ph.D. dissertation, Imperial College of Science, Technology, and Medicine, London, UK.

Mispel, J., and Williamson, P., 2001, 3-D wavefront construction for P & SV waves in transvesely isotropic media: 63rd Conference & Technical Exhibition, European Association of Geoscientists and Engineers (EAGE), P094.

Morton, K. W., and Mayers, D. F., 1994, Numerical solution of partial differential equations: Cambridge Univ. Press.

Moser, T. J., 1991, Shortest path calculation of seismic rays: Geophysics, **56**, 59–67.

Nye, J. F., 1985, Physical properties of crystals: Their representation by tensors and matrices: Oxford University Press.

Podvin, P., and Lecomte, I., 1991, Finite-difference computation of traveltimes in very contrasted velocity models: a massively parallel approach and its associated tools: Geophys. J. Int., **105**, 271–284.

Press, W. H., Flannery, B. P., Teukolsky, S. A., and Vetterling, W. T., 1992, Numerical recipes in c : The art of scientific computing; 2 edition: Cambridge University Press.

Pšenčík, I., and Teles, T. N., 1996, Point source radiation in inhomogeneous anisotropic structures: Pure Appl. Geophys., **148**, 591–623.

Qian, J., and Symes, W., 2002, An adaptive finite-difference method for traveltimes and amplitudes: Geophysics, **67**, 167–176.

Rathore, S. K., Kishore, N. N., and Munshi, P., 2003, An improved method for ray tracing through curved inhomogeneities in composite materials: Journal of Nondestructive Evaluation, **22**, 1–9.

Rokhlin, S. I., Bolland, T. K., and Adler, L., 1986, Reflection and refraction of elastic waves on a plane interface between two generally anisotropic media: J. Acoust. Soc. Amer., **79**, 906–918.

Sava, P., and Fomel, S., 2001, 3-d traveltime computation using huygens wavefront tracing: Geophysics, **66**, 883–889.

Sayers, C. M., 1999, Stress-dependent seismic anisotropy of shales: Geophysics, **64**, 93–98.

Thomsen, L., 1986, Weak elastic anisotropy: Geophysics, **51**, 1954–1966.

Tzimeas, C., 2004, Image resolution analysis: A new, robust approach to seismic survey design: Ph.D. dissertation, Texas A&M University, College Station.

van Avendonk, H. J. A., Harding, A. J., Orcutt, J. A., and Holbrook, W. S., 2001, Hybrid shortest path and ray bending method for traveltime and raypath calculation: Geophysics, **66**, 648–653.

Van Trier, J., and Symes, W., 1991, Upwind finite-difference calculation of traveltimes: Geophysics, **56**, 812–821.

Vidale, J., 1988, Finite-difference calculation of traveltimes: Bull. Seis. Soc. Amer., **78**, 2062–2076.

——— 1990, Finite-difference calculation of traveltimes in three dimensions: Geophysics, **55**, 521–526.

Vinje, V., Iversen, E., and Gjøystdal, H., 1993, Traveltime and amplitude estimation using wavefront construction: Geophysics, **58**, 1157–1166.

Vinje, V., Ketil, Å., Iversen, E., and Gjøystdal, H., 1999, 3-D ray modeling by wavefront construction in open models: Geophysics, **64**, 1912–1919.

Virieux, J., 1986, P-sv wave propagation in heterogeneous media: Velocity-stress finite-difference method: Geophysics, **51**, 889–901.

Zhang, J., and Toksöz, M., 1998, Nonlinear refraction traveltime tomography: Geophysics, **63**, 1726–1737.

APPENDIX A

SEISMIC RAY TRACING IN ANISOTROPIC MEDIA

Seismic ray theory is a high frequency approximation using asymptotic solutions of the elastodynamic equation. Červený (1972) has derived the traveltime and amplitude computation for inhomogeneous general anisotrpic medium using asymptotic seismic ray tracing. In 2001, he published a book introducing ray theory and its details (Červený, 2001). This appendix reviews mainly the derivation of ray theory for inhomogeneous general anisotrpic medium by Červený (1972) and his book (Červený, 2001), and the paraxial ray theory by Gibson et al. (1991).

Elastodynamic Theory

In the Lagrangian description of motion (describing the motion of particles specified by original position and a reference time), the displacement vector, $\underline{u} = \underline{u}(\underline{x}, t)$, is a vector distance of a particle at time t from position $\underline{x}$ at the reference time. We suppose the stress vector and strain vector are symmetric,

$$\tau_{ij} = \tau_{ji}, \quad e_{ij} = e_{ji} \tag{A.1}$$

where $\tau_{ij}(\vec{x}, t)$ is Cartesian components of the stress tensorr and $e_{ij}(\vec{x}, t)$ is the Cartesian components of the strain tensor.

The displcement vector can be used to express the strain tensor:

$$e_{ij} = \frac{1}{2}(u_{i,j} + u_{j,i}) \tag{A.2}$$

where $u_{i,j}$ represents the ith component of partial differentiation of $\vec{u}$ with respect to jth component.

The stress tensor describes the stress condition at a point $\vec{x}$ and it can be used to express traction, $\vec{T}$ acting across a surface element of arbitrary direction at $\vec{x}$,

$$T_i = \tau_{ij} n_j, \tag{A.3}$$

where $\underline{n}$ is the normal unit vector of the surface.

The elastodynamic euqation sets the relation between the spatial variations of stress and the temporal variations of the displacement vector,

$$\tau_{ij,j} + f_i = \rho \ddot{u}_i, \quad i = 1, 2, 3. \tag{A.4}$$

where, f_i are the Cartesian components of body force (force/volume) or source term, and ρ is the density. $\ddot{u}_i$ is the second partial derivative of u_i with respect to time, $\partial^2 u_i / \partial t^2$.

Stress-Strain Relations

The generalized Hooke's law relates stress with strain linearly in a linear, anisotropic, elastic solid. This is called the constituiteve stress-strain relation,

$$\tau_{ij} = c_{ijkl} e_{kl}, \tag{A.5}$$

where c_{ijkl} are components of the 4th order elastic tensor. The general form of the elastic tensor has 81 components ($3^4 = 81$) but it can be reduced to 21 components by the symmetry relations of the elastic tensor,

$$c_{ijkl} = c_{jikl} = c_{ijlk} = c_{klij}. \tag{A.6}$$

This constituitive equation can be used to express strain tensor in terms of stress tensor,

$$e_{ij} = s_{ijkl} \tau_{kl}, \tag{A.7}$$

where s_{ijkl} is called the *compliances* which is $s = c^{-1}$. Thus it has the relation of

$$s_{ijkl} c_{klmn} = c_{ijkl} s_{klmn} = \delta_{im} \delta_{jn}. \tag{A.8}$$

where δ_{ij} is called the Kronecker delta, defined by

$$\delta_{ij} = \begin{cases} 1 & \text{when } i = j, \\ 0 & \text{when } i \neq j. \end{cases} \tag{A.9}$$

The components, c_{ijkl}, of the elastic tensor are also called elastic constants, elastic moduli, elastic parameters, or *stiffness*. The unit of c_{ijkl} is same as the unit of stress (kg/ms^2) and the compliance tensor has the unit of stress^{-1} as described in the relation of equation (A.8). The relationship between stress and strain tensors can be expressed with displacement vectors. From the equation (A.2) and using symmetry, we can replace e_{kl} with $u_{k,l}$,

$$\tau_{ij} = c_{ijkl}u_{k,l}. \tag{A.10}$$

The components c_{ijkl} can be expressed using Voigt notation, C_{mn}: $m \rightarrow i, j$ and $n \rightarrow k, l$. Using symmetry, $C_{mn} = C_{nm}$ and it reduces 81 components of c_{ijkl} to 21 independent elastic moduli, C_{mn}:

$$C_{mn} = \begin{pmatrix} C_{11} & C_{12} & C_{13} & C_{14} & C_{15} & C_{16} \\ & C_{22} & C_{23} & C_{24} & C_{25} & C_{26} \\ & & C_{33} & C_{34} & C_{35} & C_{36} \\ & & & C_{44} & C_{45} & C_{46} \\ & & & & C_{55} & C_{56} \\ & & & & & C_{66} \end{pmatrix} \tag{A.11}$$

Anisotropic symmetric axes are well discussed by various authors (Fedorov, 1968; Nye, 1985). The symmetry is often discribed with *n-fold rotation axis of symmetry* which means a rotation of $2\pi/n$ about a given axis, where n is positive (Nye, 1985). General anisotropic symmetry is *triclinic symmetry* which has no symmetry other than a 1-fold axis and it may have 21 independent moduli. In seismic studies, *othorhombic* and *hexagonal* symmetry are more common. The *orthorhombic symmetry* has three mutually perpendicullar 2-fold axes of symmetry and the number of elastic moduli reduces to 9 from 21 of *triclinic symmtery.* Then, C_{mn} in the Cartesian coordinate system:

$$C_{mn} = \begin{pmatrix} C_{11} & C_{12} & C_{13} & 0 & 0 & 0 \\ & C_{22} & C_{23} & 0 & 0 & 0 \\ & & C_{33} & 0 & 0 & 0 \\ & & & C_{44} & 0 & 0 \\ & & & & C_{55} & 0 \\ & & & & & C_{66} \end{pmatrix} \tag{A.12}$$

In *hexagonal symmetry* system, only a single 6-fold axis of rotation exists. In this symmetry system, the number of moduli is five when the vertical axis in Cartesian coordinates is selected as the 6-fold axis of rotation:

$$C_{mn} = \begin{pmatrix} C_{11} & C_{11}-2C_{44} & C_{11}-2C_{44} & 0 & 0 & 0 \\ & C_{11} & C_{11}-2C_{44} & 0 & 0 & 0 \\ & & C_{11} & 0 & 0 & 0 \\ & & & C_{44} & 0 & 0 \\ & & & & C_{44} & 0 \\ & & & & & C_{44} \end{pmatrix} \qquad \text{(A.13)}$$

The medium of the hexagonal symmetry system is transversely isotropic due to its general invariance in rotation by any angle about the axis of symmetry. The axis of symmetry can be tilted in an arbitrary direction (*Tilted Transversely Isotropic*: TTI) or horizontal (*Horizontal Transeversely Isotropic*: HTI). If the axis is vertical (*Vertical Transeversely Isotropic*: VTI), it is azimuthal anisotropy. The most common type of anisotropy in seismology is hexagonal symmetry and the anisotropy in common type of rocks and sedments in exploration seismology is usually weak (Thomsen, 1986).

Elastodynamic Equation of Motion

From the equation of elastodynamic relations between stress and displacement vectors (A.4) and the relationship of stress and displacement vectors (A.10), we have the *elastodynamic equation* for general anisotropic, perfectly elastic, and inhomogeneous medium.

$$\left(c_{ijkl}u_{k,l}\right)_{,j} + f_i = \rho \ddot{u}_i, \quad i = 1, 2, 3. \qquad \text{(A.14)}$$

From the generalized Hooke's law of (A.1) and the strain-displacement relationship (A.2), we obtain Hooke's law in an isotropic medium:

$$\tau_{ij} = \lambda \delta_{ij} u_{k,k} + \mu(u_{i,j} + u_{j,i}). \qquad \text{(A.15)}$$

By inserting (A.15) into the elastodynalic relation of (A.4) we obtain the elastodynamic equation for the unbounded isotropic, inhomogeneous medium,

$$(\lambda u_{j,j})_{,i} + \{\mu(u_{i,j} + u_{j,i})\}_{,j} + f_i = \rho \ddot{u}_i, \quad i = 1, 2, 3. \qquad \text{(A.16)}$$

Ray Theory for inhomogeneous anisotropic medium

The devlopment of ray theory for inhomogeneous and anisotropic elastic medium can be started with the equation of motion. In 3D rectangular Cartesian coordinates, the equation of motion without body force from (A.14) is

$$\frac{\partial}{\partial x_i}\left(c_{ijkl}\frac{\partial U_k}{\partial x_l}\right) = \rho\frac{\partial^2 U}{\partial t^2}, \tag{A.17}$$

where t is time, x_i are the components of rectangular Cartesian coordinates, ρ is density, U_j are the components of the displacement vector $\mathbf{U}$, and c_{ijkl} are elastic coefficients of material.

The analytic solutions of (A.17) are not easy to derive (or not known) along moving wavefronts (Červený, 1972). Suppose a wavefront is a function of traveltime, $t = \tau(x_i)$, and if we are looking for an approximate solution in a ray series,

$$U_k(x_i,t) = \sum_{n=0}^{\inf} U_k^{(n)}(x_i) f_n(t-\tau(x_i)), \tag{A.18}$$

where the function f has the following property of

$$\frac{df_{n+1}(\xi)}{d\xi} = f_n(\xi).$$

If (A.18) is plugged in the equation of motion (A.17), then it becomes,

$$\mathbf{N}(\mathbf{U}^{(n)}) - \mathbf{M}(\mathbf{U}^{(n-1)}) + \mathbf{L}(\mathbf{U}^{(n-2)}) = 0 \tag{A.19}$$

where n=0,1,2 ..., with $\mathbf{U}^{(-1)} = \mathbf{U}^{(-2)} = 0$. $\mathbf{N}, \mathbf{M}$ and $\mathbf{L}$ are

$$N_j(\mathbf{U}^{(n)}) = \Gamma_{jk}U_k^n - U_j^n, \tag{A.20a}$$

$$M_j(\mathbf{U}^{(n)}) = p_i a_{ijkl}\frac{\partial U_k^n}{\partial x_l} + \frac{1}{\rho}\frac{\partial}{\partial x_i}(\rho a_{ijkl} p_i U_k^{(n)}), \tag{A.20b}$$

$$L_j(\mathbf{U}^{(n)}) = \frac{1}{\rho}\frac{\partial}{\partial x_i}(\rho a_{ijkl}\frac{\partial U_k^{(n)}}{\partial x_l}), \tag{A.20c}$$

where

$$\Gamma_{jk} = p_i p_l a_{ijkl}, \quad a_{ijkl} = \frac{c_{ijkl}}{\rho}, \quad p_i = \frac{\partial \tau}{\partial x_l} \tag{A.21}$$

This is the basic system of equations of ray theory for anisotropic inhomogeneous media (Červený, 1972). The eigenvalues of Γ_{jk} can be found by solving the characteristic equation

$$Det(\Gamma_{jk} - G\delta_{jk}) = 0, \tag{A.22a}$$

$$G^3 - PG^2 + QG - R = 0, \tag{A.22b}$$

where P, Q, and R are the invariants of the symmetric matrix Γ_{jk}. Γ_{jk} 3 eigen values and eigen vectors from A.22. Since Γ_{jk} is positive definite, its eigenvalues, G_1, G_2, and G_3 are also real and positive. When we use Euler's theorem for homogeneous functions, we will get the equation

$$p_i \frac{\partial G_m}{\partial p_i} = 2G_m \qquad (m = 1, 2, 3). \tag{A.23}$$

The corresponding eigenvectors, $\vec{g}^1$, $\vec{g}^2$, and $\vec{g}^3$ are unit vectors and can be determined from the following equation for $G_1 \neq G_2 \neq G_3$

$$(\Gamma_{jk} - G_m\delta_{jk})g_k^{(m)} = 0. \tag{A.24}$$

When $n = 0$, equation (A.19) simplified as $\mathbf{N}(\mathbf{U}_k^{(0)}) = 0$, or

$$(\Gamma_{jk} - \delta_{jk})U_k^{(0)} = 0, \tag{A.25}$$

It is easy to see that equation (A.25) has non-trivial solutions when one of G_i is equal to one by comparing to equation (A.22a). That is, for $G_1 \neq G_2 \neq G_3$, equation (A.25) has a non-trivial solution when

$$G_m(p_i, x_i) = 1, \tag{A.26}$$

Equation (A.26) is a non-linear partial differential equation for $\tau(x_i)$ stating the propagation of three different wavefronts (Červený, 1972): one quasi-P wave and two quasi-S waves. When two eigenvalues are identical (say, $G_2 = G_3$), then two wavefronts are identical as in the isotropic medium. Solving equation (A.26) with the characteristics method and using equation (A.23), equation (A.26) can be written as

$$\frac{dx_i}{d\tau} = \frac{1}{2}\frac{\partial G_m}{\partial p_i}, \tag{A.27a}$$

$$\frac{dp_i}{d\tau} = -\frac{1}{2}\frac{\partial G_m}{\partial x_i} \tag{A.27b}$$

where $i = 1, 2, 3$. This set of equation is a critical part of the ray tracing system. From equation (A.22) after some work, we obtain

$$\begin{aligned}\frac{\partial G_m}{\partial p_i} &= \frac{\partial \Gamma_{jk}}{\partial p_i}\frac{D_{jk}}{D},\\ \frac{\partial G_m}{\partial x_i} &= \frac{\partial \Gamma_{jk}}{\partial x_i}\frac{D_{jk}}{D},\end{aligned} \tag{A.28}$$

where

$$\begin{aligned}
D_{11} &= (\Gamma_{22} - 1)(\Gamma_{33} - 1) - \Gamma_{23}^2,\\
D_{22} &= (\Gamma_{11} - 1)(\Gamma_{33} - 1) - \Gamma_{13}^2,\\
D_{33} &= (\Gamma_{11} - 1)(\Gamma_{22} - 1) - \Gamma_{12}^2,\\
D_{12} &= D_{21} = \Gamma_{13}\Gamma_{23} - \Gamma_{12}(\Gamma_{33} - 1),\\
D_{13} &= D_{31} = \Gamma_{12}\Gamma_{23} - \Gamma_{13}(\Gamma_{22} - 1),\\
D_{23} &= D_{32} = \Gamma_{12}\Gamma_{13} - \Gamma_{23}(\Gamma_{11} - 1),\\
D &= trD_{jk} = D_{11} + D_{22} + D_{33}.
\end{aligned} \tag{A.29}$$

From equation (A.21), the derivatives of $\Gamma_j k$ with respect to x_i and p_i can be obtained as

$$\begin{aligned}\frac{\partial \Gamma_{jk}}{\partial x_i} &= a_{ijkl} p_l D_{jk}/D,\\ \frac{\partial \Gamma_{jk}}{\partial p_i} &= (a_{ijkl} + a_{ikjl})p_l.\end{aligned} \tag{A.30}$$

Gathering and simplifying terms in equations (A.27), (A.28), and (A.30), we obtain the final set of equations describing the ray tracing for inhomogeneous anisotropic medium.

$$\begin{aligned}\frac{dx_i}{d\tau} &= a_{ijkl} p_l D_{jk}/D\\ \frac{dp_i}{d\tau} &= -\frac{1}{2}\frac{\partial a_{ijks}}{\partial x_i} p_l p_s D_{jk}/D,\end{aligned} \tag{A.31}$$

where $i = 1, 2, 3$.

For isotropic medium, the equations describing the ray tracing is simpler than (A.31).

$$\begin{aligned} \frac{dx_i}{d\tau} &= v^2 p_i \\ \frac{dp_i}{d\tau} &= -\frac{1}{v}\frac{\partial v}{\partial x_i}, \quad i = 1, 2, 3. \end{aligned} \tag{A.32}$$

where v is the velocity of compressional wave (α) or shear wave (β) (Gibson et al., 1991).

By solving the system of ray equations, we obtain the following physical quantities as well as the physical Cartesian coordinates x_i along the ray (Červený, 2001).

- The components of a point along the ray path: x_i.
- The components of slowness vector ($\vec{p}$), p_i, perpendicular to the wavefront at each point along the ray.
- The phase velocity: $\mathcal{C} = (\mathcal{C}_k\mathcal{C}_k)^{1/2} = (p_k p_k)^{-1/2}$, and phase velocity components: $\mathcal{C}_i = p_i/p_k p_k$.
- The components of unit normal to the wavefront: $N_i = \mathcal{C}p_i$.
- The components of polarization vector, $g_i^{(m)}$, for the corresponding wave types. The polarization vector defines the direction of the displacement vector for the wave type.
- The components and magnitude of group velocity vector:

$$\mathcal{U}_i = \frac{dx_i}{d\tau} = a_{ijkl}p_l g_j^{(m)} g_k^{(m)} = a_{ijkl}p_l D_{jk}/D, \quad \mathcal{U} = (\mathcal{U}_k\mathcal{U}_k)^{1/2}$$

- The components of the unit vector tangent to the ray: $t_i = dx_i/ds = \mathcal{U}/(\mathcal{U}_k\mathcal{U}_k)^{1/2}$, where s is the arclength along the ray path.
- Angle γ between the ray and normal to the wavefront:

$$cos\gamma = \vec{t}\cdot\vec{N} = (\mathcal{C}/\mathcal{U})(\vec{p}\cdot\vec{\mathcal{U}}) = \mathcal{C}/\mathcal{U}.$$

- Angle ξ between the ray and the polarization vector $\vec{g}^{(m)}$:

$$cos\xi = \vec{t} \cdot \vec{g}^{(m)}.$$

- Angle η between the polarization vector and the normal to the wavefront:

$$cos\eta = \vec{N} \cdot \vec{g}^{(m)}.$$

Traveltime Computation from Ray Tracing

The application of the high-frequency assymptotic methods to the acoustic wave equation leads to the eikonal equation $(\nabla\tau)^2 = 1/v^2$, and to the elastodynamic equation yields $(\nabla\tau)^2 = 1/\alpha^2$ for P waves and $(\nabla\tau)^2 = 1/\beta^2$ for two identical S waves in isotropic inhomogeneous medium. For anisotropic inhomogeneous medium, there are three types of waves: quasi-P waves, and two quasi-S waves. The corresponding eikonal equation is $G_m(x_i, p_i) = 1, \quad i = 1, 2, 3,$ where G_m are the eigenvalues in Christoffel matrix [see (A.26) and Červený (2001)].

The eikonal equation is a first order nonlinear partial differential equation that can be solved by the method of characteristics. In seismic ray theory, rays are defined as the characteristics of the eikonal equations and the system of ODEs are called the ray tracing system or system of ray equations (A.31) and (A.32) (Červený, 2001).

Computing traveltime in acoustic or isotropic medium can be obtained by directly solving the eikonal equations in the finite-difference way (finite-difference solver of eikonal equation) (Vidale, 1988; Vidale, 1990; Podvin and Lecomte, 1991; Kim, 2002; Qian and Symes, 2002). Even if it is called finite-difference solver, it is not directly applying conventional finite-difference method to solve the eikonal equation but it is conceptually solving the eikonal equation in finite-difference way as a consequence. This method is computing the first-arrival traveltime only. Another popular way of computing first-arrival traveltime is network shortest-path ray tracing which is based on the theory of graphs (Moser, 1991; Cheng and House, 1996; van Avendonk et al., 2001). The first-arrival traveltime is a function of position which is unique in space and, thus, it exists even in shdow zones and doest not have multivalued (single-valued anywhere) beyond caustics. Also it does not have direct relation with ray concepts and wave types.

Ray-theory traveltime is computed from ray tracing for each wave type. It can a be multivalued function of the coordinates of the receiver beyond caustics due to multipathing. By solving the system of ray equations, we obtain the ray-theory traveltime as well as the ray paths. (A.31) can be used for anisotropic inhomogeneous medium as well as isotropic inhomogeneous medium and (A.32) can be used to compute the traveltime and the ray path for isotropic inhomogeneous medum. In general, ray tracing can be solved in four different ways. They can be solved numerically, analytically, semi-analytically, or by cell ray tracing methods (Červený, 2001). The most practically used method in seismology uses numerical methods to solve the set of the first order ordinary differential equations (ODEs) with initial conditions: the initial position (x_0) and the direction (p_0) of the ray at the source point. Popular numerical solvers are high-order adaptive Runge-Kutta methods and predictor-corrector types of numerical ODE solvers. In this thesis, a 5th order adaptive Runge-Kutta method has been used as a numerical solver.

APPENDIX B

AMPLITUDE COMPUTATION FROM RAY TRACING

Solving the system of ray equations (A.31) and (A.32), and computing traveltime is called kinematic ray tracing due to its description of kinematic aspects. The ray amplitudes along the ray are controlled by the transport equation and it can be solved in terms of ray parameters or Jacobian. The Jacobian can be computed by Dynamic ray tracing or directly from kinematic ray tracing. The representaion of transport equation in terms of Jacobian using kinematic ray tracing from an acoustic case to anisotropic elastic case is shown. This review of the derivation is following Červený's (2001) and Gajewski's (1987) work.

In an acoustic case, the wave equation is

$$\nabla^2 p = \frac{1}{c^2(x_i)}\ddot{p}, \tag{B.1}$$

where $c(x_i)$ is the acoustic velocity as a function of position, and p is the pressure as a function of position and time. If we try a high-frequency time harmonic solution,

$$p(x_i,t) = A(x_i)e^{-iw(t-\tau(x_i))}, \tag{B.2}$$

$A(x_i)$ is the magnitude of the trial solution. Assuming a high frequency approximation, $w \gg 0$, $A(x_i)$ and $\tau(x_i)$ are smooth. Using vectorial identity: $\nabla \cdot a\vec{b} = \vec{b} \cdot \nabla a + a\nabla \cdot \vec{b}$,

$$\begin{aligned}\nabla^2 p &= \nabla \cdot \nabla p \\ &= \{iw(\nabla A + iwA\nabla\tau) \\ &+ (\nabla^2 A + iw\nabla\tau \cdot \nabla A + iwA\nabla^2\tau)\}e^{-iw(t-\tau(x_i))}.\end{aligned} \tag{B.3}$$

Substituting $\nabla^2 p$ in (B.1) with (B.3), we obtain the following expression,

$$-w^2 A\left[(\nabla\tau)^2 - \frac{1}{c(x_i)^2}\right] + iw\left[2\nabla A \cdot \nabla\tau + A\nabla^2\tau\right] + \nabla^2 A = 0. \tag{B.4}$$

We want this equation to be valid for any frequency, but we have only two variables independent of w for three terms. However, we want w^1 and w^2 terms be vanished in high frequency approximation (we are more interested in higher frequencies). Then we have the following equations in acoustic case,

- Eikonal equation (from w^2 terms):

$$(\nabla\tau)^2 = \frac{1}{c(x_i)^2}, \tag{B.5}$$

- Transport equation (from w terms):

$$2\nabla A \cdot \nabla\tau + A\nabla^2\tau = 0. \tag{B.6}$$

If we introduce a variable density term, ρ, the transportation equation with $A/\sqrt{\rho}$ instead of A becomes

$$2\nabla\tau \cdot \nabla(A/\rho) + (A/\rho)\nabla^2\tau = 0. \tag{B.7}$$

Along the ray, $\nabla\tau = \vec{t}/c(x_i)$, where $c(x_i)$ is the velocity and $\vec{t}$ is the tangent unit vector to the ray direction. Recall that $\vec{t} \cdot \nabla(A/\rho) = d(A/\sqrt{\rho})/ds$,

$$\frac{d}{ds}\left(\frac{A}{\sqrt{\rho}}\right) + \frac{c}{2}\frac{A}{\sqrt{\rho}}\nabla^2 A = 0. \tag{B.8}$$

Relation of Jacobian (J) to $\nabla^2\tau$

The transport equation in isotropic media (including the acoustic case) is expressed in terms of $\nabla^2\tau$.

$$\nabla^2\tau = \nabla \cdot \nabla\tau = \nabla \cdot \vec{p}, \tag{B.9}$$

where $\vec{p}$ is the slowness vector. In an isotropic medium, $V = \mathcal{U}$, where $\mathcal{U}$ is the gourp velocity and $V = c, \alpha$, or β, and we can put $\vec{p} = \vec{\mathcal{U}}/V^2$,

$$\begin{aligned} \nabla^2\tau &= -\frac{2}{V^3}\nabla V \cdot \vec{\mathcal{U}} + \frac{1}{V^2}\nabla \cdot \vec{\mathcal{U}} \\ &= \frac{1}{J_\tau}\frac{d}{d\tau}\left(\frac{J_\tau}{V}\right) = \frac{1}{VJ_s}\frac{d}{d\tau}\left(\frac{J_s}{V}\right) = \frac{1}{J_s}\frac{d}{ds}\left(\frac{J_s}{V}\right), \end{aligned} \tag{B.10}$$

The Jacobian (J) is a transformation from ray coordinate $(\gamma_1, \gamma_2, \gamma_3)$ to Cartesian coordinate (x, y, z):

$$J_\tau = \begin{vmatrix} \frac{\partial x}{\partial \gamma_1} & \frac{\partial x}{\partial \gamma_2} & \frac{\partial x}{\partial \tau} \\ \frac{\partial y}{\partial \gamma_1} & \frac{\partial y}{\partial \gamma_2} & \frac{\partial y}{\partial \tau} \\ \frac{\partial z}{\partial \gamma_1} & \frac{\partial z}{\partial \gamma_2} & \frac{\partial z}{\partial \tau} \end{vmatrix}, \quad \text{and} \quad J_s = \begin{vmatrix} \frac{\partial x}{\partial \gamma_1} & \frac{\partial x}{\partial \gamma_2} & \frac{\partial x}{\partial s} \\ \frac{\partial y}{\partial \gamma_1} & \frac{\partial y}{\partial \gamma_2} & \frac{\partial y}{\partial s} \\ \frac{\partial z}{\partial \gamma_1} & \frac{\partial z}{\partial \gamma_2} & \frac{\partial z}{\partial s} \end{vmatrix}. \tag{B.11}$$

In take-off angle ray coordinates system, the ray parameters are defined as $\gamma_1 = \psi$ (declination), $\gamma_2 = \theta$ (azimuth), and $\gamma_3 = s$ (arclength along the ray) or $\gamma_3 = \tau$ (traveltime along the ray). Different types of ray parameters are avaiable if the ray is uniquely defined in space and time with the definign ray parameters. See Červený (2001) for more details on the derivation of $\nabla \cdot \vec{\mathcal{U}} = \frac{1}{VJ_\tau}\frac{d}{d\tau}\left(\frac{J_\tau}{V}\right)$.

Representation of Amplitude with Jacobian

Inserting (B.10) into (B.8), it is simplified as,

$$\frac{d}{ds} ln \left\{ A(s)\sqrt{\frac{J(s)}{\rho(s)c(s)}} \right\} = 0, \tag{B.12}$$

which has the solution of

$$A(s) = \Psi(\gamma_1, \gamma_2)\left(\frac{\rho(s)c(s)}{J(s)}\right)^{1/2} = \left[\frac{\rho(s)c(s)J(s_0)}{\rho(s_0)c(s_0)J(s)}\right]^{1/2} A(s_0), \tag{B.13}$$

where Ψ is constant along the ray and varies in other rays. It is basically describing the initial amplitude distributiotn at s_0. This is the amplitude along the ray for the acoustic case.

For isotropic elastic medium, in a similar way,

$$A(s) = \frac{\Psi(\gamma_1, \gamma_2)}{\sqrt{(\rho(s)v(s)J(s))}} = \left[\frac{\rho(s_0)v(s_0)J(s_0)}{\rho(s)v(s)J(s)}\right]^{1/2} A(s_0), \tag{B.14}$$

where $v = \alpha$ or β for isotropic elastic case.

For anisotropic inhomogeneous medium, the transportation equation along the ray is

$$2\vec{\mathcal{U}} \cdot \nabla(\sqrt{\rho}A) + (\sqrt{\rho}A)\nabla \cdot \vec{\mathcal{U}} = 0, \tag{B.15}$$

and similarto the isotropic case, applying the relation of $\nabla \cdot \vec{\mathcal{U}}$,

$$\frac{d}{ds}(\sqrt{\rho}A) + \frac{1}{2\mathcal{U}}\sqrt{\rho}A\nabla \cdot \vec{\mathcal{U}} = 0. \tag{B.16}$$

will lead us to have

$$A(s) = \frac{\Psi(\gamma_1, \gamma_2)}{\sqrt{\rho(s)(U_s)J(s)}} = \left[\frac{\rho(s_0)\mathcal{U}(s_0)J(s_0)}{\rho(s)\mathcal{U}(s)J(s)}\right]^{1/2} A(s_0). \tag{B.17}$$

or when the third ray parameter is traveltime ($\gamma_3 = \tau$),

$$A(\tau) = \left[\frac{\rho(\tau_0)\mathcal{U}(\tau_0)J(\tau_0)}{\rho(\tau)\mathcal{U}(\tau)J(\tau)}\right]^{1/2} A(\tau_0). \tag{B.18}$$

VITA

Kyoung Jin Lee was born in Seoul, Korea. He finished his B.S. in geology at Korea University, 1991. During his study in undergraduate, he was awarded in the National University Student Research Paper Contest in 1990. After his undergraduate study, he started his M.S. program with Dr. A. F. Gangi at Texas A&M University in 1991 and received his M.S. degree in geophysics in 1994. In 1994 he joined LG Precision, now Nex1, as a DSP system developer for various SONAR systems. After his industry experience in underwater acoustics, he returned to the more exciting geophysical world by studying seismic wave propagation and imaging for his Ph.D. under Dr. R. L. Gibson at Texas A&M University and received his Ph.D. in 2005. He is now working in BP EPTG as a geophysicist. His permanent address is 13519 Westport, Houston, TX 77079, USA and email address is seisprofs@yahoo.com.